Università
Ca'Foscari
Venezia

Master's Degree
in
Sciences and technologies of Bio and Nanomaterials

Final Thesis

Analysis of the effects of low-temperature degradation on mechanical properties of BIOLOX® delta femoral heads through fractographic study and Raman spectroscopic analysis

Supervisor
Ch. Prof. Pietro Riello
Ch. Prof. Giuseppe Pezzotti

Graduand
Marco Ciniglio
Matriculation number
838720

Academic Year
2018/2019

The greatest enemy of knowledge is not ignorance,
it’s the illusion of knowledge.
D. J. Boorstin

ABSTRACT

Zirconia-toughened-alumina (ZTA) is one of the most used bioceramic material for artificial hip joints. Some of the reasons for its success are the mechanical properties of this material, in particular, the high flexural strength and fracture toughness.

During the propagation of a microcrack, the polymorphic transformation from tetragonal zirconia to monoclinic zirconia occurs, triggering a volumetric expansion of the 3-4% zirconia grain size. The increase in volume allows the material to block the development of the crack and helps to preserve the integrity of the overall structure by recording the highest value of compressive stress at the tip of the crack. Over the years, numerous studies concerning the transformation of the ceramic material subjected to stress have been carried out, observing how, on the surface, the zirconia polymorphic transformation occurs spontaneously in a hydrothermal environment.

In this work, the results of the fractographic study conducted on artificial femoral heads subjected to preliminary burst resistance tests are analyzed. Through the test, it is possible to study how the mechanical properties of the ZTA femoral heads have changed or how much the LTD could have influenced, for example, the flexural strength or fracture toughness.

The ZTA BIOLOX® delta femoral heads (CeramTec, Plochingen, Germany) were all 28mm in diameter, made of a patented Alumina (Al_2O_3) matrix (80%) containing 17% Zirconia (ZrO_2), partially stabilized with approximately 1.3mol% yttrium oxide (Y_2O_3).

The burst strength test was performed according to ISO 7206-10 standards. The variation in fracture resistance evaluated before and after accelerated degradation at low temperatures, recording an average burst strength of 52 kN for pristine femoral heads, while for the aged ones had an average breaking value was ~13% lower.

Furthermore, the aged samples showed an increase of the monoclinic zirconia volume fraction, ranging from about 6% (before hydrothermal degradation) to more than 50% (after hydrothermal degradation).

All the analyzed ZTA femoral heads have exceeded the minimum fracture resistance value, according to the regulations stipulated by the US FDA despite the critical conditions applied. The samples, through a fractographic approach combining Raman spectroscopy analysis and optical analyses such as laser microscopy and SEM microscopy, were studied.

CONTENTS

1. INTRODUCTION

The hip, the second-largest joint of the human body, is the primary tool for locomotion, is exposed to a higher number of traumatic risks, which all lead to the pathological condition called: osteoarthritis. Regarding the initial causes, the diagnosis is almost always the same: intense joint pain, limited movements, and impaired locomotor function.

Total hip arthroplasty (THA), surgical replacement of the hip joint, is a procedure that has dramatically improved the resolution of those pathologies of the hip joint, giving new lymph to conventional medical therapy. The primary purpose following the creation of a "new hip" is to allow the patient to carry out daily activities autonomously, consequently no intolerance and rejection phenomena in the short and long term should occur.

The leading causes that lead the patient to need surgery are various; we talk about primary arthritis or the early decrease of the joint tissue, local necrosis leading to cell death caused by an alteration of the circulatory system of the femoral heads, femoral neck fracture, arthritis, and post-traumatic necrosis. [1]

The main cause of the pain is represented by the wear of the cartilage, whose purpose is to slide the articular surfaces. In addition to diseases such as osteoarthritis, the main causes that lead to total hip replacement may be “post-traumatic arthrosis” and “avascular necrosis.”

Post-traumatic arthritis is a severe hip injury characterized by a fracture or dislocation where fractures of the hip bones that have suffered trauma over time can lead to the damage of the articular cartilage, resulting in intense pain.

Avascular necrosis is also in this case, a possible hip injury, in the form of dislocation or a fracture, can limit the flow of blood to the head of the femur which ends up losing vitality in some of its parts or entirely. The lack of blood can cause the dead bone surface to collapse, which will result in osteoarthritis.

In most patients undergoing the operation, a marked improvement in motor functions is observed, but the main goal is pain reduction. As for the average life of an artificial joint prosthesis, it is about 8-12 years, although the duration is less for younger and more active people.

Arthroplasty has undergone a continuous transformation over the years, both in the materials and in the practical technique used.

Starting with the first total hip arthroplasty made by Charnely, this technique has become one of the most general operations of modern orthopedic surgery.

The ceramic materials are used for the first time in the orthopedic sector in the seventies as material for the femoral heads in substitution of the metal components available for the THA. [2]

Subsequently, also the ceramic acetabular coatings have been manufactured and used in coupling with the ceramic femoral heads, thus constituting the first COC systems. [3]

The extensive use of these new biomaterials born from their high biocompatibility and the ability to reduce frictional wear. The most used structural ceramic materials nowadays are Zirconia stabilized with Yttrium (Y-TZP) and zirconia-toughened alumina (ZTA).

Among the mechanical properties of the femoral heads, these have a low degree of porosity, to avoid the corrosion of the material by the body fluids, and to reduce frictional wear with the bearing. Usually, femoral heads are produced with a roughness of fewer than 10 nanometers; moreover, the ceramic femoral heads have more hardness than the metalheads. [4][5] In cases where fractures of ceramic femoral heads occur, surgical revision surgery is necessary for the replacement and removal of the fractured component; usually, the rate of fractures for ceramic femoral heads is around 1: 10,000. [6] To limit the number of fractures, manufacturers use standardized proof test and burst strength tests to maximize the quality of the marketed product. Usually, the ceramic heads are subjected to continuous cycles of loading, higher than the average physiological load, to certify the maximum load to which the material can be subjected during its use.

Following the breaking tests, fractographic studies of the surfaces involved to determine the origin and the breaking mode of the material considered, are carried out. [7]

1.1 Historical aspects

Total hip arthroplasty today is a staple of orthopedic surgery worldwide thanks to new technologies and new materials that have allowed patients undergoing this surgical operation to improve their daily lives.

In the last century, the diseases related to the hip joint were associated with age, while there were few occasions in which surgery to relieve the pain was taken.

From the late 1800s, the Frenchman Ollier tried to reconstruct the damaged bone surface through the interposition of the peri-articular connective tissue and muscle flaps. In the following years, there followed a series of attempts aimed at the replacement of the joint but without great success, as the operation performed by Gluck with a prosthesis in ivory or with the prosthesis in platinum by the French doctor Jules Pean in 1890. [8]

In the early 1900s, Hey and Groves performed for the first time the replacement of the femoral head with an ivory cephalic prosthesis, while in 1923, scientists Smith and Petersen defined the first arthroplasty cup. [9] [10]

This glass object was coated with tissue like the synovium and positioned between the acetabulum and the femoral head; unfortunately, the glass turned out to be too weak to resist the loads of daily effort that the articulation was subjected. It was fundamental to study and concentrate on inert, biocompatible materials with high resistance to mechanical stress.

New materials were then thought, such as Bakelite or Vitallium (the latter an alloy made of chromium, cobalt, and molybdenum), that turned out to be biologically inert and with excellent mechanical resistance. [11]

The first total hip arthroplasty implant was performed in 1938 by the Londoner P.W. Wiles, the prosthesis was divided into two stainless steel metal parts congruent with each other, a screwed plate fixed the acetabular part while the femoral part was composed of a sphere fixed by a nail-washer system. Thanks to the study conducted by the London research group, in 1939, A.T. Moore and H. Bohlman developed a Vitallium endoprosthesis consisting of a solid sphere attached to a short-flanged stem.

In 1950, the two researchers examined the possibility of modifying the fenestrated stem in such a way as to favor bone growth through implantation. [8]

The British McKee and J.W. Farrar in 1960 signed a milestone in the development of arthroplasty; they studied the metal-metal articular coupling in chrome-cobalt, where initially the cotyloid component was provided with a return screw to be introduced into the ileum, then introduced a series of pins to facilitate the grip of the dome to the acrylic cement wall. [12]

The first coating prosthesis was produced starting in the 1950s by Charnley. The implant included a double cementless Teflon prosthesis and two fragile cups of about 2-3 mm in polytetrafluoroethylene. [13] [14]

This type of prosthesis, with metal-polyethylene coupling, in the short term, gave positive results while in the long-term, the results were highly conflicting with each other. The main problems related to this type of implant, associated with the fracture of the femoral neck or the necrosis of the head, were thought.

However, the underlying problem was the osteolysis caused by the wear debris released by the polyethylene. [15] [16] In fact, Teflon proved to be unsuitable due to the high rate of a tear in the medium to long term, and a high-density polyethylene in the subsequent prostheses was used. The results obtained over the years led Charnley to resize the measurements of both the femoral head at 22 mm and the outer diameter of the acetabular dome at 50 mm, thus calling the "low friction arthroplasty" (Figure 1).

For a long time, this type of prosthesis was the most used, and updated versions regarding the material and the surgical grafting technique are still used. [17]

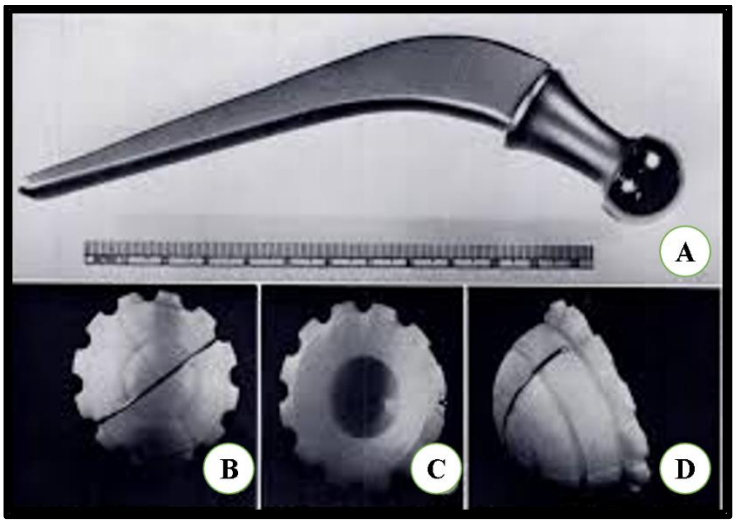

Fig.1: Historical picture of Charnley low friction total hip replacement; A) above the stainless-steel femoral component with a spherical, polished and small head, B), C) D) downward the high molecular weight polyethylene acetabular component.

In the seventies, Maurice Muller proposed a second-generation prosthesis modifying the stem in such a way as to be "self-locking" that can stabilize against the cortical femoral, with this model the cement was placed on both the anterior and posterior sides of the cortical while the stem it was in direct contact with the medial and lateral cortical.

Despite technological innovation, the long-term result was not satisfactory enough, especially regarding cement blocking and the problem of polyethylene wear debris. [18]

In the same period, Mittelmeier (1974) proposed the innovative ceramic-ceramic system (COC), among the best still today in terms of friction coefficient and debris formation, with a quadrilateral shank with different depressions to facilitate blocking; the problem that they were unable to solve resided at the level of the bone-ceramic acetabular interface. [19]

Between the years 70-80 began the study of artificial joints in alumina (Al_2O_3), Shikata proposed a type of alumina femoral heads with high molecular weight polyethylene component (COP). In recent years, the materials in alumina were intensively studied to obtain highly technological products with less porosity, excellent resistance to fractures, and density. [20]

However, although the initial results on the use of alumina were promising, the various applications in the orthopedics field found a high rate of fractures in vivo; consequently,

zirconia (ZrO_2) has been studied, having a rate of resistance to breakage and a mechanical strength higher than alumina.

The high mechanical capacity of zirconia is linked to a stress-induced phase change by its tetragonal metastable phase to its stable monoclinic phase at room temperature, respectively. [21]

In 1988, the previously studied metal-metal combined systems were revalued, introducing metals with a high content of carbides in the Metasul prosthesis of Sulzer Orthopedics with a shallow wear rate, thus opening the doors to the prostheses of coating like the one introduced in 1991 from Wagner: a cemented prosthesis characterized by two metal components each coated with titanium, with Metasul joint. [22] [23] At the same time in England, Corin Medical, in assistance to McMinn, proposed a non-cemented coating system with elements of chrome-cobalt and molybdenum. [24]

In the nineties, the use of zirconia in the femoral heads was quite widespread, particularly in conjunction with polyethylene (COP) bearings due to the high tenacity and mechanical strength.

However, tetragonal zirconia, following hydrothermal effects of in vivo degradation, turns out to be highly unstable and transforms with a raised conversion rate in its monoclinic phase. [25]

To address the problem in the early 2000s, two attractive ceramic-on-ceramic zirconia alternatives for bearings were proposed, one in which a surface with a thickness of a few microns through the oxidation of zirconium oxide (OxiniumTM of Smith and Nephew Orthopedics) was obtained [26]; the second one represented a mixture of alumina and zirconia, known as ZTA, in this case, suitable not only as orthopedic bearings but also for both COP and COC applications.

Zirconium ceramic compounds (ZTA) consist respectively of 80% polycrystals of tetragonal zirconia and 20% of alumina, with this weight distribution the mechanical properties are superior to both conventional alumina and zirconia. [27]

In 2003, CeramTec proposed a new category of ZTA femoral heads (BIOLOX®delta) consisting of new volume distribution of components: 82% alumina matrix, 17% yttrium stabilized zirconia, two minor additives to increase material hardness, 0.5% strontium oxide and 0.5% chromium oxide (figure 2). The fraction of yttrium oxide added to zirconia (1.3% moles) was intended to stabilize the tetragonal polymorph. [28]

Fig.2: BIOLOX®delta components provided by CeramTec.

To date, the materials in ZTA have a resistance and a toughness that makes the comparison with other materials difficult for the same purpose of use.

Nowadays, two biomaterials in ZTA are available on the market for hip arthroplasty, namely BIOLOX®delta from CeramTec Medical Products (Plochingen, Germany) and AZ209 from KYOCERA Medical (Osaka, Japan).

In the last few years, silicon nitride (Si_3N_4) has been studied initially for the resolution of arthrodesis problems in the cervical and thoracolumbar column, and subsequently, this material for the production of bearings for total arthroplasty of the femur will be studied. In favor of silicon nitride, there are different properties such as high hardness and fracture resistance, the inherent stability of phase, remarkable biocompatibility and hydrophilicity, and an essential resistance to bacterial activity. [29]

1.2 Total hip arthroplasty

An artificial articulation aims to realize a system that, respecting physiological kinetics, allows to bear loads and efforts minimizing wear and friction [30].

The functional anatomical specifications and the biocompatibility of the system must be considered during the design and construction of a hip replacement. Furthermore, it is necessary to guarantee the functionality of the prosthesis for many years, making the choice of the material used essential. Hip arthroplasty is an artificial joint consisting of metal alloys, plastic, and ceramic materials used to replace the damaged coxo-femoral joint.

In general, the hip prosthesis consists of two elements, a cotyloid cup, linked to the iliac bone of the pelvis, and a femoral element consisting of two areas: the neck and the stem, which are respectively inserted into the medullary canal of the femur.

Metal or ceramic femoral heads in the construction of the prosthesis are used, which in turn will assemble to the inner region of the cotyloid cup [31].

A prosthesis must have a series of requirements that make it suitable for use:

- Ensure the same degrees of rotational freedom between the femur and pelvis that a natural joint has;
- High resistance to stress during the daily load cycle of the subject operated both in the first postoperative period and in the long-term;
- Be made of particularly wear-resistant joint materials;
- Use of biocompatible materials that do not lead to unwanted reactions to tissues, thus affecting the mechanical stability between the prosthesis and the pelvis;
- Have the right elastic modulus to prevent micro-instability in the host bone.

1.2.1 Anatomy of the hip

The hip joint, shown in figure 3, consists of the articulation of the femoral head into the acetabulum of the coxal bone. Compared with the shoulder joint, it has more excellent stability and less freedom of movement.

The femoral head is composed of about two-thirds of a sphere and is covered with thicker articular cartilage in the upper part and is gradually thinning along the irregular termination line at the junction point between the head and the femoral neck.

The acetabulum of the coxal bone has an arcuate articular surface surrounding the acetabular pit.

The longest and largest main bone of the human skeleton is the femur and has a body called diaphysis and two irregular ends that are part of both the hip joint and the knee joint.

The upper end of the bone is made up of a spherical shaped head tied on an angled neck and the prominent trochanters serving as insertion for the muscles.

The femoral head is smooth, with a more full articular surface above and anteriorly, is also interrupted in the middle by the dimple of the femoral head, in which it inserts the ligament. The neck is compressed anteroposteriorly, has a large number of holes for the passage of blood vessels and is extended about 5 cm, forming with the diaphysis an angle that varies between 115 and 140 degrees.

The pit joint also receives a mass of adipose tissue covered by the synovial membrane; the transverse ligament of the acetabulum closes the inferior acetabular pit.

The acetabular lip is inserted into the bone contour and transverse ligament of the acetabulum. The joint area also receives a mass of adipose tissue covered by the synovial membrane; the transverse ligament of the acetabulum closes the inferior acetabular pit. The acetabular lip is inserted into the bone contour and the transverse ligament of the acetabulum.

The joint capsule is robust and relatively hard; adheres to the bone limit of the acetabulum and below the transverse ligament. It adheres before the intertrochanteric line and at the junction point of the femoral neck to its trochanters. Posteriorly, the capsule has a curved free margin that goes to the border with the lower part of the

femoral neck. Most of the fibers of the joint capsules have a longitudinal course, but other deeper fibers have a circular pattern. The longitudinal, iliofemoral, ischiofemoral, and pubofemoral ligaments are not dissociable from the capsules; in fact, they are nothing more than thickened portions of the capsules and are also called iliocapsular, ischiocapsular and pubocapsular ligaments [32] [33].

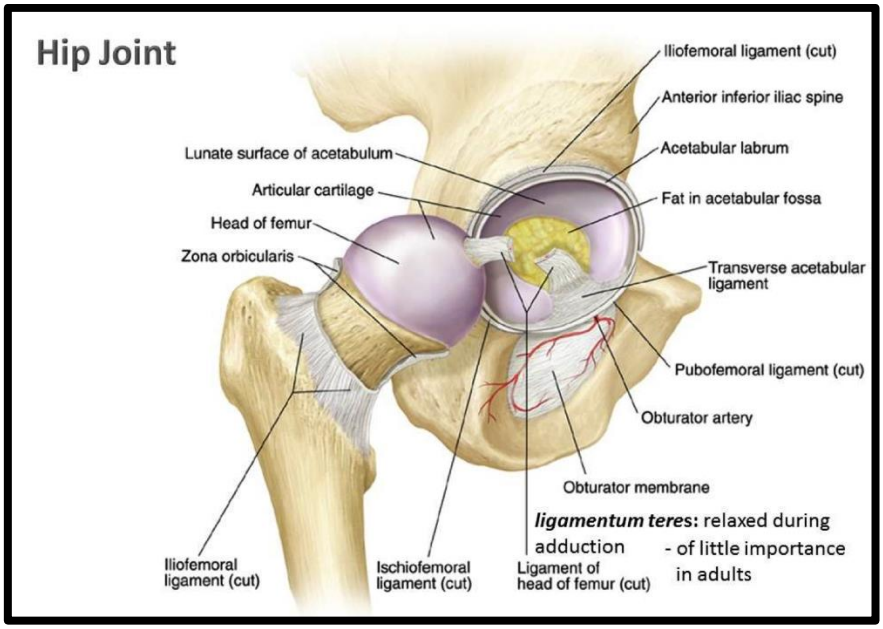

Fig.3: Anatomy of the hip.

1.2.2 Types of hip prosthesis

Throughout the years, fundamentally, three sorts of hip prosthesis have been produced [34]:

• TOTAL PROSTHESIS;

• ENDOPROSTHESIS;

• COATING PROSTHESIS.

Regarding the total hip replacement shown in figure 4, during the surgical operation, both the cotyloid component, including the prosthetic cup and the insert and the femoral component are replaced, with the removal of the stem and the femoral head. For the stem, metal materials are used, alloys based on titanium-aluminum and vanadium or

based on chromium-molybdenum-cobalt. The acetabular component can be composed either of a metallic mono-block or several parts, such as the metallic acetabular shell associated with an insert made of metallic, ceramic, or polymeric material.

The femoral head is composed of metal or ceramic material.

In most cases, in hip replacement, there are positive outcomes for patients over 55 years of age, while for younger patients, the failure of the prosthetic implant is more significant due to the high wear of the respective parts that make up.

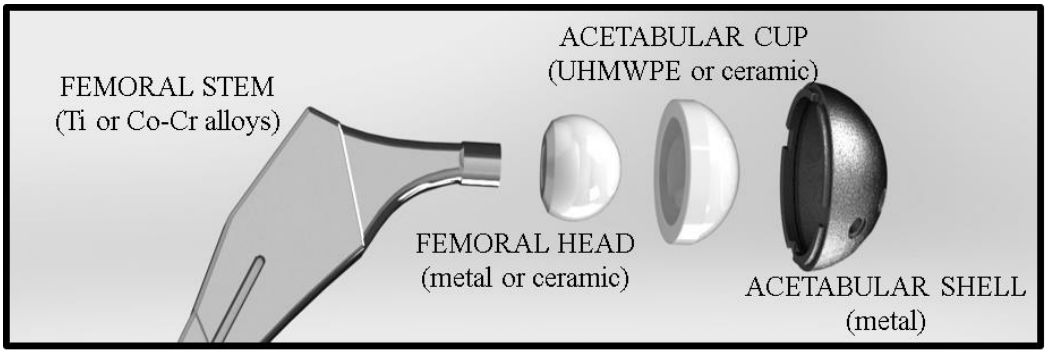

Fig.4: Total hip replacement components: from left to right, the femoral stem, the femoral head, and both the acetabular cup and shell are shown.

The two types of endoprosthesis are monopolar and bipolar, and the difference concerning the total prosthesis is that only the femoral part is artificially constructed (figure 5). In the monopolar endoprosthesis, the metal femoral head binds directly to the pelvis at the level of the acetabular cavity. This prosthesis is not widely used due to the excessive wear of the acetabular bone, due to the constant friction with the metal head.

The bipolar endoprosthesis, on the other hand, consists of a metallic cup that mainly performs two functions: interacting internally with the metal head and interacting with the cartilage of the acetabulum. This prosthesis for medial fractures of the femoral neck is recommended.

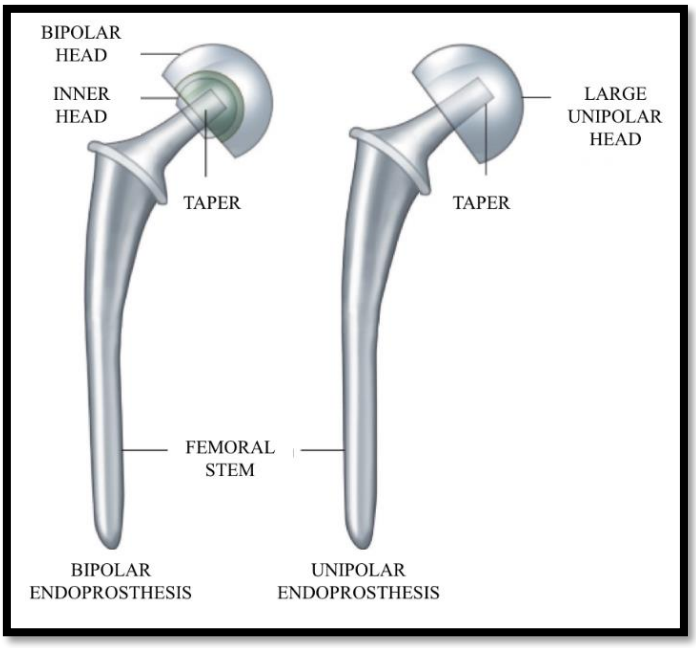

Fig.5: Two types of endoprosthesis: on the left is observed the bipolar endoprosthesis, on the right the unipolar endoprosthesis.

The coating prosthesis consists of the replacement of the articular surface, where the femoral head is covered with a molded hemisphere, thus avoiding the removal of the femoral neck. The new generation prostheses consist of a metal-metal coupling; usually, the primary metal alloy used is chromium-molybdenum-cobalt, to reduce the degree of wear and the production of friction, which are the leading causes of failure of the prosthetic implant. A further advantage in the use of coating prostheses is the ability to preserve a large amount of bone tissue, both the neck and the femoral head, while still guaranteeing the same dimensions in terms of diameter of the femoral head. This type of prosthesis is recommended for patients with high-quality bone tissue, although, unfortunately, it is not readily applicable to patients with joint deformations.

1.2.3 Components of total prosthesis

The total hip prosthesis can be divided into different parts (as shown before in figure 4), each with a particular function [35]:

- ACETABULAR SHELL

The acetabular shell is the part that is anchored to the pelvis through acrylic cement and screws; moreover, it is usually coated with hydroxyapatite with the aim of both promoting bone growth and promoting adhesion to the bone wall.

- ACETABULAR CUP

It is the element that fits into the acetabular shell, creating the new acetabulum ensuring freedom of movement to the entire prosthetic implant. The inserts have a variable diameter depending on the size of the cup and the femoral head. The acetabular cup is made up of different materials such as high molecular weight polyethylene, ceramic, or metallic material.

- FEMORAL HEAD

It is the spherical component that is coupled with the internal cavity of the cup forming the prosthetic joint; it is mainly made of ceramic material, and by conical coupling, it binds to the stem.

- METALLIC STEM

The stem of the total hip replacement is the metallic part inserted in the upper extremity of the femur and carries the head of the prosthesis. The materials used are titanium, steel, and a cobalt-chrome alloy. There are then two types of stems, respectively, the straight stems, which do not consider the femoral curves and are anchored in the femoral diaphysis, and then there are the anatomical stems that instead follow the femoral lines. The fixing step can be direct if the stem has been previously treated with calcium hydroxyapatite.

- FEMORAL NECK

The neck corresponds to the upper end of the femoral stem, which carries the prosthetic head. The stability of the prosthesis depends in no small extent on the neck since this must both reproduce and correct the anatomical position of the neck. In standard prosthetics, the neck is an integral part of the femoral stem and makes it challenging to correct parameters such as femoral torsion, the length of the neck, or the angle that it creates with the femoral diaphysis. In modular prostheses, the neck is separated from the stem in which it will be inserted. The different inclinations and lengths available make it possible to modulate the total hip prosthesis to reproduce or correct the patient's anatomy.

1.2.4 Causes that lead to hip replacement

The factors that lead to hip replacement and surgery are numerous and diversified [36]:

- FRACTURE

The femur is the most common fracture point, while fractures of the acetabulum and pubis are rarely observed. The fracture occurs in the bone, following a trauma, or following severe osteolysis around the implant; this disease is observed only for bone weakness.

- DISLOCATION

Dislocation of the femoral head from the acetabulum hole, in 1-3% of patients undergoing primary surgery, is observed. The main causes that lead to this problem are the patient's poor attention to post-operative precautions or malposition of the prosthetic components, with attention to the acetabulum during the operation.
Usually, dislocation and continuous loosening are the leading causes that lead to revision.

- DEEP VENOUS THROMBOSIS AND PULMONARY EMBOLISM

Thrombosis is the development of a thrombus inside the venous dividers that can show with different side effects or even with no kind of side effect. The risk of the thrombus emerges from the likelihood of either blocking a vein, making an inadequacy of the venous circle or disengaging itself, shaping an embolus which, by relocating, produces an impediment of vital vessels. An isolates thrombus pneumonic embolism can likewise prompt the patient's demise and should, in this manner, be dealt with or expeditiously forestalled. Extraordinary consideration has been paid to deep vein thrombosis and pneumonic embolism as the primary driver of mortality in patients experiencing total hip arthroplasty. Without prophylaxis, the rate of deep vein thrombosis can achieve 70%, though that of 20% pneumonic embolism. Mortality from aspiratory embolism is 2%. Usually, a low dose of heparin, antithrombin III, and warfarin are given as anticoagulants.

- WOUNDS COMPLICATIONS

In total hip arthroplasty, the most critical wound complications are the hematoma, whose complete rate is 3.5%, and the bacterial contamination that can present as an optional complexity. Hematoma can undoubtedly be considered a breeding ground for microscopic organisms. Some nearby skin changes that may aggravate the wound mending are flare, hypertrophy, necrosis, and septic complications. In any case, superficial trauma diseases are rare and must be separated by profound contamination, including prosthetic segments.

- INFECTIONS

A serious problem concerns the possible bacterial contamination of the prosthesis; even a minimal presence of bacteria on the implant can lead to its malfunction. These microorganisms can adhere to the walls of the tissues and prostheses, quickly forming multilayer chemical and physical barriers. These multi-layer structures are called biofilms and work by protecting bacteria from the attack of anti-biotic drugs or the immune system. Bacterial contamination is the most common cause of acute and chronic infections and, in some cases, of irreversible infections resulting in the removal of the prosthesis [37].

- WEAR PROSTHETIC COMPONENTS

Since its first use, the prosthesis has been continuously subjected to wear and probable formation of bone debris. By studying the regular use of the prosthesis, it is observed that, due to the considerable contact forces placed at the interface between the femoral head and the acetabular cavity usually, the material of the acetabular cavity is repeatedly scratched. These small particles lead to a progressive inflammation of the affected area, and at the same time, the reaction of the immune system is triggered that through the macrophages, it tries to engulf the debris of the material. At this point, the macrophages are not able to digest the foreign particles, and consequently, they become more prominent and melt together, generating particles with an even larger size. These particles called "Langhans cells" gradually lead to chronic inflammation with subsequent mobilization of the prosthetic implant [38] [39]. A second consequence of the recall of macrophages in the production of cytokines, protein molecules capable of modifying the behavior of other cells by inducing cell growth or death. The cytokines support both the action of osteoclasts, which "phagocytize" the bone, and fibroblasts that produce bone tissue; the result is the disappearance of the bone tissue. Further wear of the prosthetic components also leads to the disappearance of the coupling and alignment between the various components with incorrect patient deambulation [40].

- ASEPTIC LOOSENING

One of the leading causes that lead to the failure of the hip prosthesis in the long term is the aseptic loosening of the implant. The loss of fixation of the prosthetic component is not associated with infectious phenomena but linked to periprosthetic bone reabsorption that can be detected, especially in very young individuals with high body mass. Moreover, failure to fix the stem or acetabular shell is often due to the erroneous execution of the surgical operation.

Wear often contributes to the relaxation of the acetabular cavity, and this leads to a series of complications that are difficult to detect in a simple radiograph.

Following the surgical operation, in all cases, the formation of a soft tissue layer at the bone and implant interface is observed, mainly consisting of bone residues not suitably removed, organic fluids, or blood clots linked to the healing process. Unfortunately, in cases where the amount of soft tissue is too high, and no case of reabsorption or

osseointegration is observed, the prosthesis undergoes a gradual deterioration with subsequent prosthetic failure [41].

- BREAKING OF PROSTHETIC COMPONENTS

The rupture of a part of the prosthesis can occur in concomitance of severe trauma or due to minor but continuously repeated injuries. The parts of the prosthesis that are most prone to breakage are the neck, the root, and, more rarely, the acetabular head and the head of the femur.

1.3 Total hip arthroplasty materials

In the 21st century, medical engineering is a vital place for technological improvement. The design, development, and manufacturing of medical implants that update failed body or organ functions are of first-rate significance for a growing old population. This led to the study, analysis, and design of medical implants that can replace the mechanical functions of human limbs entirely or partially. Biomaterials are synthetic materials used to increase elements and update a body component or feature of the frame part safely and dependably. Biomaterials used in the human body need to be inert and routinely sturdy enough to endure the burden. Biomaterials are expected to work satisfactorily in a body environment, where the pH cost of body fluid varies from 1 to 9. During day by day, sports bones are subjected to the pressure of approximately 4MPa, and the mean load on the hip joint is three times the body weight. The peak load on the hip joint throughout leaping time can be up to ten instances of body weight; once more, those stresses are repetitive and fluctuating [42].

THA is taken into consideration one of the greatest fulfillments in orthopedic surgical operation, from an engineering factor of view. Today THA is not only applicable to generations of older people, but it is also applicable to young children, subject to the greater movement. So, trying to prolong the life of the prosthetic implant requires even more attention. The aim of developing an alternative THA fabric is to create a joint with

reduced friction and applied rates but with better resistance.

The biocompatibility of material must be evaluated as a feature of its precise utility. Its interplay with the body environment can provide variety from no interaction, the bio-inert case, to the most for bioactive or bio-resorbable matrices.

A prosthesis must have the following requirements [43]:

- STRUCTURAL ASPECTS

Since the hip is the body's second-largest weight-bearing joint, the prosthesis ought to showcase good enough mechanical energy and fatigue power; then, it needs to face up to hundreds of thousands of automatic loading cycles without fracture.

- TRIBOLOGICAL ASPECTS

The articulated surfaces must guarantee the appropriate relative movement of the musculoskeletal device without being compromised by excessive use.

- BIOLOGICAL ASPECTS

Stem and shell and all prosthesis components ought to provide right osteointegration, must resist the highly corrosive body environment, and the unavoidably released wear debris need not damage the organism.

Thus, the structural and bearing components must be bioinert. In contrast, inside the case of cementless fixation, stems and shell of the acetabular cup should exhibit bioactive surfaces for desirable osteointegration at the same time.

1.3.1 Metallic materials

Metals are necessary for orthopedic applications due to the fact they exhibit extended mechanical power and fracture durability, the capacity to contain a crack and to withstand fracture. Today three groups of metals are prevailing for applications in joint replacements: stainless steels, Cobalt-chromium-molybdenum (Co-Cr-Mo) alloys, Titanium (Ti).

- STAINLESS STEELS

Austenitic stainless steels include essential alloying elements chromium (Cr), nickel (Ni), molybdenum (Mo), nitrogen (N), and usually exhibit top corrosion resistance. Composition, treatments, and features of wrought stainless steels are classified inside the standard ISO 5832-1 (implants for surgery – metallic materials). Stainless metallic alloys are economical but have restricted resistance towards localized crevice corrosion. Moreover, their high content material of Ni represents a likely supply of Ni sensitization for patients who have received a stainless-steel hip implant. Stainless steel with expanded Ni content material showed off better corrosion resistance and progressed mechanical traits, which entail more complicated production methods and higher cost. [44]

- COBALT-CHROMIUM-MOLYBDENUM

Cobalt-chromium-molybdenum (CoCrMo) alloys in two major categories are divided: alloys that has been utilized in dentistry for a long term and presently in making artificial joints and wrought alloys that is a comparatively new material that is now used for getting ready the stems for the prosthesis of firmly loaded joints such as the knee and hip. CoCrMo significantly increased mechanical proprieties and the most advantageous corrosion resistance below the friction situation [45].

Its fundamental drawbacks are related to their weak fatigue resistance and their high cost. Wrought CoCrMo is even extra expensive than cast material, but the higher price can be justified through the enhanced corrosion and fatigue resistance. The presence of Ni creates some issues concerning viable nickel sensitization. In assessment to cast

CoCrMo, the tribological qualities of wrought CoCrMo are too adverse for bearing surfaces. However, due to the corrosive environment in the human body, factors including Ni, Cr, and Co turned out to be released from the chrome-stainless steel and cobalt alloys. Co-Cr-Mo corrosion products are more poisonous than chromium-plated steel [46] [47].

The added advantage of totally cobalt-based alloys is considerably corrosion-resistant even in the chlorine environment due to the formation of the oxide layer in the environment of the human body. They have advanced mechanical properties together with high resistance to fatigue and cracking due to corrosion with remarkable resistance to wear, although these substances have a high elastic modulus (220-230 GPa), which is greater than that of cortical bone (20-30 GPa).

- TITANIUM

Titanium primarily based alloys are also popular in THA, because of its characteristics like low density (approx. 4700 Kg/m^3), excessive strength or good resistance to corrosion due to the formation of an adhesive TiO_2 oxide layer and entire inertness together with biocompatibility. However, the harmful mechanical properties of natural Ti, which include small Young's elastic modulus and low fracture strain, have restrained its utility in joint alternative [48].

Ti and Ti alloys are wear-resistant due to low shear resistance. Two Ti-based alloys for implants are commercially natural Ti and Ti_6Al_4V; however, thanks to its high mechanical power, Ti_6Al_4V is a substitute for commercially natural Ti.

Long-time period using Ti alloys creates health hassle like Alzheimer's ailment and neuropathy, which mainly arises because of the release of aluminum and vanadium. Although vanadium is a vital element inside the human frame, the extra level is poisonous, and it can worsen when implant fractures. The extreme trouble related to Ni-Ti alloys is the discharge of Ni ions, which might be allergic, toxic, and probably carcinogenicity [49].

1.3.2 Polymeric materials

In 1962, Sir John Charnley proposed a metal hip prosthesis on polyethylene with self-polymerizing bone cement in polymethyl methacrylate (PMMA) for fixation. Already since the 70s, the method proposed by Charnley became the standard for THR, with the fixation of bone cement with a metal stem and the femoral head rested on a high molecular weight polyethylene (UHMWPE) liner.

Among the properties of polymeric materials stand out the low cost and the high mechanical and physical properties; moreover, the considerable biodegradability is essential [50].

There are biostable polymers such as polyethylene (PE), polymethylmethacrylate (PMMA), or polyetheretherketone (PEEK) that can be used positively in hip and dental implants. High molecular weight polyethylene (UHMWPE) for hip and knee joints is often being used. The second category of polymers is that of biodegradable polymers such as polycaprolactone (PCL), polyglycolic acid (PGA), polylactic acid (PLA), and poly co-glycolic acid (PLGA), which can gradually be absorbed by the physiological environment [51].

During the activity, the implant and the bone are inconsistently loaded, resulting in a different distribution of effort. In this case, the suitable material must have a low modulus, and one of these is the polymeric material; on the other hand, however, if the low modulus is associated with low power, the polymer is limited in its use.

For performance in the immediate period, a UHMWPE guarantees an excellent performance, but in the long term, it is still to be optimized, trying to improve rigidity, slip resistance, and power.

Some examples of composite polymers are carbon fiber with very high molecular weight polyethylene (CF / UHMWPE), carbon fiber with epoxy resin (CF / epoxy resin), and CF with PEEK.

One of the main errors related to total hip replacement is the lack of a link between the stiffness of the femur bone and the prosthesis, considering that the stems used in the prostheses are about 5/6 times more rigid than the bone. Consequently, aseptic loosening and failure of the prosthetic implant are expected.

By improving the design of the prosthesis and the quality of the materials, it is possible to reduce and solve the problem of failure of the implant, thus obtaining mechanical properties like the bone. The composite polymeric material also guarantees excellent resistance and flexibility, which are a fundamental requirement for the design of a hip prosthesis.

- ULTRA HIGH MOLECULAR WEIGHT POLYETHYLENE

Ultra-high molecular weight polyethylene (UHMWPE) is a subset of semi-crystalline thermoplastic polyethylene materials [52]. UHMWPE is a tough material, with a considerable impact on strength. It is relatively resistant to corrosive chemicals except for oxidizing acids, is a material with a very low friction coefficient, is self- lubricating and resistant to abrasion. However, UHMWPE has a friction coefficient similar to the polytetrafluoroethylene (PTFE) and, on the other hand, has higher abrasion resistance than PTFE [53].

In overall hip replacement system commonly applies ultra-excessive-molecular-weight polyethylene (UHMWPE) insert that articulates in opposition to a cobalt-chromium alloy or ceramic to reinstate the function of a broken joint. Although the abilities of the composite polymer are appropriate for total hip replacement, there may be no appreciable distinction wear rate of reinforced and unreinforced UHMWPE. Often carbon fibers are used to reinforce the UHMWPE and improve the mechanical properties, but the impact of carbon fiber reinforcing on wear function of UHMWPE is uncertain [54].

The destructive debris generated by excessive wear of the UHMWPE causes periprosthetic osteolysis and results in THR failure. In the last years with enhancing the wear resistance, crosslinked and thermally handled UHMWPE evolved for THR, the so-called first-technology highly cross-linked polyethylene (HXLPE). Cross-linking UHMWPE can be finished utilizing producing unfastened radicals along the backbone of the long chains that make up the polyethylene molecules. The unfastened radicals produced in adjacent chains integrate, forming carbon-carbon covalent bonds, which are the so-known cross-links [55].

The crosslinked components are finally stabilized by heat treatments (including anti-ageing treatments), including vitamin E, to avoid the oxidative effects of irradiation and

to maximize the quality of the cross-linked form. During the laboratory experimentation, it was observed how these coatings underwent a 95% lower degree of wear compared to the classic highly crosslinked UHMWPE coatings. This new category of cross-linked polymers called X-UHMWPE or XLPE loses in terms of mechanical energy, increased fragility, but increases wear resistance significantly.
However, UHMWPE damage residues are still limiting the lifetime of hip implants of the "metal-on-polyethylene" models, as the release of debris triggers the immune system's reaction with failure of the prosthetic implant [56] [57].

1.3.3 Ceramic materials

Ceramics have been utilized in total hip arthroplasty since the 1970s. Despite the critical brittleness of ceramics, both the hardness and the wettability of ceramic surfaces bring about brilliant abrasion and wear resistance, ensuing in low wear rates. Usually for hip prosthesis are used three different ceramic materials: alumina, zirconia, and alumina-toughened-zirconia (ZTA), while still being studied are the ceramic materials based on silicon nitride [58].

- ALUMINA

Alumina represents the most important ceramics material in total hip replacement due to its excessive compression energy, high hardness, and its endurance to abrasion and chemical attack. Its hydrophilicity performs a crucial role in the wettability of its surface and, therefore, at the lubrication performance under friction.
However, aluminum oxide is a brittle material that is not able to withstand high impulsive tensile stresses.
Alumina is typically used for total hip replacement owning to its low friction and wear coefficient, makes it is appropriate for orthopedic bearing. Comparative to alumina, zirconia offers extra flexure resistance fracture toughness and fracture resistance. Alumina does not guarantee a long life in its use; consequently, the zirconia has been introduced to replace the alumina, thus significantly improving the resistance to wear.

- ZIRCONIA

Zirconia has three different crystallographic phases, a monoclinic, a tetragonal, and a cubic. In many cases, zirconia is mixed together with low percentages of yttrium oxide (Y_2O_3) to stabilize the tetragonal phase at room temperature. Among the different crystallographic phases, the tetragonal phase presents the best mechanical properties, and consequently, in industrial processes, it is tried to obtain this phase in the finished component. To date, tetragonal zirconia stabilized with yttrium is the standard used for the hip replacement operation [59].

- ZIRCONIA TOUGHENED ALUMINA

For the hip replacement operation, the ceramic material known as ZTA has been very successful; it is composed of an alumina matrix with dispersed zirconium particles, thus improving the overall capacity of alumina in terms of strength and toughness.

The main characteristic of zirconia is that of being a polymorphic substance, which is, therefore, able to change its crystalline structure while maintaining the initial chemical composition.

During the cooling phase, a slow change from the tetragonal zirconia to the monoclinic zirconia is observed with an increase in the volume of about 3-5%, causing an expansion of the zirconia grains. [60]

This non-diffusive and automatic mechanism under certain conditions, when there is a high variation in free energy, is exploited to improve the mechanical properties of the composite material. Furthermore, as stabilizers of the tetragonal phase, oxides with a stabilizing function such as yttrium or cerium are added. [61]

1.4 Zirconia toughened alumina femoral heads

In this section, we will discuss the topics concerning a particular ceramic material used for artificial femoral heads, focusing on the properties of the zirconia toughened alumina.

In the second half of the 1970s, were studied new ceramic materials; one of these was characterized using zirconium oxide in different percentages in an alumina matrix, thus obtaining a modern high purity ceramic material. [62]

The Zirconia-toughened-alumina has the right mix between the mechanical properties of alumina and zirconia Y-TZP, alumina exerts a force on metastable Zirconia grains, guaranteeing more excellent stability in that phase. The hardness of the material is due to the slow transformation from tetragonal to the monoclinic phase of zirconia grains. This transformation is mainly due to the difference in elastic modulus between the zirconium-alumina particles and the matrix, and the cracks are induced to move around the zirconium oxide rigid particles, inducing their T-M dissipating transformation stage then the crack energy. [63]

The micro-cracks cause a second dissipative effect in the generated matrix with consequent expansion in the volume of the dispersed zirconium particles.

For this reason, a series of metal oxides are used to limit the growth of the grains and greatly improve the mechanical properties of the material.

Strontium oxide (SrO), to create structures in situ during the synthesis phase, is added in an elongated shape to slow down the possible propagation of internal cracks; in fact, in this way the split to spread in the material needs more energy to get around the obstacle and in this way, the propagation stops.

A second oxide used in the initial mixture is chromium oxide (Cr_2O_3) used to guarantee and preserve the hardness of alumina.

In addition to these oxides, yttrium oxide (Y_2O_3) is introduced to improve the stability of zirconia and slow down its growth and transformation. [64]

As mentioned, the properties of ZTA are strongly influenced by the mixed behaviors of alumina and zirconia.

The high breaking strength shown by many zirconium ceramics is attributed to the bond that occurs during the transition from the tetragonal to the monoclinic phase.

Despite the remarkable advantages of this material, there are also weak points such as the resistance and stability of the zirconia grains that are compromised following prolonged exposure of the grains to an environment rich in water vapor at temperatures between 30 and 300 degrees. This process is known as low-temperature degradation (LTD). [65]

Before studying the mechanism that leads to the phase transformation of zirconia, an essential aspect in ZTA ceramic materials, it is necessary to study the different phases that compose it and the temperatures to which it is stabilized.

Zirconia has three different allotropic forms, monoclinic (M) cubic (C) and tetragonal (T). At room temperature, the zirconia is detectable in the monoclinic phase and is stable in these conditions up to 1170 degrees; increasing the temperature, there is a passage to the tetragonal phase which maintains its stability up to 2370 degrees after which the cubic phase occurs (Figure 6).

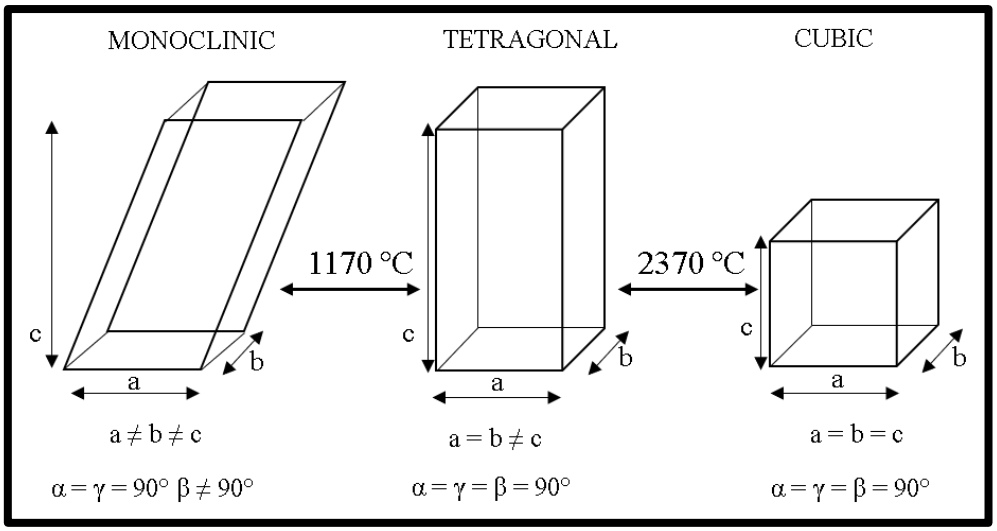

Fig. 6: Allotropic forms of Zirconia.

Generally, after cooling, a transformation from tetragonal to monoclinic is observed, with subsequent expansion in the volume of about 3-4%. [66-67].

Following the volumetric expansion, there are intense stresses inside the material that lead to the birth and propagation of cracks. A technique used to prevent the spontaneous transformation of T-M during cooling is to proceed through low-temperature sintering, to stabilize the different phases at room temperature.

As mentioned above, different oxides (CaO, MgO, CeO, Y_2O_3) are used and based on their percentages, three different categories of zirconia-containing ceramic compounds can be distinguished: a material containing completely stabilized zirconia called FSZ, one with zirconia polycrystals PSZ and one containing partially stabilized tetragonal zirconium grains TZP.

Generally, the TZP in the presence of either yttrium oxide (Y-TZP) or cerium at low weight percentages (about 2-3%) is stabilized. [68]

The ZTA ceramic materials have the typical mechanical-physical characteristics of Y-TZP, the grains dispersed on the alumina matrix consist of tetragonal zirconium with a granulometry of about 100nm. The tetragonal fraction kept stable at room temperature depends on various factors such as the size of the grains, the percentage by weight of yttrium, and the stress applied on the grain.

The nature of stable tetragonal grains depends on the concentration of yttrium oxide; if the critical dimension threshold is exceeded, then the T-M transformation takes place below the minimum threshold, and the transformation is inhibited due to too fine grain size. [69]

Two fundamental aspects of being considered in the study of the ZTA are both the formation of stress on the external surface with crack propagation towards the internal part of the material, and the ability of the zirconia grains to increase mechanical strength and toughness; this is possible because as the crack advances the energy associated with the fracture is dissipated. [68-70]

In detail, on the surface, the tetragonal zirconia grains free and not bound by the matrix, can freely transform into the monoclinic phase if subjected to harsh treatments, with consequent formation of compressive stress up to several microns of depth from the external surface.

It is also observed in figure 7 that in response to the propagation of the crack inside the material, there is an automatic T-M phase transformation, in this way, there is an increase in the hardness and tenacity of the material and the energy accumulated by the

crack propagation it is dissipated both in the transformation itself and in the increase in volume of monoclinic zirconia grains (3-4%).

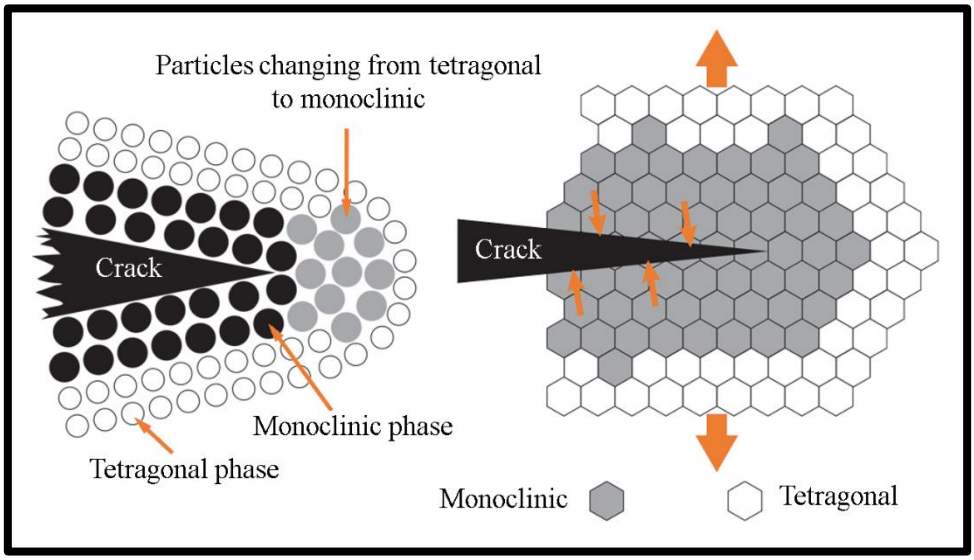

Fig.7: Crack propagation pattern.

Moreover, thanks to the phase transformation, it is easy to proceed with fractographic studies of the surfaces involved to identify the causes and reasons that led, for example, to the propagation of cracks inside the ceramic material.

From these considerations, it is clear that the phase transition and the subsequent hardening play a key role in understanding the mechanical properties, especially for biomedical implants such as joint prostheses.

2.FRACTOGRAPHIC ASPECTS OF BIOCERAMIC MATERIALS

In the main fractographic analyses the first step is to try to identify the origin of the fracture, then through the analysis of the fracture surface (FSA), it is possible to identify the cause of the failure, the amount of residual stress and the development of a crack before catastrophic failure. Quantitative fractography is a necessary tool for the analysis of fragile materials. The fractographic analysis is useful not only to identify the origin of the error but also to determine whether the material problem is caused by a processing or production defect. To understand the work presented in this thesis is necessary to introduce some critical elements for the study of fracture surfaces of femoral heads in ZTA subjected to burst strength standard test ISO 7206-10.

2.1 Relationship between crack velocity and fracture surface structure

2.1.1 Fast crack propagation

Ceramic materials have fascinating characteristics. The covalent or partially covalent ionic bonds that bind together the atoms of these materials are powerful; consequently, they are characterized by high chemical inertia, a high elastic modulus, low density, and a considerable hardness. The same chemical bonds that give them these important characteristics are also responsible for their fragility. They do not allow the crystalline planes to deform plastically, and consequently, the ceramics break with a mechanism

typical of fragile materials: the fracture propagates quickly in the material, suddenly and without any warning.

If the materials have surface irregularities such as cracks or defects, when tensile or compressive stress is applied; it is possible to calculate the intensity of stresses at the tip of the crack, which can be expressed utilizing a constant of proportionality K_I (stress intensity Factor) characteristic of the material.

In the equation shown in figure 8A, "a" represents the length of the surface fissure, and "Y" is a geometric factor linked to the morphology of the defect.

When, on the other hand, the K_I limit value is exceeded, it is possible to calculate the K_{IC} fracture resistance value, which also depends on temperature, type of ceramic material, and thickness of the defect.

In a fragile material, a crack can propagate when the decrease inelastic deformation energy is at least equal to the energy required to create a new fracture surface when the energy produced by an effort is spent to develop a new fracture surface.

The fracture resistance of a brittle material "σ_R" is expressed in figure 8B.

To improve the mechanical properties of ceramic materials by limiting brittle failure, either composite materials are used to try to obtain an increase in the matrix toughness or tried to optimize the initial formulation of the product, minimizing initial defects.

A) $K_I = Y\sigma\sqrt{a}$ B) $\sigma_R = \frac{K_{IC}}{Y\sqrt{a}}$

Fig.8: Stress intensity factor (A) and fracture resistance (B) equations.

2.1.2 Subcritical crack growth

An essential aspect of fragile materials is their susceptibility to the slow growth of cracks (SCG), and as seen in the previous paragraph, there is a correlation between K_{IC} and σ_R that often leads to a failure of the ceramic material despite the intensity factor K_I being maintained below the critical K_{IC} value.

The process that is verified is known as subcritical propagation of the cracks, with consequent expansion of the crack even below the critical K_{IC} value. The growth and propagation of the crack that occurs below the minimum values of the intensity factor depend on the applied loads, environmental conditions, the presence of water or steam. When the length of the crack is so considerable as to cause the failure of the material instantaneously, here it is possible to calculate the fracture resistance factor σ_R shown in Figure 8B.

The subcritical growth of cracks in ceramic materials is linked to stress and corrosion mechanisms that occur at the tip of the crack in a watery environment, reducing surface energy and inducing propagation. An estimate of the SCG is expressed by the relationship between the crack propagation speed with the stress intensity factor (v-K_I curve). [71] Experimentally three different phases are observed (figure 9), the first in which the propagation depends on the kinetics reaction on the tip of the crack between the molecules of the ceramic material and the water; in the second phase the breaking speed stabilizes, and it is observed that the reaction which induces surface expansion is faster than the transport of water molecules; in the third phase, there is an increase in speed regardless of the environment. [72]

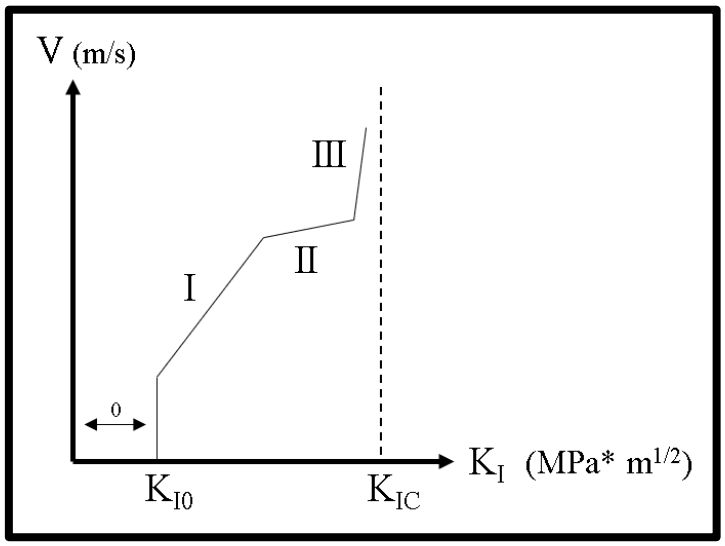

Fig.9: Schematic representation of the three regions observed during the Slow Crack Propagation.

In the v-K_I curve, there is a threshold known as "K_{I0}", below which the crack propagation is zero. In this area, zero speed is synonymous with a state of equilibrium of the crack.

In the study of ceramic femoral heads, this threshold guarantees the operating interval to work in safety; if the threshold is extensive, then the reliability of the product and the respective duration will be better.

Figure 10 shows the interaction mechanism on the tip of the crack between the water molecules and the zirconia molecules, in a humid environment. The main steps are the adsorption of water to the Zr-O bond, the transport of electrons and protons, and the creation of new surface hydroxyl complexes. [72]

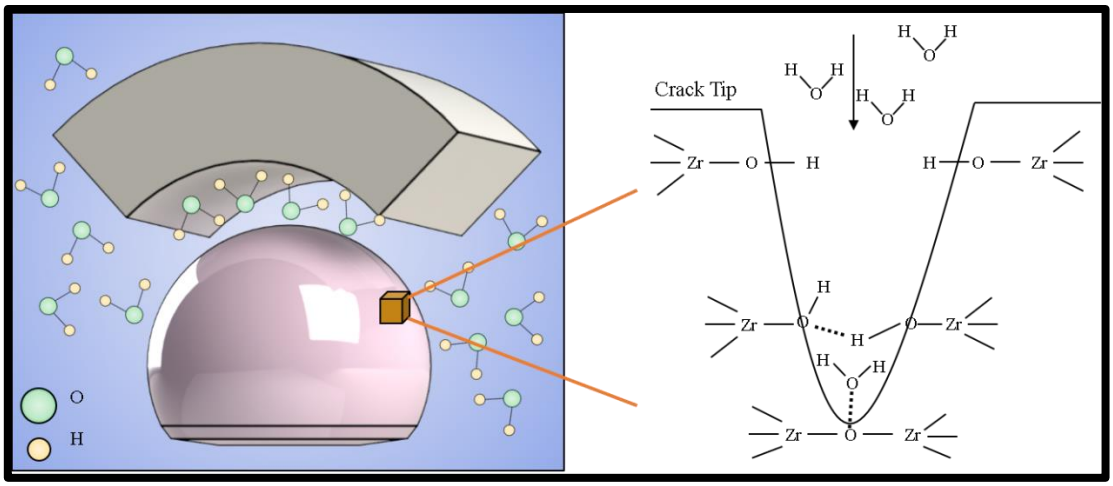

Fig.10: Reaction between water and strained Zr-O-Zr bond at the crack tip.

In recent years the v-K_I curves of different ceramic materials have been studied, comparing the thresholds of the zero region, where there is the minimum crack propagation value, the slopes, and the position of the intensity factor K_{I0} and K_{IC}.

Figure 11 shows the curves of Al_2O_3, Y-TZP, and ZTA (10% of zirconia). From the comparison, different behavior for the different materials is observed; alumina shows a higher slope of the curve due to lower susceptibility to water and the consequent corrosion. ZTA ceramic material presents the mix of characteristics of the single monoliths with a slope like alumina, with at the same time a shift towards large values

of the intensity factor. The toughening mechanism causes this shift towards larger K_I due to the presence of zirconia (10%).

In this way, the reliability threshold is made more extensive compared to monoliths, without neglecting some typical characteristics of alumina such as hardness and stability. [72]

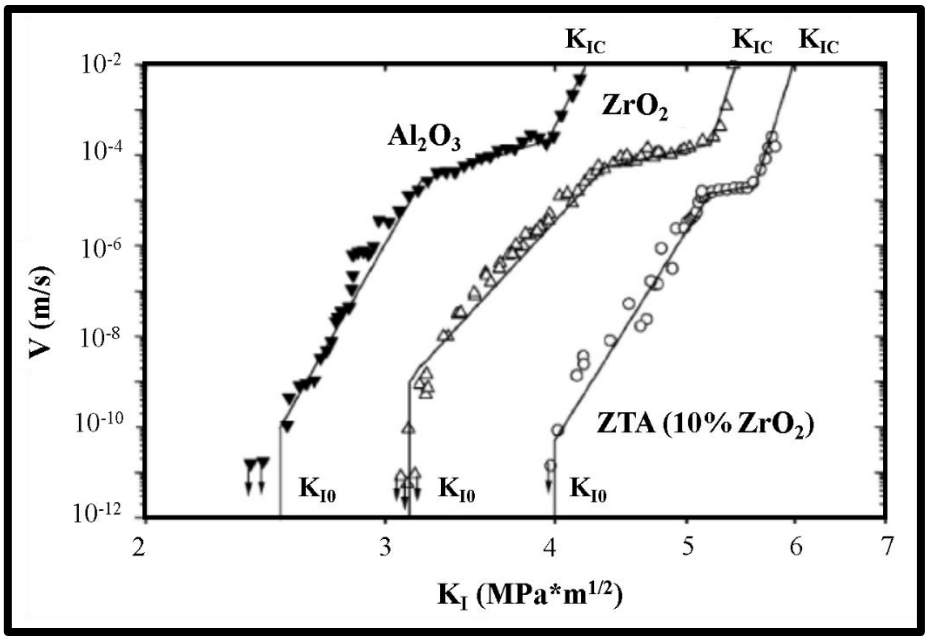

Fig.11: v-KI diagram of Alumina, Zirconia (Y-TZP) and ZTA (10 vol.% ZrO_2).

The ZTA toughening mechanism, as seen previously, due to the action of zirconia in the composite material, causes the shift towards higher values of the intensity factor.

The ability to resist fracture is caused by various phenomena such as the phase transition, from tetragonal to monoclinic, induced by stress with an expansion in the volume of about 4%, or by the interaction of the front of the crack with microcracks.

In ZTA composite materials, the toughening mechanism linked to the increase in K_{IC} and the increase in structural properties of the mechanical properties also depends on other factors such as the distribution of zirconium grains, the grain size, and the homogeneity in the grain distribution. [73] [74]

2.1.3 Ageing in ZTA

In recent years the effects on the change of mechanical properties of alumina reinforced with zirconia subjected to aging have been studied.

One way to proceed with the aging of the ZTA is to subject the material to heat treatment at low temperatures, in controlled conditions of humidity in an autoclave.

The mechanism of propagation of ageing is related to the phase transformation of zirconia from tetragonal to monoclinic, about 10% after only two hours, in samples containing a fraction of the initial weight of zirconia less than 15 wt %. In ZTA samples, with higher values than 16 wt % of zirconia, there is a further increase in thermal degradation with an increase in the monoclinic zirconia fraction.

Regarding the degradation mechanism, it must be considered that the transformation from tetragonal to monoclinic leads to volumetric expansion of about 3-4% with consequent formation of internal microcracks. Consequently, if the presence of initial zirconia is excellent, the phase transformation from tetragonal to monoclinic will be considered with a subsequent increase of cracks. Furthermore, an increase in cracks contributes to the diffusion of water, thus favoring the propagation of ageing. [75]

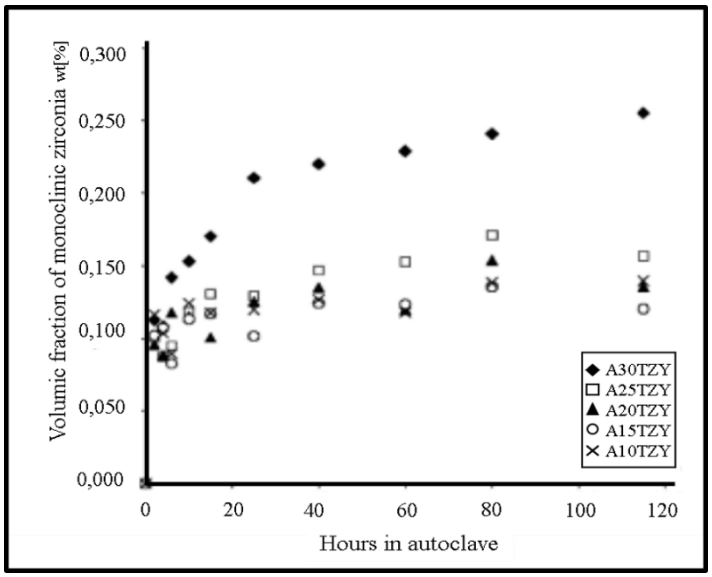

Fig. 12: Ageing of ZTA composites at 140°C with different wt % of monoclinic zirconia (10-15-20-25-30 wt %).

2.2 Surface fracture elements

It has been known that in ceramics, owing to its brittle nature, cracks extended under localized stress may become a trigger for instantaneous fracture.
The fractographic techniques represent a method of analysis for the study of the fracture surfaces of ceramic and glass materials. The study of the characteristics of the fractured surface can help to determine the cause of the failure in an engineered product.
As previously mentioned, fractography plays a key role in identifying the origin of the fracture in a fragile material, so it is possible to analyse the individual elements that characterize the surface fracture plan.

2.2.1 Fracture mirror

As the first step of the analysis, the operator must proceed with the identification of crack origin, where a particularly smooth and reflecting region, with a symmetrical shape (circular or semi-circular), is observed. Usually, the fracture plan is called "Fracture Mirror," a flat region surrounded by cracks with radial direction at the point of fracture and characterized by a high degree of transgranular fracture. [76]
Generally, the fracture mirror is not observed in materials that are too weak because the crack does not reach enough speed within the sample boundaries, but only in samples with high strength respect to the applied breaking load.
When the point where the breakage of the material originates is identified, the other elements that characterize the main fracture plane can be studied: the "mist region," the "hackle area," and the "twist hackle" (figure 12).

- "Mist region": the intermediate region between the smooth surface of the mirror fracture and the cracks radially directed towards the "hackle area."
- "Hackle area": a region where crack propagation is observed, usually characterized by a high degree of intergranular fracture, and formed when the fracture propagates very quickly.
- "Twist hackle": cracks formed as a result of torsion respect to the original fracture plane and are formed mainly at long distances from the mirror fracture.

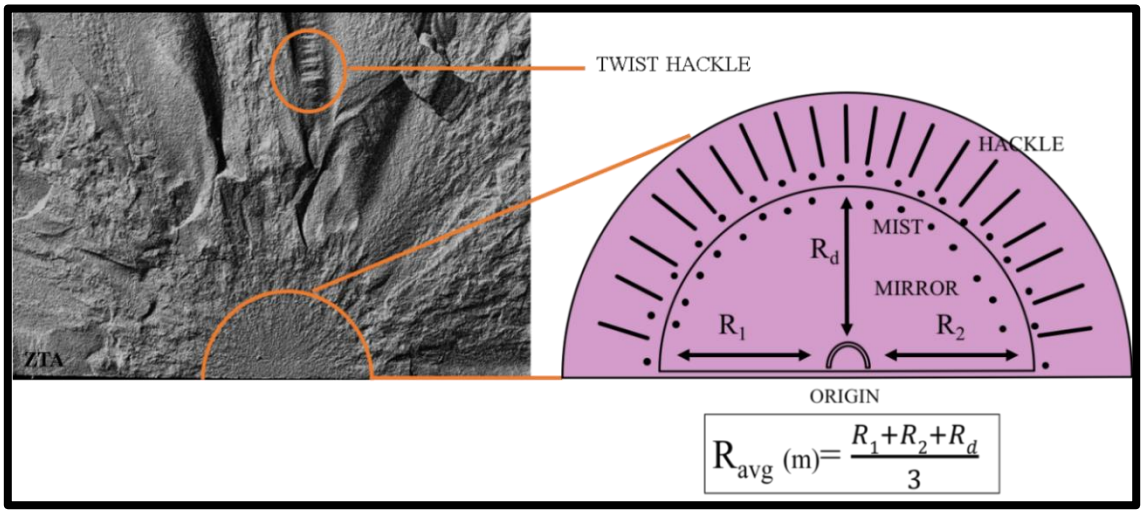

Fig.12: Schematic representation of a fracture mirror centered on a surface flaw, and evaluation of the average radius of the mirror area.

Thanks to high-resolution optical instruments such as the laser microscope, it is possible to calculate the average radius (R_{AVG}) of the fracture mirror, considering the three radial directions shown in figure 12 and reported in the formula.

The shapes of the mirror are often commonly influenced by the stress gradients in a plate or a beam, with elongation of the smooth reflecting area and in the direction of decreasing stress. Usually, mirrors are elongated in bending stress fields if the mirror is small compared to the size of the material, then the mirror may be semi-circular, as shown in figure 12. If instead the material is particularly weak or the fractures develop in weak parts of the ceramic material, the area of the mirror extends towards into the interior with loss of symmetry of the fracture plane. [77]

Starting from 1950, a method called "Kerkhof," in memory of its discoverer allows calculating the fracture propagation in ceramic and glass materials. This method is part of the discipline of ultrasonic fractography.

When there is a material in which there is an expanding crack, it is possible to calculate precisely the correlation between crack propagation speed and fracture surface structure. The method, known as ultrasonic wave fractography, is characterized by ultrasound waves of a known frequency that, when applied to a moving crack, there is a change of direction due to the periodic change of the principal stress direction.

Therefore, Wallner's artificial lines are left on the fracture surface, and the wavelength of these lines determines the fracture velocity; this implies that if the direction of the maximum principal tensile stress changes, the crack will change the direction of propagation. [77]

If ultrasonic waves periodically modulate the crack, the fracture velocity (v_f) is determined by the relationship shown in figure 13, considering the wavelength of the artificial Wellner lines (λ_b), the frequency of ultrasonic waves (υ_t) and the phase velocity of ultrasonic waves (c_t). [78]

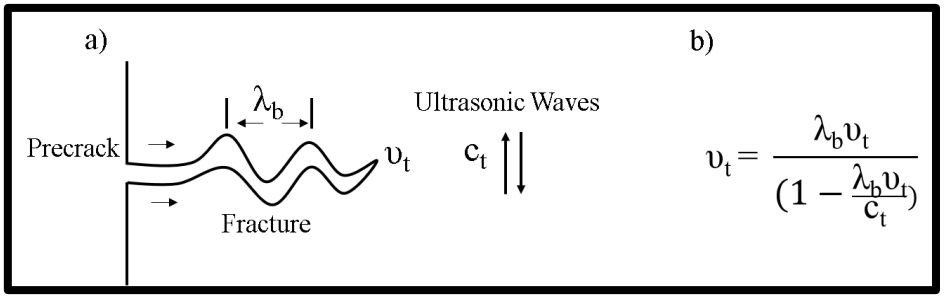

Fig.13: Ultrasonic modulation of a moving crack (a), fracture velocity relationship (b).

The ultrasonic wave fractography provides as a first thing the construction of the v-K_I curve seen previously in figure 11, so at each point of the curve, it is possible to attribute a specific morphological structure of the surface of the material.

When the fracture speed exceeds 800 m /s, the surface structure changes from "mirror" to "mist," while in the transition from the "mist" zone to the "hackle" the speed remains

almost entirely constant; in particular for ceramic materials, it is complicated to identify the "mist" region because the surface involved is particularly small.

Obviously, as the fracture proceeds, the intensity factor K_I increases.

Furthermore, it is clear that during the transition leading to the formation of the "hackle" there is a net change in the speed of propagation of the cracks, the energy that is released initially due to the formation of the smooth surface is not high enough to support the propagation of the areas of "mist" and "hackle" with the same speed.

Below in Figure 14 is proposed the correlation between the hypothetical v-K_I curves and the respective areas of the fractured material.

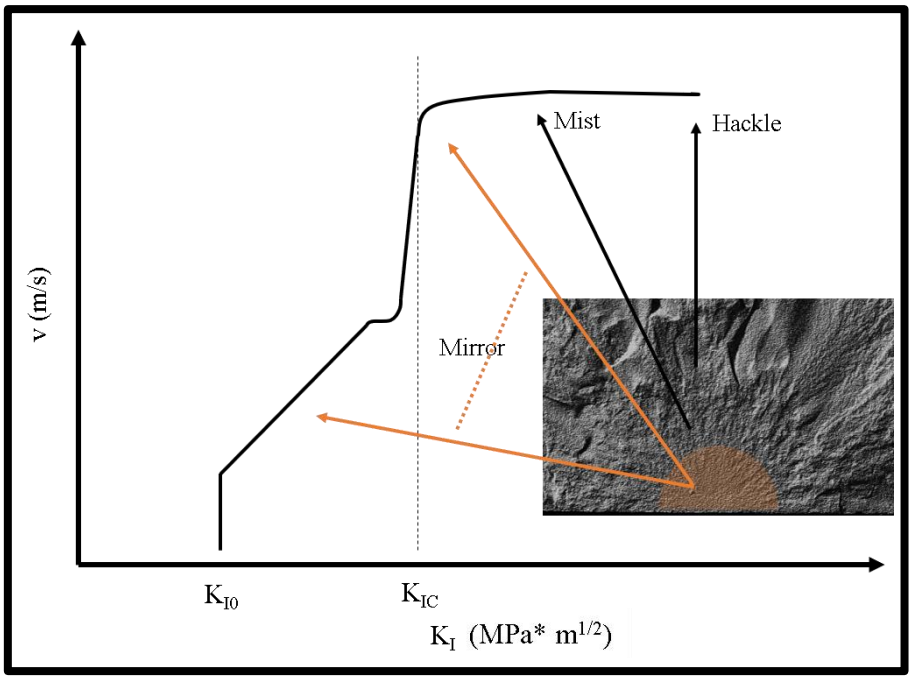

Fig.14: v-K_I dependence in fractured material (schematic) with the equivalent fracture surface structure.

2.3 Resistance to static load

All the ceramic materials used in the biomedical sector (example: artificial femoral heads) are, before being sold, subject to international standard tests.

In the case of artificial femoral heads, there is the international standard ISO 7206-10 test, the purpose of this test is to study the behavior between the artificial femoral head and the stem “neck” when they are subjected, under specific laboratory conditions, to tensile or compressive stress which causes failure or breakage of the sample.

Figure 15 shows the schematic arrangement of the components of the breaking test according to the ISO 7206-10 standard. The sample is placed on a metallic conical loading bore with Brinell hardness between 150 HB and 250 HB, and in the middle is arranged a copper ring (Young modulus: 350 GPa; Poisson's ratio: 0.22). The femoral head is placed on the ring with the Ti_6Al_4Vor CoCr trunnion inserted (Young modulus: 113.8 GPa and 200GPa) through which the load is continuously applied.

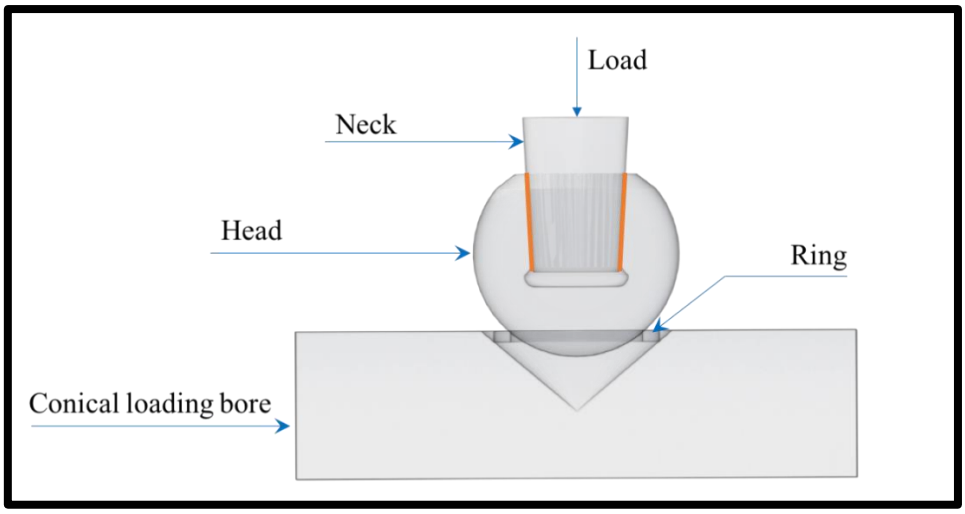

Fig.15: Scheme of the burst strength testing following the international standard ISO 7206-10.

According to the standard directives, the test involves the application of compressive or tensile stress on the head-neck system with a constant speed of 0.5 kN /s until one of the following cases is achieved:

- on the load profile discontinuities or anomalous peaks are observed;
- the femoral head is completely fractured, and cracks are present on its surface;
- the copper support ring is permanently deformed or broken;
- the established load limit has been reached.

3.RAMAN SPECTROSCOPY

Raman spectroscopy is a molecular analysis technique that can provide valuable information on the molecular composition, bonds, chemical environment, phase and crystal structure of the samples under examination, and is therefore appropriate for the analysis of materials in several forms: amorphous or crystalline solids, liquids, and gasses.

The technique exploits a physical phenomenon discovered in 1928 by the Indian physicist C.V. Raman, who won the Nobel prize in 1931. He discovered that a small fraction of the radiation scattered by specific molecules have a different energy from the incident radiation, and the energy difference is related to the chemical structure of the molecules responsible for the diffusion. This phenomenon was called the "Raman effect."

The principle on which the Raman technique is based is the diffusion of a monochromatic radiation incident on the sample. The information that can be obtained derives from the way this phenomenon occurs.

When monochromatic radiation affects the surface of an object, the radiation can be: absorbed if it has an energy equal to a possible transition to a higher energy level (ex: UV-vis, IR); reflected if it does not interact with matter; diffuse if it interacts without energy transitions.

3.1 Basic principles

When light interacts with matter, the photons which make up light can be absorbed, dispersed, or not interact with the material, passing through it. The phenomenon of absorption predicts that the energy of the incident photon coincides with the energy gap between the fundamental state of a molecule and its corresponding excited state.
Generally, many spectroscopic techniques on this phenomenon are based.
On the contrary, scattering may occur whether or not there is an adequate pair of energy levels to absorb the radiation.
Radiation is described by its wavelength ($\lambda = \frac{c}{\nu}$), while studying the interaction of the radiation with the state of the molecule it is necessary to introduce the frequency ($\nu = \frac{\Delta E}{h}$) or the wavenumber ($\varpi = \frac{\nu}{c} = \frac{1}{h}$), both linearly dependent on energy.
The interaction of radiation with materials change if we compare IR spectroscopy and Raman spectroscopy; these two techniques can be considered complementary and non-competitive. At the bottom of the two spectroscopic techniques, there are two different physical principles, in the IR, there is selective absorption of the radiations which cause energy transitions while in the Raman technique there is the anelastic diffusion of light. Moreover, the selection rules, which determine which modes of vibration are active and which are not, are different: in the IR, energies that cause changes in the dipole moment of a molecule are absorbed, while in Raman is required a change of its polarizability, property linked to the possibility of distortion of the electronic cloud.
As a result, some modes of vibration are active in the IR and not in the Raman and vice versa. To the advantage of the Raman technique, water and glass do not cause interference, differently from IR, and the lines of the Raman spectrum are generally narrower and, therefore, easier to identify. The advantage of the IR technique is that the spectra are usually more abundant in signals, and therefore the technique is easier to use.
In the Raman diffusion the light, that interacts with the molecules polarizes the cloud of electrons around the nucleus, forming a temporary state called "virtual state"; this condition is not stable, and the photon is immediately irradiated again.

Considering the light-matter interaction in terms of particles, we can imagine it as a collision between the photons and the particles that form the irradiated sample.

The photons that, interacting with the sample particles, are backscattered can be divided into two categories. If the diffusion occurs by elastic interaction, without net energy transfer, the photons (or diffuse radiation) have the same energy as the incident photons; this phenomenon is known as Rayleigh diffusion and represents the most frequent event. If the diffusion is a consequence of an inelastic interaction, with transfer of energy from the photon to a particle or vice versa, the diffuse photon has respectively smaller or higher energy than the incident one: this is the Raman diffusion or Raman effect, which occurs on a minimal number of events (figure 16).

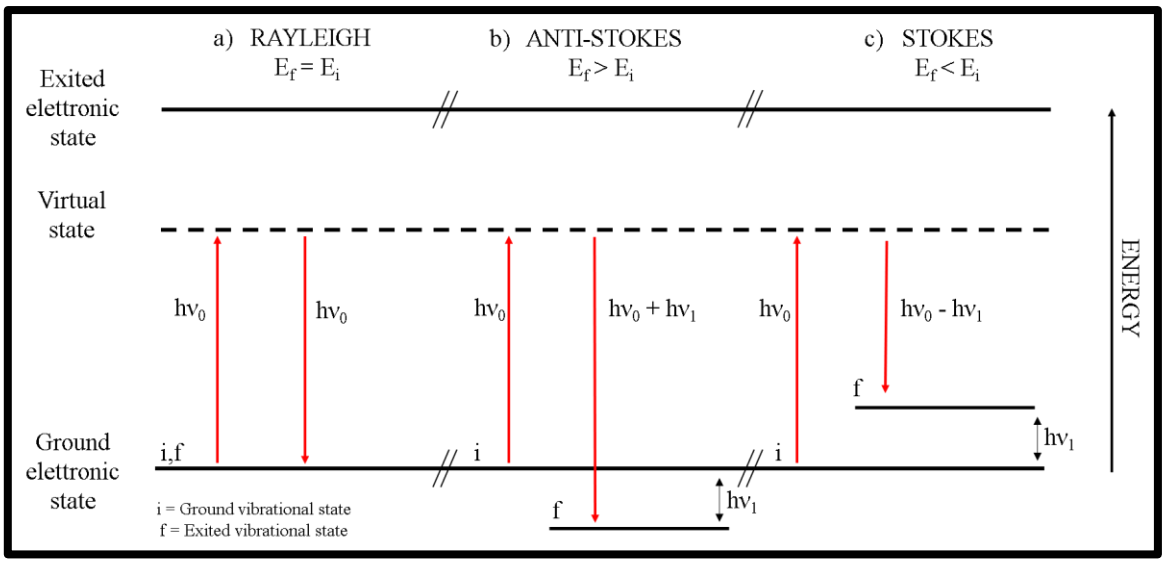

Fig.16: Energy level diagram showing the combined excitation-relaxation effect for a) Rayleigh, b) Anti-Stokes, and c) Stokes Raman scattering.

Both in the elastic interactions, which generate the Rayleigh diffusion (a) and in the inelastic interactions (b, c), we can imagine that the molecules can pass to a virtual energetic state $h\nu_0$, not quantized, from which they decay emitting photons. Inelastic interaction has two possibilities:

- the molecule already presents in a vibrational state excited $h\nu_1$ decays from the virtual state to the ground state emitting a photon with energy $h\nu_0 + h\nu_1$, higher than the incident (b);
- the molecule decays to a $h\nu_0 - h\nu_1$ excited vibrational state, emitting a photon with energy lower than the incident (c).

Three types of signals characterize the Raman spectrum of a molecule radiated by monochromatic light:

- the Rayleigh radiation, clearly the most intense of the spectrum, having the same wavelength of the incident radiation and $h\nu_0$ energy;
- the signals corresponding to the inelastic interactions in which photons are emitted with less energy than those incidents, called Stokes lines, with $h\nu_0 - h\nu_1$ energy;
- the signals corresponding to the inelastic interactions in which higher-energy photons are emitted, called Anti-Stokes lines, with $h\nu_0 + h\nu_1$ energy.

At room temperature, the fundamental vibrational level is more populated, so the Stokes lines are more intense than the anti-Stokes. Furthermore, the Stokes and anti-Stokes lines are symmetrical as compared to the Rayleigh line (both differ from $h\nu_1$ compared to Rayleigh).

3.2 Absorption and scattering

The information that the Raman spectrum of a molecule can provide us depends almost exclusively on the Stokes lines. Rayleigh radiation does not provide any information because it has the same energy in every sample; the anti-Stokes lines are generally of too low intensity to be revealed and can only be exploited to indicate the temperature of the sample based on the relationship with the intensity of the Stokes lines.

The Stokes lines, on the other hand, are linked to the functional groups of the sample molecules, and their modes of vibration, similarly to infrared spectroscopy (although with different mechanisms), and are therefore used for diagnostic purposes to identify

the compounds present in the sample qualitatively. Also, in Raman spectroscopy, the quantitative aspect is less considered since the irregularity of the analysed surface can affect the reproducibility of a measurement.

When a light wave, understood as a propagating oscillating dipole, approaches a molecule, it can interact and distort the electronic cloud around the nucleus.

From this interaction, the energy is released as diffuse radiation, but if we consider the respective dimensions of the wavelength of light (400-700nm) and the dimensions of a small molecule (example carbon tetrachloride with a size of about 0.3-0, 4nm), we see that the oscillating dipole is much larger than the molecule.

When the molecule moves, if there is the interaction between the electronic cloud and the light wave, the polarization of the electrons is observed with passage to a state with higher energy. In this instant, the energy of the light wave passes into the molecule leading to the temporary formation of a complex between the electrons of the molecule and the light energy. This complex is not stable, and light is released quickly as diffuse radiation. This condition is called the virtual state of the molecule.

From these considerations, none of the electronic states of the molecule can describe the disposition of electrons. Because following the interaction between light energy and electronic cloud, there is a different electronic geometry, with the first static molecule that has nuclei that cannot reach a new equilibrium condition. The new distorted electronic arrangement depends on the amount of energy that is transferred to the molecule and the frequency of the laser used. Depending on the laser used, the relative energy of the virtual state of the molecule, and the degree of distortion of the electronic cloud are defined. The virtual state can be defined as a real state of the transient complex formed.

The mechanism that leads to the temporary formation of the virtual state is different compared to a classic phenomenon of absorption.

The first difference is found in the fact that the additional energy is not capable of promoting an electron to an excited state of the molecule, but all states are involved in forming a "distorted" complex. A second difference is the duration of the excited state, which is much lower than most absorption phenomena. It is observed that the radiation is dispersed and not dissipated due to the transfer of energy inside the molecule.

Finally, it is possible to study particular vibrations of the interaction between the polarization of the exciting photons and the dispersed photons.

Two scattering mechanisms have been identified: Rayleigh scattering and Raman scattering. The first is the most intense form of dispersion and is realized when the electronic cloud relaxes without any nuclear movement; it is classified as an elastic process without quantifiable energy variations. Raman scattering, on the other hand, is observed less frequently, involving several scattered photons ranging from 10^6-10^8, when light interacts with electrons, with the consequent movement of the respective nuclei.

The nuclei are more substantial than the electrons, and this involves a change in energy terms, with lower or higher energy values depending on whether the process starts with a molecule in the ground state (stokes scattering), or that a molecule is formed in the vibration state excited (anti-stokes scattering). [79]

The reciprocal relationship between the intensities of the scattering of stokes and anti-stokes will depend on the number of molecules present in the fundamental vibrational state and on the number of molecules present in the excited vibrational levels. This ratio can be calculated from the Boltzmann equation proposed in Figure 17.

$$\frac{N_f}{N_i} = \frac{g_f}{g_i} e^{-[\frac{E_f - E_i}{kT}]}$$

Fig.17: Boltzmann equation.

In the upper equation "N_f" is the number of molecules in the excited vibrational energy level (f); "N_i" is the number of molecules in the ground vibrational energy level (i); "g" is the degeneracy of the levels "f" and "i"; "$E_f - E_i$" is the difference in energy between the vibrational energy level; "k" is Boltzmann's constant ($1.3807x10^{-23}JK^{-1}$).

3.3 States of a system

The molecules are characterized by different electronic states, each of which has a high number of rotational and vibrational states. Figure 18 shows a typical fundamental electronic state of a molecule with the internuclear separation and the energy of the system, respectively, along the abscissa and ordinate axis; the curved line depicts the electronic state.

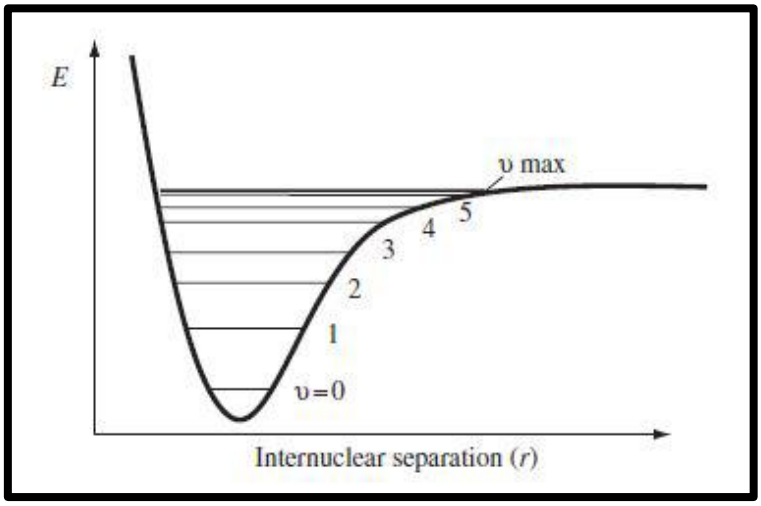

Fig.18: Morse curve in which the electronic state shows the vibrational levels as horizontal tie lines.

As is observed graphically at long distances, internuclear atoms are free to move while reducing the distance the forces of attraction push them towards the formation of the bond. When the distance is minimal, repulsive forces prevail with a sudden increase in the energy of the molecule.

Consequently, the lower energy coincides with the length of the bond.

Not all the energy states shown in Figure 18 are possible; this is because it is necessary to consider the vibrations of the molecules that lead to quantized vibrational energies. A certain vibrational level in a precise electronic state is called the vibronic level.

In the Morse curve shown in Figure 18, not all vibrations are taken into consideration but merely a single vibration. The "v = 0" level represents the fundamental state of the

molecule in the absence of vibrations; the next level involves the absorption of a quantum of energy with vibration of the molecule. The energy required in the levels above the "v = 1" will be different from that required to promote the molecules from the ground state to the first of excitation.

If we observe energy changes different from the energy quantum, we obtain a peak called “overtone”; in the Raman scattering, this phenomenon is observed in rare cases.

Very similar to overtones are the combination bands that lead to the formation of a new level following the mutual interaction between two quanta of different vibrations.

At lower energy values, compared to the vibrational levels, the rotation levels must also be considered. Figure 18 shows the Morse curve of the fundamental state of a molecule, in the case in which the phenomenon of absorption occurs with the passage of the electron in the excited state, it is necessary to introduce a second Morse curve for the excited state placed at higher energy values along the y-axis.

Generally, in Raman spectroscopy, scattering is very fast when compared with nuclear movement; consequently, no change in nuclear separation is observed, and therefore no variation along the x-axis. For simplicity, therefore, energy changes in the molecule are represented as vertical lines, states as horizontal lines, while all other features of the curve are neglected.

In Figure 16 reported in the previous paragraph, it is reported that the energetic changes, which occur following the interaction between the molecule and light radiation, lead to the formation of a virtual state, with subsequent scattering when the molecule relaxes.

The diffuse radiation is expressed as Raman scattering, with the energy difference between the excitation and scattering process that coincides with the vibrational energy of the molecule.

Together with these considerations, it is possible, by studying the shape of the Morse curve, to calculate the energy of the vibronic levels using a simple harmonic approximation. In this approximation, the Morse curve, intended as a parabola, is devised starting from a diatomic molecule where the two masses are held together by a vibrating spring.

The relationship between the frequency, the mass of the atoms of the diatomic molecule, and the bond strength are expressed by Hooke's law (Figure 19).

$$\nu = \frac{1}{2\pi c}\sqrt{\frac{K}{\mu}} \qquad \mu = \frac{M_X M_Y}{M_X + M_Y}$$

Fig.19: Hooke's law "ν" on the left and reduced mass "μ" on the right.

"K" is the force constant of the bond between the two molecules "X" and "Y," "c" is the velocity of light, "μ" is the reduced mass of the atom "X" and "Y" of masses "M_X" and "M_Y."

3.4 Polarization and Raman intensity

When a source emits light radiation, each emitted photon is characterized by an oscillating dipole, and if observed at 90 degrees respect to the direction of propagation, the beam of light rays looks like a wave. Generally, the lasers used in Raman scattering are partially polarized and consist of an optical polarizing element, which ensures that the polarization occurs linearly.

If the linearly polarized light beam passes through a molecule, the electronic cloud is polarized according to a value that varies according to the ability of the electrons to polarize (ALFA = polarizability). Following the interaction between polarized light and molecule, there is a dipole change in the molecule along the three Cartesian coordinates "x," "y" and "z," so to clarify the effect of the interaction between linear polarized radiation and molecule it is necessary to follow the expression ($\mu = \alpha E$) where the dipole "μ" depends on the product between the field of the incident photon "E" and the polarizability "α."

Usually, the polarizability components are labeled with a first subscript indicating the polarizability direction and the second subscript representing the polarization of the incident radiation, operating along with the three directions "μ_x," "μ_y" and "μ_z" (for example $\mu_x = \alpha_{xx}E_x + \alpha_{xy}E_y + \alpha_{xz}E_z$).

In figure 20 is defined as the polarizability in terms of the tensor:

$$\begin{bmatrix} \mu_x \\ \mu_y \\ \mu_z \end{bmatrix} = \begin{bmatrix} \alpha_{xx} & \alpha_{xy} & \alpha_{xz} \\ \alpha_{yx} & \alpha_{yy} & \alpha_{yx} \\ \alpha_{zx} & \alpha_{zy} & \alpha_{zz} \end{bmatrix} \begin{bmatrix} E_X \\ E_Y \\ E_Z \end{bmatrix}$$

Fig.20: Tensor representing the polarizability of the molecule.

As can be seen from the complex arrangement shown in the tensor of Figure 20, there is a clear correlation in Raman scattering between the incident beam and dispersed beam.

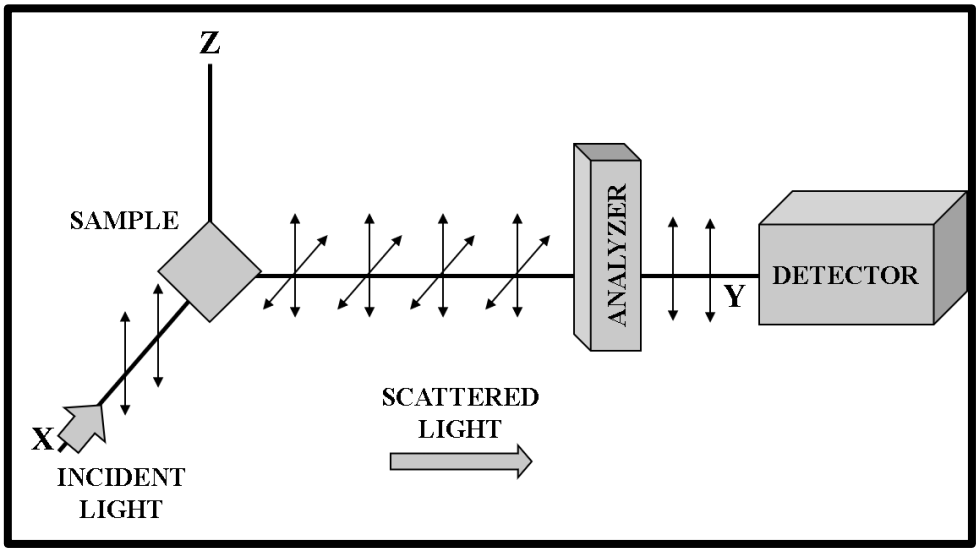

Fig.21: System to study the polarization of Raman scattering, the black arrows depict the plane of diffused light; by rotating the Analyser, it is possible to measure parallel or perpendicular scattering.

The Raman spectrometer is made up of a series of optical elements, such as the polarizer, which allow calibrating the polarization of the incident ray, in this way the light beam along the plane is polarized, and at the same time allow to determine the angle of the plane of the incident ray.

A further optical element is an analyser, which analyses in detail the polarizability of the scattered ray through a particular system that grants polarized light to pass through a detector; it is usually positioned at 90 degrees allowing any polarized radiation, that has interacted with the molecule, to reach the detector. The arrangement of the various components is shown in figure 21.

In a crystalline material, the optical axes are arranged 90 degrees of respect to each other, recognizing that light is a property of the dipole. For example, in the tetragonal space group, the optical axis and the crystalline axis are arranged together, forming a right angle, to be aligned with the polarization direction of the incident ray.

In this way, the polarized light can cross the crystal along the “z” axis identifying the “α_{zz}” component. In the presence of other space groups and more generally, in most cases, the analysis is much more complicated; if the light is not aligned along a precise axis of the crystal, it will rotate inside it. This approach is considered in an informative context for a limited number of solid-state samples, whereas for gaseous or liquid samples, the procedure is different. In a solution or gas state, there is no precise direction of the molecule's axes respect to the direction of polarization of the light, but it is still possible to obtain information from polarization measurements.

Usually, what is reported by the analysis is the depolarization ratio of the diffuse radiation, where the intensity of a peak is measured as a function of the polarization plane of the incident parallel or perpendicular light.

Generally, the average polarizability is regulated by two separately measurable quantities, isotropic scattering, and anisotropic scattering; the first is measured with the analyzer parallel to the plane of the incident radiation while the second with the analyzer at 90 degrees compared to the plane.

The new tensor is calculated, starting from the relationship between parallel and perpendicular scattering, precisely called depolarization ratio "ρ."

Below in figure 22 are shown the relative formulas that allow calculating the depolarization ratio, with "$\overline{\alpha}^2$" and "γ^2" representing the isotropic and anisotropic part

of the tensor, "$\bar{\alpha}\,\|^2$" and "$\bar{\alpha}\,\perp^2$" are the effects of parallel and perpendicular polarization, and finally, "ρ" represents the relationship between parallel and perpendicular scattering.

$$\bar{\alpha}^2 = \frac{1}{3}(\alpha_{xx} + \alpha_{yy} + \alpha_{ZZ})$$

$$\gamma^2 = [(\alpha_{xx} - \alpha_{yy})^2 + (\alpha_{yy} - \alpha_{zz})^2 + (\alpha_{zz} - \alpha_{xx})^2 + 6(\alpha^2{}_{xy} + \alpha^2{}_{xz} + \alpha^2{}_{yz})]$$

$$\bar{\alpha}_{\|}{}^2 = \frac{1}{45}(45\bar{\alpha}^2 + 4\gamma^2) \qquad \bar{\alpha}_{\perp}{}^2 = \frac{1}{15}\gamma^2$$

$$\rho = \frac{\bar{\alpha}_{\perp}{}^2}{\bar{\alpha}_{\|}{}^2} = \frac{3\gamma^2}{45\bar{\alpha}^2 + 4\gamma^2}$$

Fig.22: Equation representing the isotropic and anisotropic part of the tensor, the parallel and perpendicular polarization, and the depolarization ratio.

The depolarization ratio of a molecule with moderate symmetry both in the gaseous and liquid phase changes according to the degree of symmetry of the vibration; usually for low depolarization values correspond vibrations with a high degree of symmetry.

A direct consequence is that the measurement of the "$\bar{\alpha}\,\|^2$" parallel scattering or of the "$\bar{\alpha}\,\perp^2$" perpendicular scattering through the analyzer allows to control the assignments of the peaks; for example, this control is impossible to perform in the case of infrared spectroscopy.

If a monochromator is used to detect the analyser radiation, the efficiency of the light separation degree depends on the polarization plane; consequently, for parallel polarization, there will be a more efficient signal than perpendicular polarization; with a theoretically incorrect polarization ratio. One way to overcome this problem is to use a "scrambler," which confuses the polarization of the light before it crosses the monochromator, so the detector is efficient in all polarization directions.

There is a rule that can combine the different components of polarization, propagation, incident radiation angle, and diffuse radiation angle, into a single value linked to the intensity of Raman radiation. The degree of the polarizability of the molecule, the intensity of the source and the scattering cross-section also influence the final intensity

of Raman radiation. Below in Figure 23 is shown the law to calculate the final intensity of the Raman radiation "I."

$$I = Kl\sigma^2\omega^2$$

Fig.23: Intensity of Raman scattering.

The "K" parameter represents the speed of light, "l" the laser power, "ω" the frequency of the incident radiation, and "σ" the polarizability of the electrons of the molecule. The incident light frequency and laser power can be experimentally controlled.[80]

3.5 Confocal mode

During the analysis of a solid or liquid sample, the properties of a laser such as the depth of penetration or the shape depend on the refractive index and the absorption capacity of the analysed sample.

In this way, Raman scattering within the probe volume will be observed, with intensity measurements along the length of the beam and the focal plane.

A direct consequence will be that the Raman spectrum will report not only information on the surface crystallographic plane but also information deriving from a set of crystallographic planes below the surface. The use of the Raman spectrometer in confocal mode is regulated thanks to some cross-slit that directly modulates the ray probe; in this way, regions placed outside the fire are excluded. [81]

As can be seen in figure 24A, in the Raman spectrometer there are two filtering pinholes, one located on the focal plane of the microscope and one positioned on the exit path of the laser beam; the first slot serves to improve both lateral and axial spatial resolution, while the second improves the Gaussian shape of the laser probe. In this way, it is possible to exclude the light coming from the regions out of focus.

Usually, the out-of-focus light coming from the area below the surface is brought to a focus before opening and, therefore, not considered, while the surface signal is focused during the opening of the slit and then recorded.

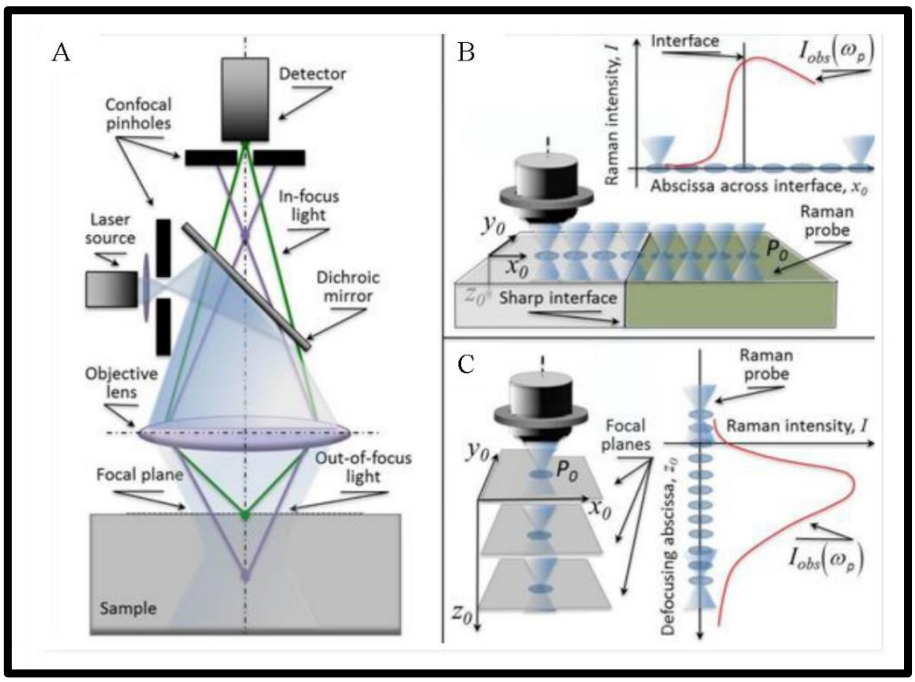

Fig.24: A) Schematic representation of the Raman spectrometer in a confocal configuration.
B), C) Schematic PRF calibrations of the probe along the plane $G_{ip}(x, y, x_0, y_0)$ and in-depth $G_{ip}(z, z_0)$.

A problem to consider is the presence of a quantitative deconvolution of Raman spectra between a set of given focal planes, associated with a specific geometry of the laser probe when it interacts with the sample to be analysed. Consequently, it is necessary to introduce a control function "Probe Response Function" (PRF), which changes experimentally from sample to sample.

The PRF function, linked to certain geometric factors, changes according to the chemical-physical properties of the sample and consists of two main elements shown in Figure 24B-C, respectively. Two pertinent aspects are observed: the first refers to the action of the probe in the plane $G_{ip}(x, y, x_0, y_0)$, and the second refers to the depth action of the probe $G_{ip}(z, z_0)$.

In the first case, through a movement along "x_0", it is possible to calculate the Raman intensity as a function of the lateral resolution, while in the second case, working along

the axis perpendicular to the plane of the sample "z_0" it is possible to perform analyses in-depth defocusing the probe. The result of the Raman spectrum intensity will depend directly on the PRF function.

There is a relation shown in figure 25 that allows calculating the value of the PRF considering the convolution of the response following the action of the probe in-depth and along the plane, when the laser is focused in a precise position of the plane P_0 (x_0, y_0, z_0).

$$G_{ip}(x,y,x_0,y_0,z_0) \propto G_{ip}(x,y,x_0,y_0)\ x\ G_{ip}(z,z_0) =$$

$$= \exp\left[(-2)\frac{(x-x_0)^2+(y-y_0)^2}{R^2}\right]\frac{p^2}{(z-z_0)^2+p^2}\exp(-2\alpha z)$$

Fig.25: Probe Response Function of the laser in a given position of the plane P_0 (x_0, y_0, z_0).

"R" is the radius of the laser beam in the focal plane, "p" the response parameter of the probe that tends to infinite values for non-focused beam, "α" is the absorption coefficient of the material at precise incident wavelength. [82] [83]

4. THESIS PLAN

In this work, the effects of hydrothermal ageing were studied on BIOLOX® delta femoral heads subjected to burst strength test, first through a fractographic approach and then by Raman spectroscopy.

The femoral heads were divided into three groups, two of whom were hydrothermally degraded to simulate in vivo degradation; successively, the breaking test was performed according to ISO 7602-10 standards.

The main objectives of this work are the detailed reconstruction of the fracture dynamics of the femoral heads subjected to the burst strength test, study how the mechanical properties of the ZTA femoral heads have changed and how much the low-temperature degradation may have influenced, for example, the flexural strength or fracture toughness.

The first thing studied was the mechanics of the fracture, the surfaces involved and cracks origin. Successively, thanks to Raman spectroscopy, it was possible to study how the residual stresses are directly linked to hydrothermal degradation.

Overall, an optical analysis was conducted for the study of fracture surfaces, revealing how the same morphological structures are present in all samples.

The study was based on two approaches: a fractographic approach, where optical studies are combined with simple mathematical analysis techniques, such as the linear regression method; a second more rigorous and precise approach, where it was possible to calculate the stresses involved thanks to the measurements taken with the Raman spectrometer. [84]

5. MATERIALS AND METHODS

5.1 Samples

In this study were considered Eighteen BIOLOX®delta ceramic femoral heads (CeramTec, Plochigen, Germany), all the samples have a diameter of 28 mm, all L type, and generically acquired by the market with the production year 2015.
The ceramic material of the Biolox® delta provides according to the patent an alumina matrix (Al_2O_3), containing 17% zirconia (ZrO_2) stabilized by a 1.3-1.4mol% yttrium oxide (Y_2O_3), 3% strontium oxide ($SrAl_2O_4$) and a 0.6% chromium oxide (Cr_2O_3) responsible for the pink colour of the femoral heads. [84]

5.2 Hydrothermal ageing

One of the techniques for simulating the in vivo degradation of ZTA ceramic femoral heads is the hydrothermal degradation carried out in an autoclave, based on the model proposed by Mehl-Avrami-Johnson. According to the simulation, every hour spent in an autoclave at a temperature between 132-134 °C and a pressure of 2.0 bar, it is equivalent to an exposure of about 3-4 years in vivo. [85]
Recognizing that the ZTA ceramic material subjected to thermal degradation, suffers a polymorphic change, from tetragonal zirconia to monoclinic zirconia, the makers have carried out numerous studies in vitro ensuring that to simulate in vivo degradation, in vitro simulations are necessary for a value of hundreds of years. [86]
Based on these considerations, the hydrothermal ageing was performed in an autoclave at a temperature of 132 °C under 2.0 bar pressure.

The samples were divided into three groups according to the following order:

• Six Pristine samples not subjected to thermal degradation in an autoclave;

• Six autoclaved samples, hydrothermally aged for 150 hours;

• Six autoclaved samples, hydrothermally aged for 165 hours.

5.3 Burst strength testing

The burst strength test was performed following the international standard ISO 7206-10 protocol, as described in paragraph 2.3.

The breaking load was applied through the stem neck by continually increasing the load at a rate of 0.5 kN / s until material fracture. For the correct development of the breaking test, all the different components, the trunnion (neck), femoral head, copper ring, and conical loading bore (with Brinell hardness between 150-250 HB), were aligned perpendicularly (Figure 26).

According to the standard regulations, the trunnion (neck) used and inserted in the artificial femoral head can be formed either by a CoCr alloy or a Ti_6Al_4V alloy.

In our work, a CoCr trunnion was used.

Following the division of samples shown in the thermal degradation treatment, the artificial femoral heads were divided into pristine, moderately loaded, and severely loaded. Pristine femoral heads were normally subjected to breaking tests, while moderately and severely loaded femoral heads were repetitively loaded and unloaded.

Precisely for moderately loaded heads, a loading-unloading cycle was performed with values between 3kN and 1kN for a total of 15 hours in autoclave at 132 °C, while similarly for the severely loaded femoral heads the loading-unloading cycle was performed with values between 20kN and 10kN for a total of 16.5 hours in autoclave at 132 °C. Both cycles of load-unload and autoclave ageing were repeated ten times for a total of 150 hours and 165 hours.

The loading-unloading test was performed under vacuum conditions, and the final load cycle was performed in the presence of 0.5ml of phosphate-buffered saline solution in the taper bore to enhance the action of the last load cycle.

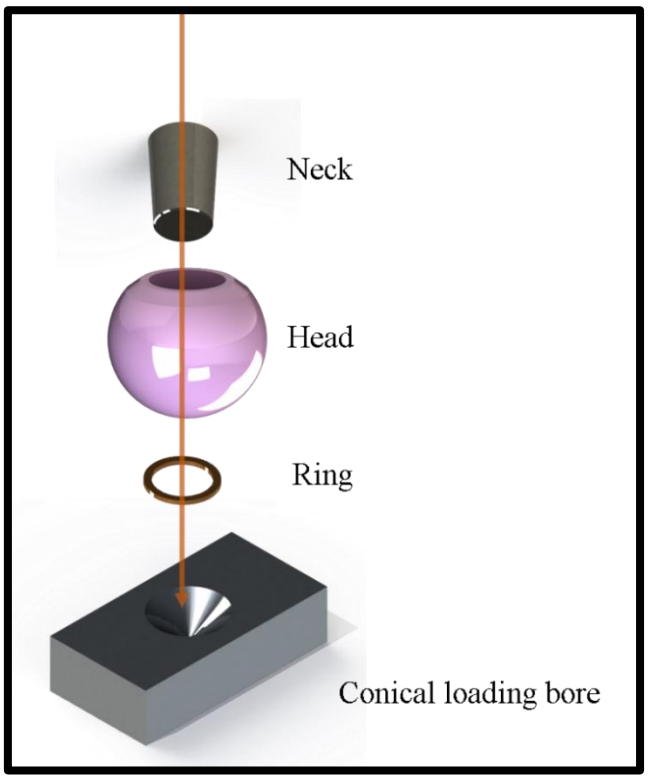

Fig.26: Scheme of the burst strength testing following the protocol ISO 7206-10.

5.4 Sample characterizations

5.4.1 Laser microscopy

The morphological analysis of the femoral heads was mostly studied using the 3D laser-scanning microscope (VKX200K series, Keyence, Osaka, Japan) shown in figure 27. This laser microscope is equipped with the best confocal laser technology that allows obtaining images with a considerable depth of field, in focus across the entire screen, detecting all the finest details of the samples. This laser microscope uses an optical system that ensures that no light other than that passing through the focal point reaches the photoreceptor (image formed by the light reflected from the sample), in this way the photoreceptor is reached by the maximum amount of light possible and is possible to record all the information related to focal point changes (sample height).

Fig.27: 3D laser-scanning microscope, VKX200K series, Keyence.

In this study, the micrographs were taken with variable magnifications ranging from 10x to 150x, with a numerical aperture between 0.30 to 0.95. The VKX200K series laser combines this confocal optical laser with an X-Y scanner that moves at high speed to create high-resolution images and gather information about the roughness, height, and shape of the sample.

5.4.2 Scanning electron microscopy

A field-emission-gun scanning electron microscope (JSM 7001F SEM, JEOL, Tokyo, Japan) was used to study the morphology of the fracture surfaces of the artificial femoral heads. All the samples were previously sputter-coated (Cressington, Watford, UK) with a platinum layer with a thickness of about 20-30 Å; while all the images collected were obtained with an acceleration voltage of 10 kV with magnifications between 100x and 50000x.

5.4.3 Raman spectroscopy

Generally, a Raman spectrometer consists of five fundamental components: a monochromatic light source (to promote Raman scattering), a microscopic device to focus the incident ray, a spectrograph that split the light into a spectrum of frequency, a detector that transforms the light signal in an electrical signal and finally a software that allows to display the spectrum of frequency.

In this work, all spectroscopic analyses were collected at room temperature using a triple monochromator (T-64000, Horiba / Jobin-Yvon., Kyoto, Japan) equipped with a charge-coupled device detector (CCD-3500V, Horiba Ltd., Kyoto, Japan) with 1024x256 pixels, arranged along the image output plane and cooled by liquid nitrogen down to 140K

The excitation source was at 532nm Nd: YVO_4 diode-pumped solid-state laser working with a nominal power at 200mW (SOC JUNO, Showa Optronics Co.Ltd., Tokyo,

Japan). The collected frequency spectra were processed with commercially available software (LabSpec, Horiba / Jobin-Yvon., Kyoto, Japan).

Each morphological analysis of the fracture surfaces of the femoral heads subjected to a burst strength test was conducted using square maps, each consisting of several points along with the X-Y directions. The lateral resolution of the Raman microprobe was on the order of 1 μm. All the maps were then unified in order to obtain broader information profiles to produce macroscopic maps of the sample surface.

Finally, using the confocal mode of the Raman spectrometer, in-depth analyses were collected using square maps from -100 μm to +100 μm along the X and Y axes, at specific depths of 5 μm, 10 μm, 20 μm, 50 μm, and 100 μm.

6. RESULTS AND DISCUSSION

6.1 Burst strength test results

The eighteen artificial femoral heads in ZTA ceramic material were subjected to the burst strength test according to the methods expressed in paragraph 5.3, maintaining the same division of the samples already announced:

- pristine femoral heads;
- moderately loaded and hydrothermally aged femoral heads for 150 hours in an autoclave at 132°C under 2.0 bar pressure;
- severely loaded and hydrothermally aged femoral heads for 165 hours in an autoclave at 132°C under 2.0 bar pressure.

All the samples have exceeded the minimum average burst-test standard of >42kN according to US FDA regulations, using CoCr trunnions as required by the ISO 7206-10 standard. CoCr trunnion has a higher elastic modulus than the Ti_6Al_4V, with consequent smaller contact area between the trunnion and femoral head under stress. [87] In literature, it is reported that in the presence of materials with higher rigidity, the amount of fretting is reduced on surfaces with comparable morphologies. [88]

In the graph shown in Figure 28 is proposed the division of the samples in each category; using the Student t-test and a p-value of 0.05 for significance, the difference between the pristine femoral heads and the moderate loaded and hydrothermally aged heads has no statistical significance ($p = 0.42$), while the difference in load values, recorded between the pristine heads and the severely loaded and hydrothermally aged heads, was just beyond the threshold of statistical significance ($p = 0.053$).

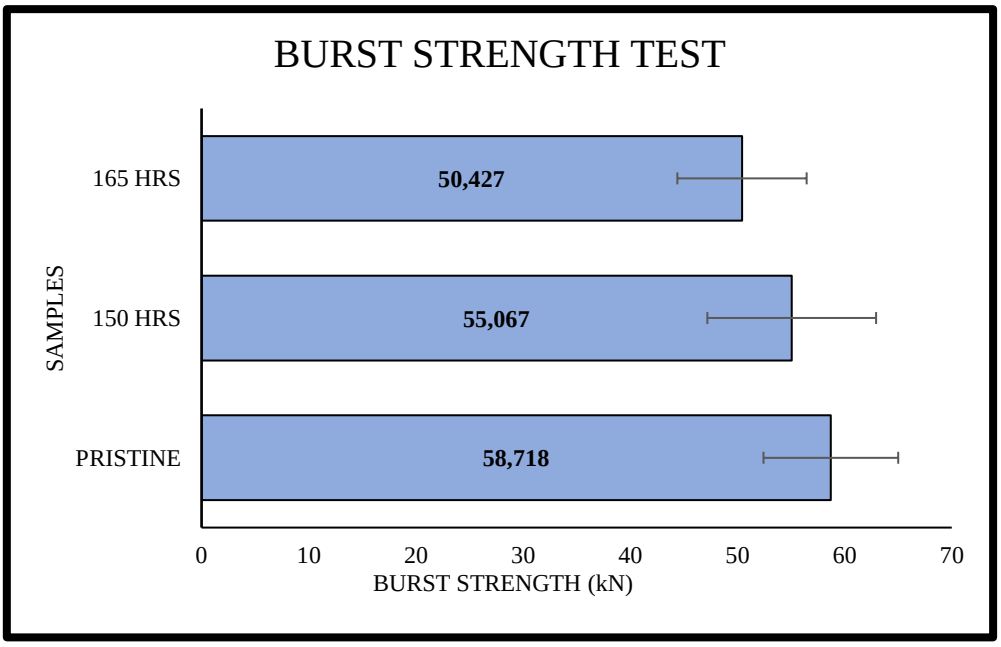

Fig.28: Burst strength test results.

The burst strength test values reported for the pristine femoral heads differ from the values published in some studies present in the literature, for example, from the analyses provided by the producers (CeramTec), the average value of the burst-test is about 83kN.[86] Further studies showed that for hydrothermally aged femoral heads for 50 hours in an autoclave, burst-test values were reported close to 80kN. [89]

However, in the first example, there is no information on the type of trunnion used for the burst strength test, whether Ti_6Al_4V or CoCr, while in the second example reported, there are no indications on the geometry of the femoral heads. [90] The different choice in the material of the trunnion influences the final burst-test value, in fact with the CoCr trunnion, with higher elastic modulus, there will be a small contact area between the trunnion and the femoral head with consequent lower fracture resistance value; while with Ti_6Al_4V trunnions, the contact area is more extensive and therefore the value reported in burst strength tests will be higher. [87]

Finally, studies carried out on pristine artificial femoral heads of the same diameter (28mm) revealed values higher than those obtained in this work (figure 28) of about 10%.[91] These differences may be justified by stress intensification at the taper interface; usually, for short-neck heads, the stress is distributed on a wider surface and in a more homogeneous way, while for long-neck heads the stress is not homogeneous and the transfer occurs lower in the taper in an area that is weaker, making the material weaker and less fracture resistant. [92]

6.2 Fractographic femoral heads reconstruction

The reconstruction of the femoral heads subjected to a burst strength test is fundamental to understand the dynamics of the fracture and the surfaces of the heads involved. Figure 29 shows only six of the eighteen femoral heads analysed, two for each category considered.

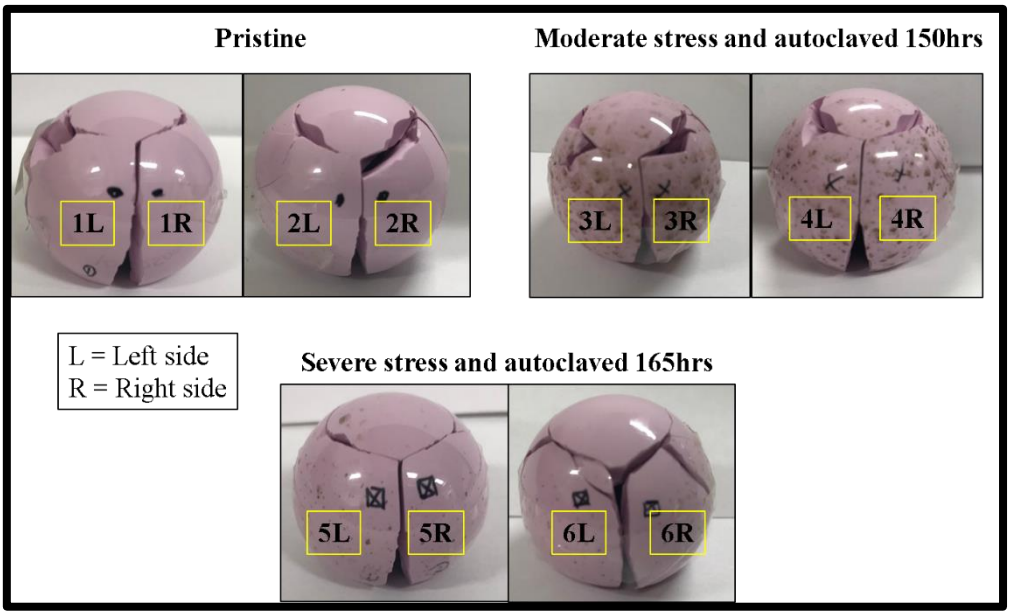

Fig.29: Reconstruction of representative burst strength tested femoral heads.

In all femoral heads, both pristine and hydrothermally aged, the same fracture morphology was observed:

- a circular fragment on the upper part of the head;
- a few large, longitudinal side fragments (number varying from four to nine fragments) which constitute the central body of the femoral head;
- a variable number of small-sized fragments with different morphology, classified as (i) spike-like (where one of the dimensions was one order of magnitude larger than the other two), (ii) blade-like (with a surface area higher than 1 cm 2 but thickness below 0.5 mm), and (iii) polyhedron like (<3 mm in maximum dimension).

The fragmentation process is based on simple principles: there is a perfectly oriented fracture plane parallel to the axis of the femoral head, while the fracture planes that follow both sides are more or less inclined respect to the axis of the head.

Generally, the parallel fracture plane is called the primary plane and is the one where the fracture occurs first when the femoral head breaks. In the instant that precedes the total fracture of the head, there is a symmetrical hoop stress field on the head with the critical stresses around the conical bore. The primary fracture modifies the distribution of stress within the femoral head with consequent formation of secondary fragments with shape and fracture surfaces very different from the primary fragments. [76]

Based on these considerations, the fragments of the femoral heads were divided into primary fragments and secondary fragments, as shown in figure 30.

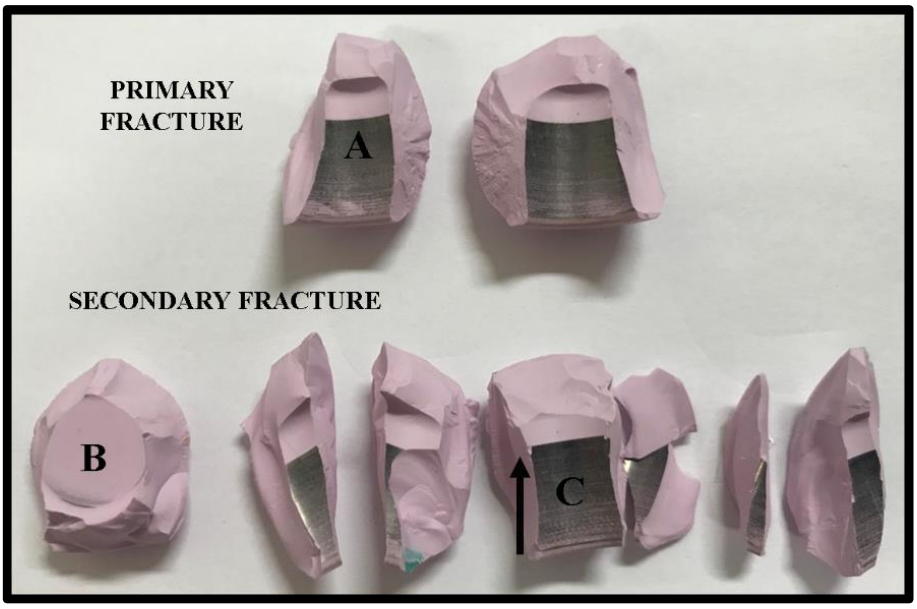

Fig.30: Main fragments of burst strength tested femoral heads, evidencing primary and secondary fracture surfaces.

From the fragment analysis, there was a first symmetrical fracture plane parallel to the load application axis, which automatically defines the primary fragments and the secondary fragments with completely random shapes.

A second observation is a metallic contamination that is visible through the metallic stains in the inner part of the fragments (cf. location labeled A in figure 30).

These stains cover most of the internal cylindrical cavity of the femoral head, and the total absence of stains in the inner part of the fragment relative to the upper part of the head indicates that the CoCr trunnion never reaches the final part of the cavity during the test (cf. location labeled B in figure 30).

Finally, it is believed that the trunnion increases its contact force as it proceeds towards the inside of the cavity; following the black arrow in figure 30 (cf. location labeled C in figure 30), a colour gradient is observed, which intensifies as the trunnion penetrates inside the cavity. The presence of a colour gradient is linked to the increase in metal contamination.

6.3 Surface fracture morphology

Thanks to optical microscopy, it was possible to study all the elements that characterize a fracture surface of the primary fragments, as already explained previously in paragraph 2.2.1. From the study of the primary fragments it was possible to identify the "fracture mirror," a smooth region surrounded by cracks with radial direction at the point of fracture; the "mist region," an intermediate region between the smooth surface of the mirror fracture and cracks that propagate radially in "hackle area"; the "hackle area," a region where the cracks propagate very quickly; the "twist hackle," cracks formed as a result of torsion from the original fracture plane and formed at long distances from the mirror fracture. All the elements represented in figure 31 were observed in all the symmetrical primary fragments (side L and side R shown in figure 29) of the eighteen femoral heads subjected to burst strength test.

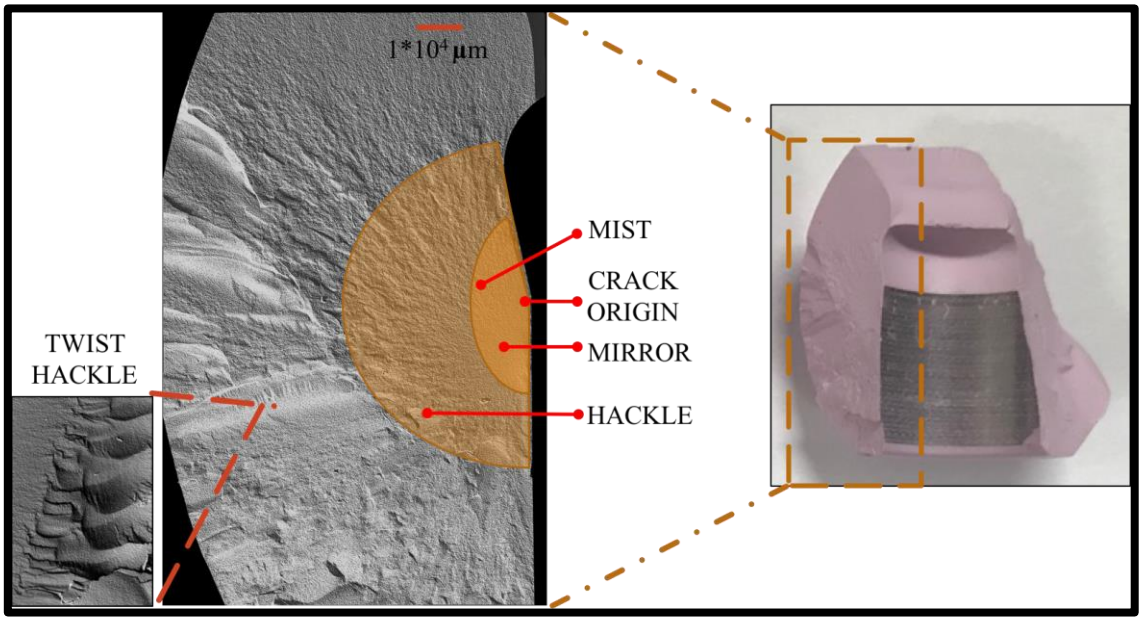

Fig.31: Schematic representation of the surface elements that make up the primary fragments.

By studying the different fracture surfaces of the primary fragments, it was possible to identify two main morphological regions, each different in position and mechanical behavior during the burst strength test.

The first region identified near the crack origin of the fracture mirror is characterized by a mainly transgranular morphological structure and usually provides essential information about residual stresses and how these are distributed along the fracture surface. The second region identified mainly along the "Hackle area" is characterized by numerous areas with intergranular morphology, at distances greater than 1.5mm from the crack origin.

The transgranular or also called cleavage fracture occurs when the fracture follows preferential directions of the crystal, ignoring the individual grains of which the material is composed; usually, the fracture surface appears bright and reflective. The intergranular fracture is instead a fracture that follows the grain boundaries; in this way, the wavefront of the crack passes from one grain to the other following propagation lines perpendicular to the front of the crack. These cracks bind together, forming the fracture surface.[76]

These two different modalities in the fracture of the primary surfaces induce to think about which is the mechanism of global propagation of the breach; consequently, it can be assumed that initially in the fracture mirror there is a lower absorption of energy (typical of cleavage fractures), but this energy is sufficient to break the chemical bonds of the material thus causing the propagation of the crack through the grains themselves or the crystals of ceramic material. From the energy point of view, it is necessary to satisfy the balance between energy released and energy absorbed, consequently as the cracks grow and propagate in the "hackle area" the energy is transferred to the material leading to the global weakening of the grain edges with inevitable propagation of cracks along them and final breakage of the material.

Following in Figure 32 are reported the two transgranular and intergranular fractures obtained from the SEM analyses (JSM 7001F SEM, JEOL, Tokyo, Japan) obtained at 10000 magnifications.

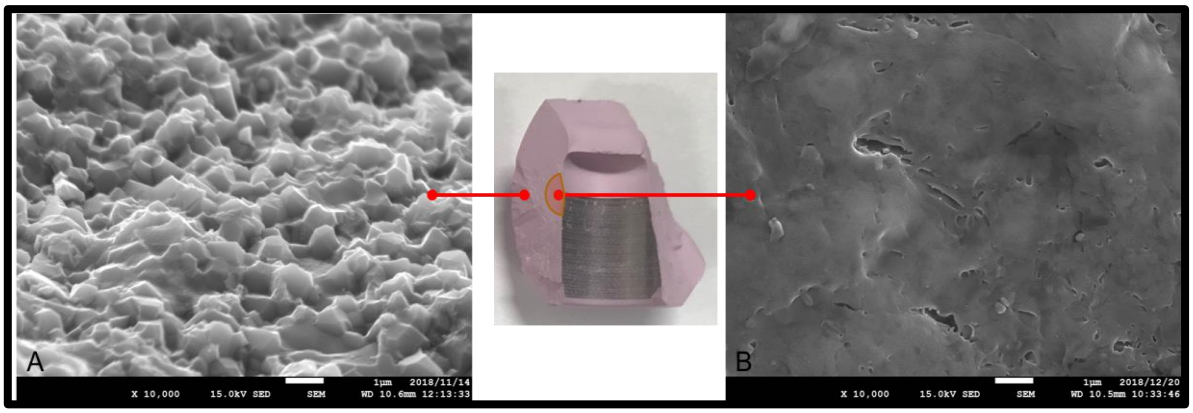

Fig.32: Scanning Electron Microscope images of two areas of the main fracture surface: A) intergranular area and B) transgranular area.

From the study of all the primary surfaces of all the samples subjected to burst strength test, it was observed that the crack origin of the fracture is the same, except for some cases in which an incorrect alignment between stem and femoral head occurred during burst strength test, or there was a defect in the ceramic material. The initial fracture starts from the contact area between the endpoint of the taper (knurling inside the femoral head), and the metallic neck-stem. The crack origin is circled in red in figure 33. During the burst strength test, the breaking load is applied perpendicularly to the plane on which the femoral head is placed (paragraph 5.3), but simultaneously with the thrust of the trunnion, it is also necessary to consider the two thrusts coming from the contact surface between the copper ring and the femoral head. These compressive thrusts mainly affect the breaking mechanism, with the point of maximum compression, which coincides with the point of maximum torsion stress, thus leading to the formation of the fracture mirror. On the surfaces of the primary fragments, the morphology of the surfaces is the same in all the femoral heads with an area rich in cracks on the upper part of the mirror, and an area devoid of irregular cracks but more brilliant and shinier under the mirror plane.
It has been observed that in some femoral heads, the point of origin of the fracture does not coincide with the point of maximum stress, but the break is identified in different regions, always along the section of contact between the taper and the stem (figure 34). In these cases, no dependence of these phenomena was observed with the initially applied load, or with hydrothermal ageing.

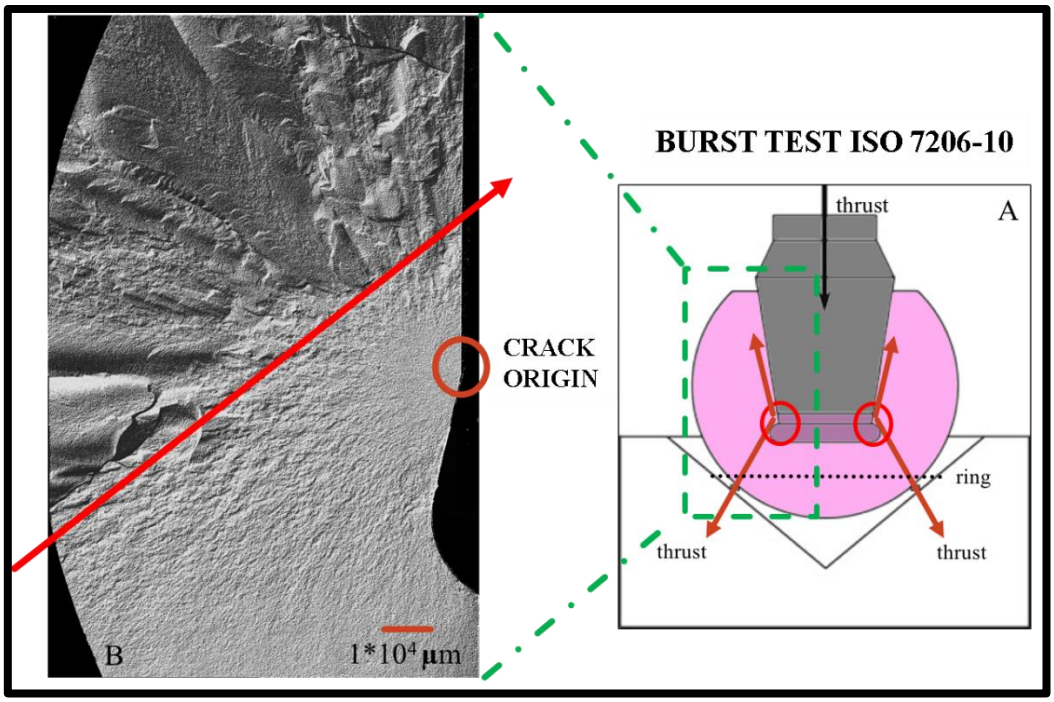

Fig.33: A) Representation of the burst strength test with, indicated in red, the cracks origin and the relative radial propagation; B) clear representation of the morphology of the primary fragment with an area rich in cracks on the upper plane of the mirror and shiny and bright on the mirror plane.

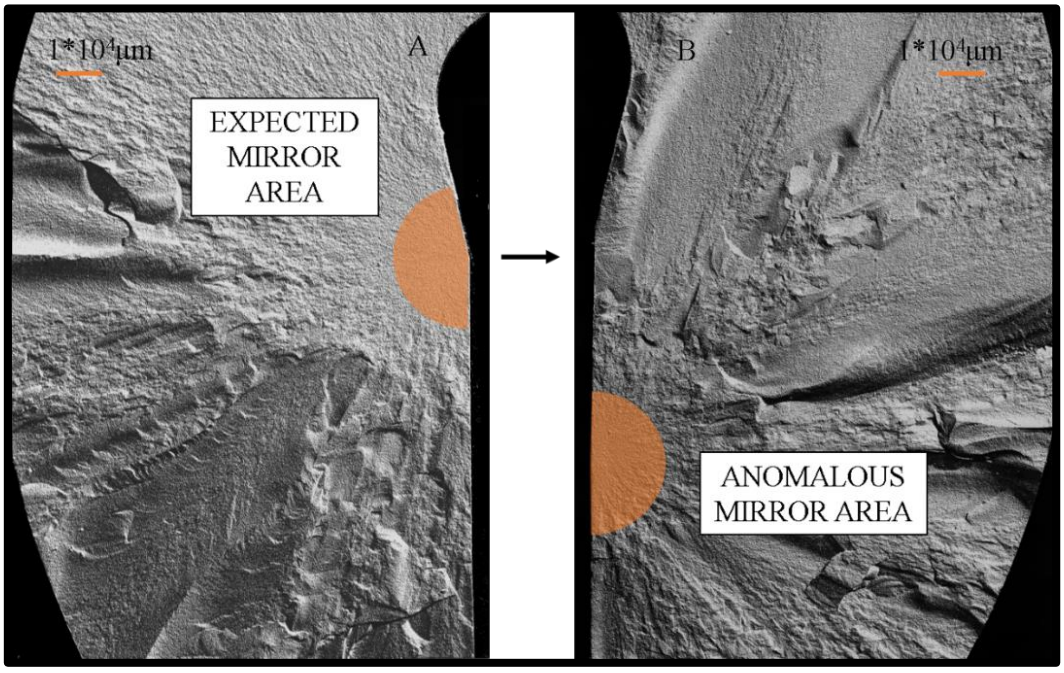

Fig.34: (A) Typical primary fragment with the origin of the fracture between the metal neck-stem and the endpoint of the taper, (B) anomalous point of origin of the fracture in a primary fragment.

6.4 Zirconia phase transformation

In several studies, it has been shown that the in vivo stability of the tetragonal polymorph, in ZTA artificial femoral heads, is based on simulations in a hydrothermally activated environment. The hydrothermal environment has an important influence on the stoichiometric state of tetragonal zirconia, favoring the transformation into monoclinic zirconia. In this study, we will see how in the femoral heads, the polymorphic transformation of the tetragonal zirconia depends on several factors such as hydrothermal ageing, fatigue testing, and energy release caused by the last step of the burst strength test. [93-94]

In the femoral heads, the tetragonal phase of the Zirconia is metastable, which means that by applying a loading effort, this accumulates on the tip of the crack, thus inducing the transition from tetragonal phase to monoclinic phase, with consequent expansion in volume on average of 3-4 %. It is known that phase transformation delays its propagation by increasing the fracture resistance capacity of the material. [95]

Consequently, it is possible through Raman spectroscopy to compare the intensities of the different peaks of the Zirconia phases by measuring the peaks shifts.

Below in Figure 35 is proposed the typical spectrum of a ceramic material in ZTA and the Katagiri equation to calculate the monoclinic zirconia fractions; considering the bands of the monoclinic phase at 181 and 190 cm^{-1}, the bands of the tetragonal phase at 147 cm^{-1}, and the correction factor "k" = 2.2 necessary to correct the scattering difference at the cross-section between monoclinic phase and tetragonal in the Raman bands. [96] The initial monoclinic fraction depends on the year of production. [97]

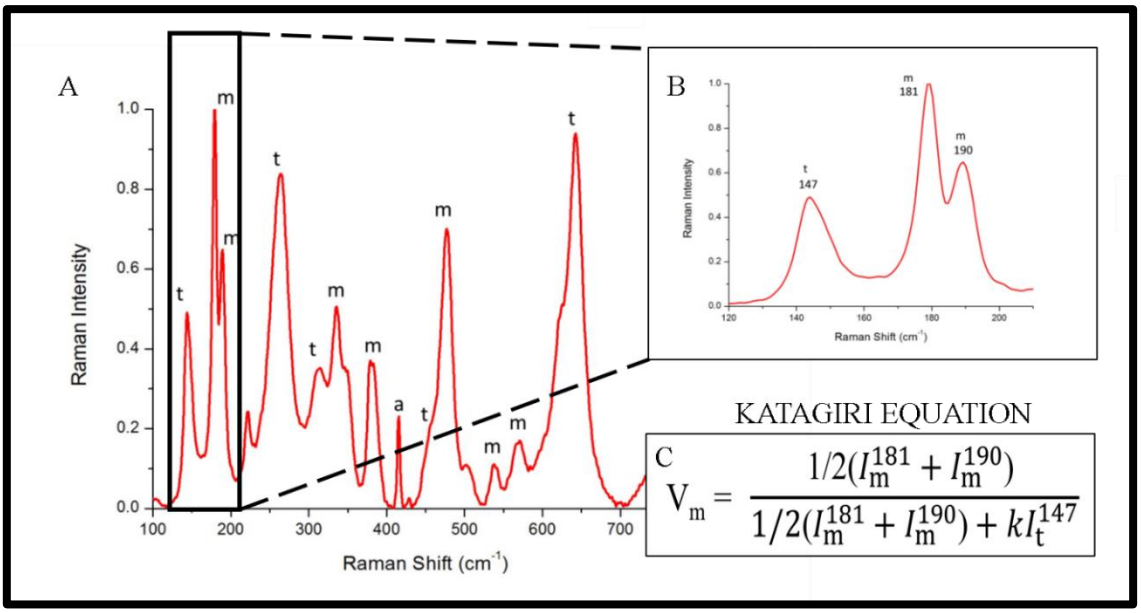

Fig.35: A) Representation of the typical spectrum for a ZTA ceramic material, B) peaks considered for the evaluation of the monoclinic fraction, C) Katagiri equation.

From an operational point of view, we work systematically on the mirror fracture, first under the laser microscope and then at the SEM, thus identifying the crack origin for each of the samples analysed.

For the Raman measurements of the fracture mirror, a semi-circular grid has been reproduced, as representative as possible of the mirror section, composed of 10 rays divided by 16.5 degrees for a total arc equal to 165 degrees. Furthermore, each radius was divided by three different circumferences about one millimeter apart (figure 36).

In each section obtained from the crossing of the rays, a 100 µm square scan was performed both along the X-axis and along the Y-axis, with 7 points analysed per row.

For the measurements of the monoclinic fraction on the external surfaces, eight maps were performed where the stress due to the burst strength test is minimal, precisely on the upper part of the femoral head. Also, in this case, the maps had a size of 100 µm per axis (X-Y), with 5 points analysed per row. Subsequently, the intensities and the shift of the peaks were processed using the Labspec software (Horiba / Jobin-Yvon., Kyoto, Japan).

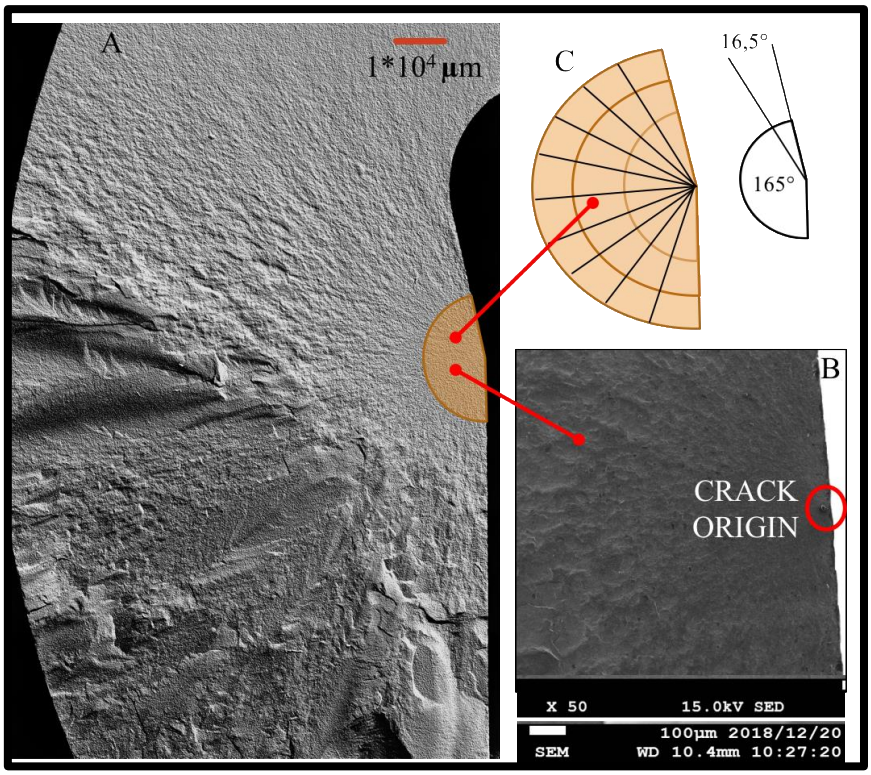

Fig.36: A) Total map of the primary surface obtained by a laser microscope, in B) the map is observed under a SEM scanning microscope and in C) the grid used for each sample during the Raman analysis.

Through Raman spectroscopy was studied the relationship between the monoclinic fraction present on the outer surface of the femoral heads and the monoclinic fraction present on the surface of the primary fragments, comparing the values obtained as a function of the simulated ageing for the CoCr trunnions. As shown in Figure 37, the decrease in mechanical properties is proportional to the increase in the monoclinic zirconia fraction, with an increase from about 6% to 23% on external surfaces and from 27 to 37% in the primary fracture area.

Proceeding in the analysis of the results obtained was observed that in the pristine femoral heads, the transformation of Zirconia from the tetragonal phase to the monoclinic phase is evident, passing from initial values between 5-7% to values between 26-29%. In this case, since there is no thermal degradation action that could influence the phase transformation, it is clear that the transformation depends solely on the stress caused by the fracture mechanism of the femoral head following the burst strength stress.

The transformation mechanism starts from the surface and proceeds through the more internal layers of the material, gradually reducing the mechanical properties.

Analysing instead the femoral heads subjected to heat treatment, we note that the phase transformation is markedly more accentuated (up to 44%). The phase transformation is not only influenced by the breaking stress of the material, as in the pristine samples, but also the hydrothermal aging and the release of energy caused by the final step of the burst strength test play a key role. However, for both femoral heads hydrothermally aged for 150 hours and 165 hours, the initial monoclinic volume fractions vary around 20%, while after the burst strength test, the monoclinic volume fraction in the severely loaded heads increases up to 35-40%.

Finally, the difference between the amount of monoclinic zirconia on the external surface and the fracture area was reduced with exacerbated test conditions, which means that the polymorphic transformation toughening mechanism was losing its effectiveness.

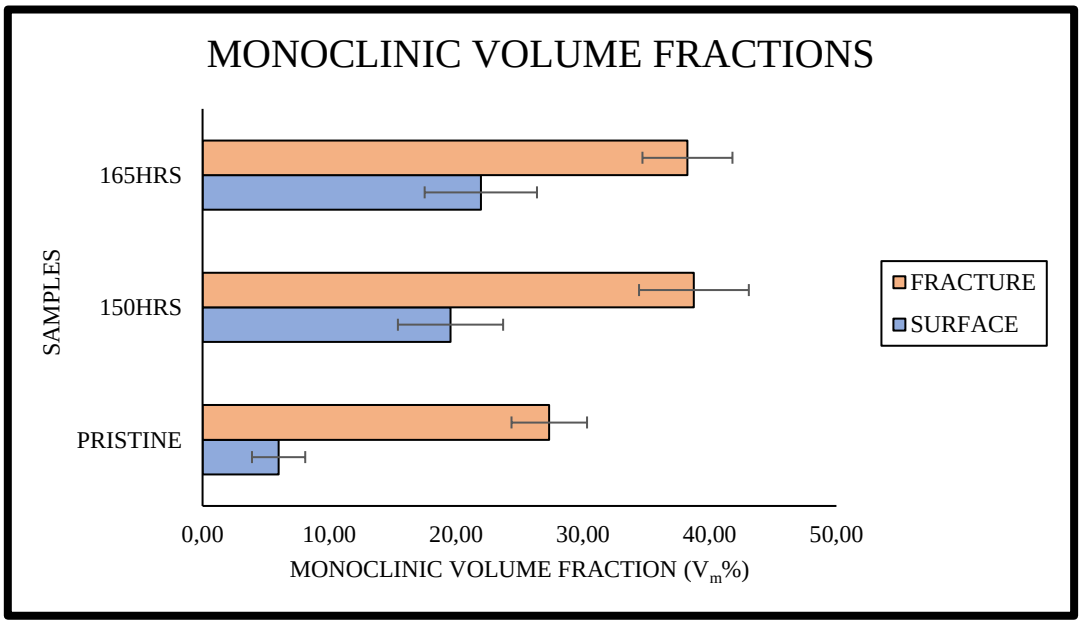

Fig.37: Monoclinic volume fractions (V_m%) measured on the external fracture surface (blue) and the internal fracture surface (orange).

6.5 Macroscopic evaluations

The fracture mirror is a smooth surface that surrounds the fracture origin through a circular or semi-circular shape. In polycrystalline ceramic materials and glass materials, there is a known correlation between applied breaking stress and mirror size. Usually, the fracture mirror is visible only for materials that offer a moderate or considerable fracture resistance, while in weak materials, the applied force leads to the formation of numerous small fragments. For weak samples, the typical confines of the mirror fracture do not occur because the crack does not achieve sufficient velocity within the boundaries of the sample.

Figure 38 shows the two equations that indicate the correlation between applied stress and mirror size, precisely in Figure 38A is proposed the general equation for ceramic and glass materials, while in Figure 38B is shown the simplified equation for fine-grained, stable polycrystalline alumina and other ceramics. In both equations, "σ" is the applied stress, "R" the radius of the mirror and "m" and "A" are constant. "A" is called "mirror constant" with units of stress intensity expressed in MPa√m, considered an intrinsic property of each ceramic material. [77]

Fig.38: A) general relationship between applied stress and mirror size; B) simplified the relationship between applied stress and mirror size.

In ceramic or glass materials the boundary between the fracture mirror and the "hackle area" is well defined and easily observable under an optical microscope; in the case of weaker materials, the smooth region of the mirror is less observable and extends broadly towards the inner part of the material, losing its circular or semi-circular shape.

For materials in which the border of the mirror fracture is visible, the equation used is shown in Figure 39B, where the average radius (R_{AVG}) of the fracture mirror is calculated along the three directions starting from the crack origin, R_1 and R_2 along the two lateral sides of the mirror and the radius R_d along the perpendicular direction.

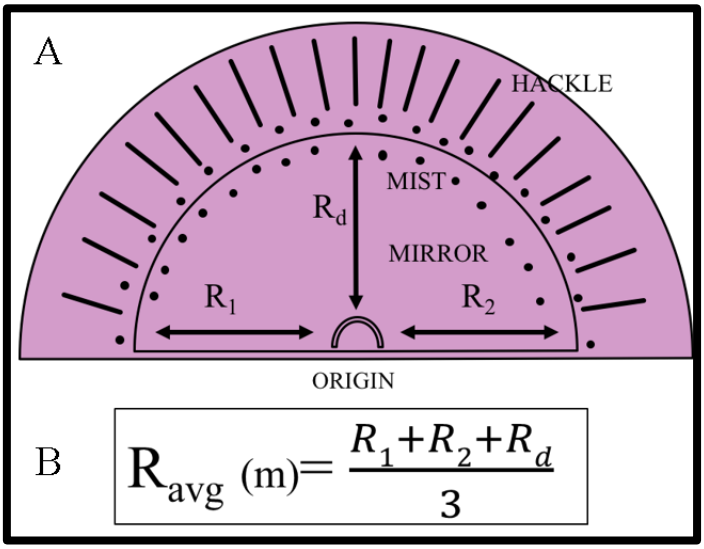

Fig.39: A) composition of the semi-circular mirror; B) equation for the calculation of the average R_{AVG} radius of the mirror.

Figure 40 shows the measurements performed on the fracture mirror of the femoral heads subjected to burst strength test, although it is evident that it is observed a large statistical dispersion for the radius values.

The average radius for pristine heads is larger than the average radius measured for hydrothermally aged femoral heads. There are no differences between the radius values measured in thermally degraded femoral heads. The difference observed between the radius values of the pristine femoral heads, and those hydrothermally aged indicates that the microstructure of the mirror fracture has memorized the residual stresses.

The polycrystalline ceramic material, subjected to hydrothermal ageing, generally reduces the ability to absorb mechanical stress by negatively affecting the mechanical performance of fracture resistance; however, there are no correlations between the initial load applied and the size of the mirror between the femoral heads. This means that although there is a reduction in the ability to absorb stress from the hydrothermally aged femoral heads, this is not sufficient to alter the fracture resistance of the material, which is why the initially applied breaking loads are similar to the pristine breaking loads.

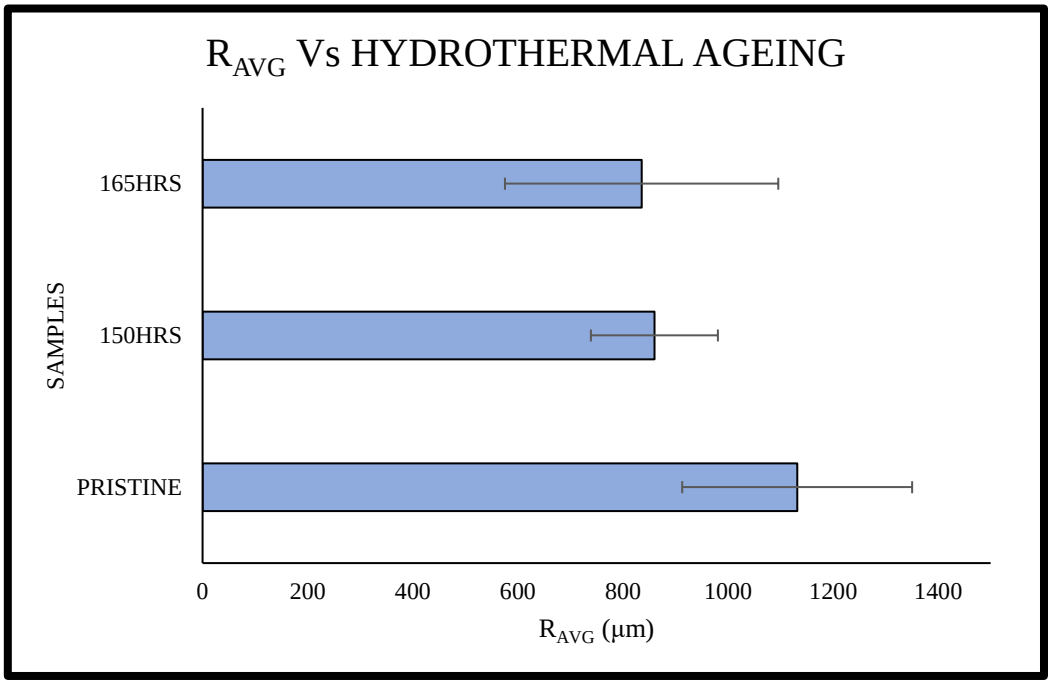

Fig.40: Radius of the mirror area as a function of the ageing conditions, using CoCr trunnions.

To measure the distribution of applied stresses, it was necessary to carry out a rough approximation, considering that in the development of the burst strength test, different contact areas can influence the final value of the applied stress and the calculation of the final residual stress. In this work, only the contact area between the trunnion and the internal conical surface of the femoral head was considered, neglecting the contact area between the support ring and the femoral head and the contact area between the ring and the conical bore loading. As shown in Figure 41B, the equation used for the calculation of the contact area considers "r_1" and "r_2" which are the upper radius and the lower radius

of the internal conical interface of the femoral head, “L” is the applied load, "l" is the length of the contact area. [98] As previously observed in Figure 30C, the metal contamination inside the conical surface of the femoral head is not constant but intensifies more and more as it reaches the upper part of the femoral head. Based on these considerations, the pressure along the contact area considered is not constant, so it was necessary to assume a parabolic stress distribution with a minimum at the lower radius and a maximum about five times higher than the minimum. [99][100] A more accurate estimate of the local stress “σ” can be obtained in the calculation of the residual stress through a “parabolic redistribution” of the estimate “σ’” along "l" considering the equation $\sigma(r_1) = 5\sigma(r_2)$. [98]

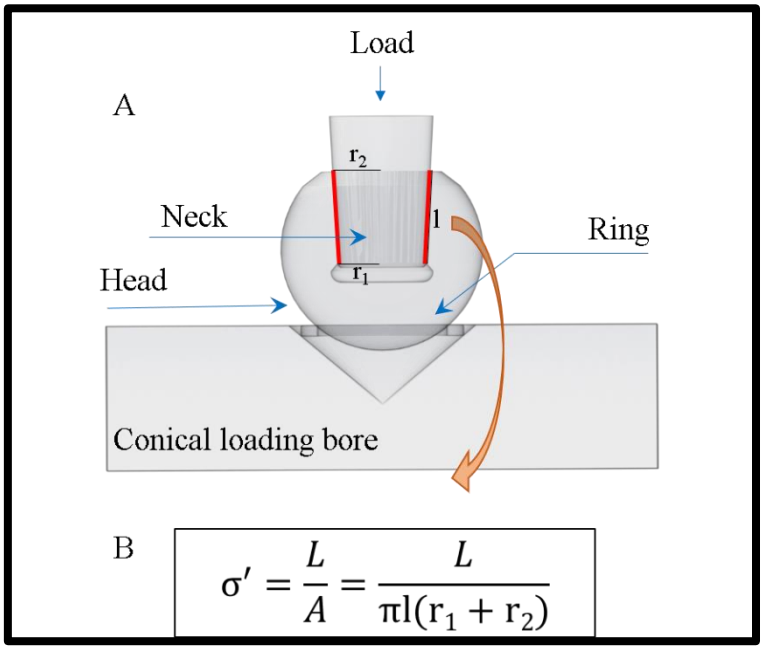

Fig.41: A) Arrangement of the elements during burst strength test wherein red is shown the contact area considered for the calculation of applied stresses; B) formula for the calculation of the considered contact area.

Once the stress values initially applied to the femoral head were obtained, it was possible to calculate the residual stresses through linear regression. This method is fundamentally based on the relation expressed in Figure 38B, where the square root of the average measured radius (R_{AVG}) of the mirror is proportional to the initially applied load (σ_a).

Furthermore, the whole macroscopic approach is based on the fact that measurements of the mirror sizes, even if recorded by computer software (Keyence, Osaka, Japan), retain a considerable error caused by the operator.

Starting from these considerations and the massive approximations performed, the final residual stresses (σ_{NET}) were calculated as a function of hydrothermal ageing for CoCr trunnions. As can be seen in figure 42, the influence of the hydrothermal treatment performed on artificial femoral heads is evident, in fact for the pristine femoral heads are reported values close to zero, while for hydrothermally aged femoral heads values are in the order of hundreds of MPa; consequently, as the ageing in the autoclave increases, the residual stress increases.

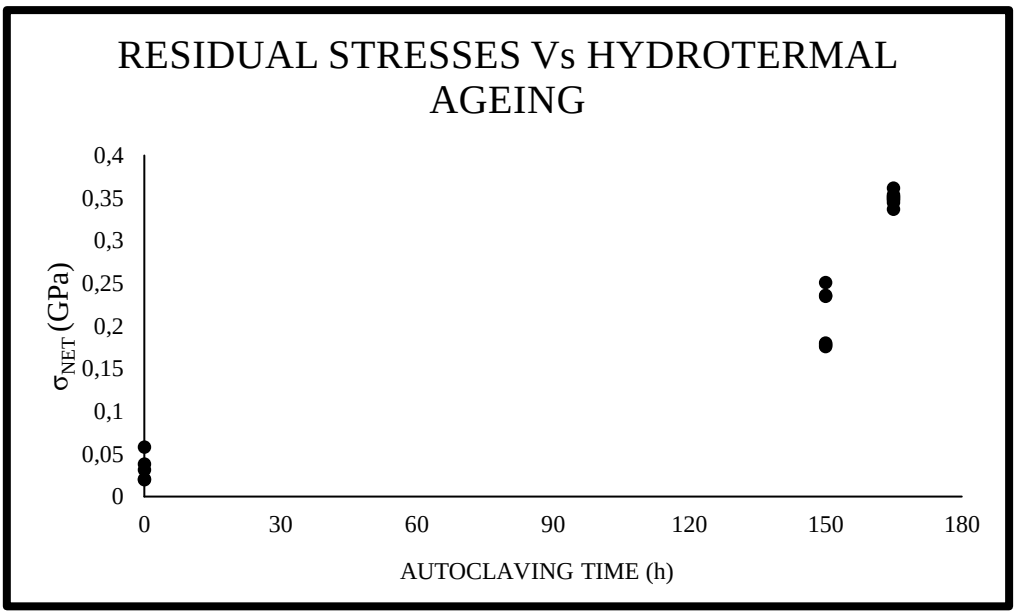

Fig.42: Residual stresses (σ_{NET}) of the mirror area as a function of the ageing conditions, using CoCr trunnions.

This macroscopic approach is to be considered representative in the relationship between femoral heads otherwise subjected to hydrothermal ageing, since the approximations made do not allow precise results. It was necessary to work with a more rigorous and precise method, trying to reduce experimental errors to a minimum and operating with instruments that allow the operator to reset errors.

6.6 Microscopic evaluations

Through a more precise analysis conducted by Raman spectroscopy, it was possible to reconstruct the distribution of the phase transformation from tetragonal to monoclinic over the entire primary surface of a hydrothermally degraded sample and a pristine sample. Starting from the grid used for the fracture mirror shown in figure 36, the measurements were performed in the same way on the whole fracture surface, through square maps from -250μm to +250μm distributed radially considering 21 points per row. The results of the distribution of the monoclinic fraction on the two studied surfaces are shown in figures 43 and 44. As already observed previously in paragraph 6.4, the content of monoclinic zirconia is higher for the hydrothermally aged femoral heads. From a first graphical analysis, two regions (A) and (B) were observed where the phase transformation is particularly high. These two areas extend almost symmetrically to the sides of the fracture mirror, the region (A) is believed to have been caused by mechanical contact (compressive stress) while the region (B) represents the point of maximum flexion effort not directly involved in the initial pressure, this means that in this region the transformation of tetragonal zirconia is caused by mechanical stresses of a tensile nature. Near the area (A) it is evident the presence of a region with a low level of zirconia transformation, as a consequence, it is clear how the high phase transformation caused by the contact stress, involves only the first millimeter of the material in contact with the trunnion without penetrating deep into the monolithic component; this effect is seen in both surfaces of the two samples.

By studying the distribution of the fraction of monoclinic zirconia in the area (C), it is evident the presence of a small region in which the phase transformation is minimal, it is identified in the center of the fracture mirror and is attributable to the crack origin.

In the region where crack propagation starts, there is a high accumulation of energy transferred during the burst strength test. Remembering that the fracture mechanism in ceramics is instantaneous, no energy dissipation is observed in the point of contact, but this is gradually radially transferred to the material. In this way, at the origin of the cracks, the minimal phase transformation is caused by the breaking of the chemical

bonds of the microstructure Furthermore, as stress influences the phase transformation, there is a 3-4% increase in volume in the grain size with definitive breakage of the material. It should also be remembered that the hypotheses on which this mechanism is based should be tried with further tests, first of all, the simulation with finite elements in which the stresses applied during the burst strength test could be correctly reproduced.
As further evidence of the proposed fracture mechanism, the fracture mirror can be considered from a morphological point of view, as previously studied, in the crack origin a bright transgranular fracture surface is expected; while moving away from the mirror, the intergranular fracture is expected with square grain size and sharp in their shape. This behavior could suggest that initially, the energy absorbed at the contact point is sufficient to break the bonds between the molecules with the cracks that propagate internally to the material, forming the ideally smooth surface of the fracture mirror.
However, as the energy is dissipated, the material absorbs this energy, causing phase transformation; the ceramic material undergoes a degradation phase in terms of mechanical properties with fracture propagation along the edge of the single weakened zirconia grains, leading to the final breakage of the material.
In the remaining regions of the primary surfaces, it is noted that in the hydrothermally degraded sample, the content of monoclinic zirconia is high and more widespread than in the pristine sample.

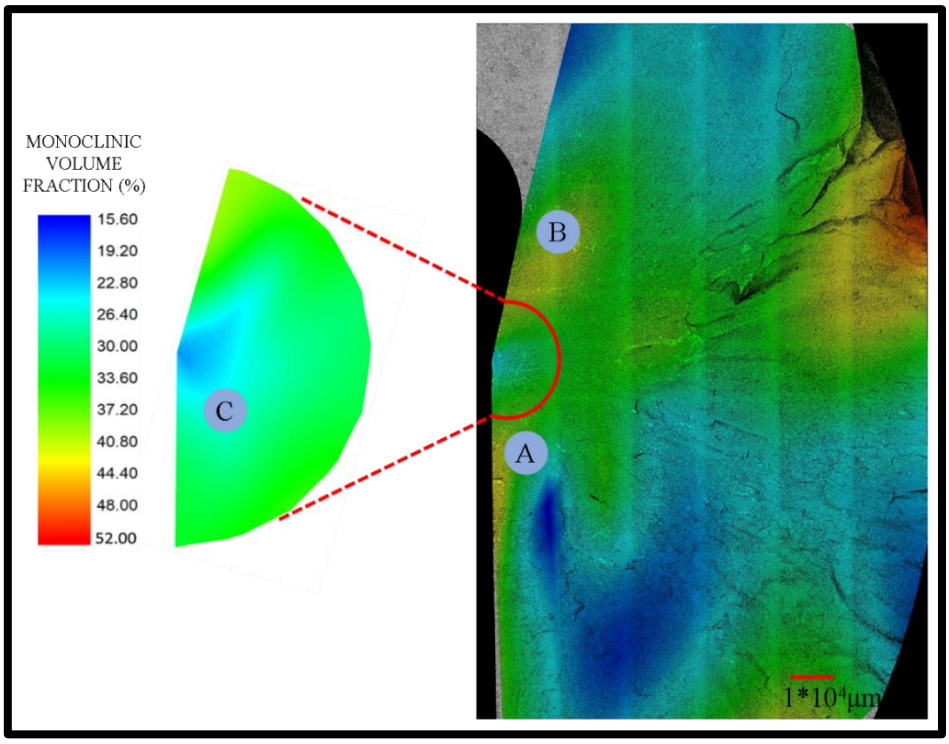

Fig.43: Fraction of monoclinic zirconia measured by Raman spectroscopy using the Katagiri equation on the primary fracture surface of a Pristine femoral head tested against CoCr trunnions.

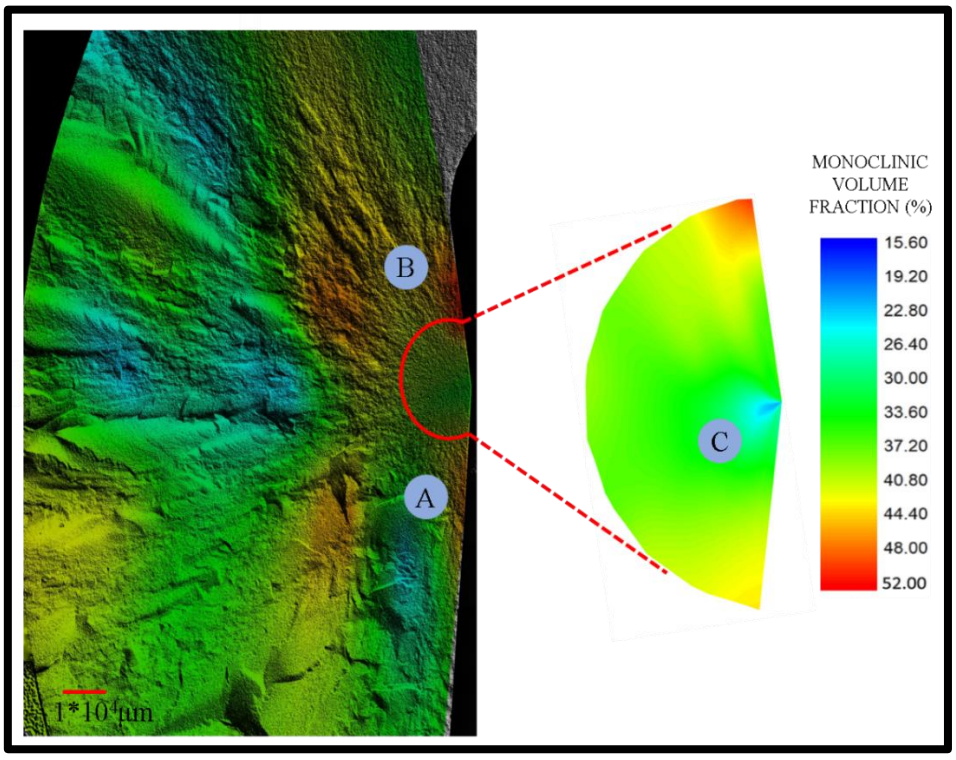

Fig.44: Fraction of monoclinic zirconia measured by Raman spectroscopy using the Katagiri equation on the primary fracture surface of an Autoclaved (150h) femoral head tested against CoCr trunnions.

To understand the influence of the low-temperature degradation on the fracture dynamics of the femoral heads and to interpret the residual stress values obtained ($\langle\sigma_{NET}\rangle$) for the ceramic composite material in the fracture mirror, it was necessary to use a mathematical algorithm (figure 45).

The residual stresses of the individual phases were previously calculated by dividing the relative shift of the peaks of the various elements (tetragonal zirconia, monoclinic zirconia and alumina), obtained by Raman spectroscopy, for the respective piezo-spectroscopic coefficients (-0.76; -0.60; -0.90cm^{-1}/ GPa).

$$\langle\sigma_{NET}\rangle = V_a\langle\sigma_a\rangle + V_z\,[V_m\langle\sigma_m\rangle + (1 - V_m)\langle\sigma_t\rangle]$$

Fig. 45: Formula used for the calculation of residual stresses.

In the mathematical equation shown in figure 45 the volume of the initial Alumina matrix (V_a) is equal to 80%, the volume of the total initial Zirconia fraction (V_z) is equal to 17%, the volume of the transformed monoclinic Zirconia fraction (V_m) was measured using the formula shown in figure 35C, the values $\langle\sigma_a\rangle$, $\langle\sigma_m\rangle$ and $\langle\sigma_t\rangle$ are the final residual stresses related to alumina, monoclinic zirconia and tetragonal zirconia. [98]

To correctly understand the results of the final residual stresses $\langle\sigma_{NET}\rangle$, it is necessary to remember that in Raman spectroscopy a shift of the relative peaks towards shorter wavelengths indicates the presence of tensile stress, while vice versa a shift of the peaks towards longer wavelengths indicates that there is compressive stress. It is essential to consider that the value of the alumina residual stress $\langle\sigma_a\rangle$ is constant and homogeneous in the sample throughout the hydrothermal degradation process without being influenced by the burst strength test; for residual stresses related to tetragonal zirconia $\langle\sigma_t\rangle$ and monoclinic $\langle\sigma_m\rangle$ point-by-point measurements are necessary in the various areas of the sample.

Following the grid shown in figure 36C, the shifts of the peaks of the different phases were analysed for both the moderately autoclaved sample for 150 h (figure 46A-C), and

the pristine sample (figure 46E-G), and subsequently it was calculated, in the fracture mirror, the final residual stress $\langle \sigma_{NET} \rangle$ for both samples, figures 46D and 46H.

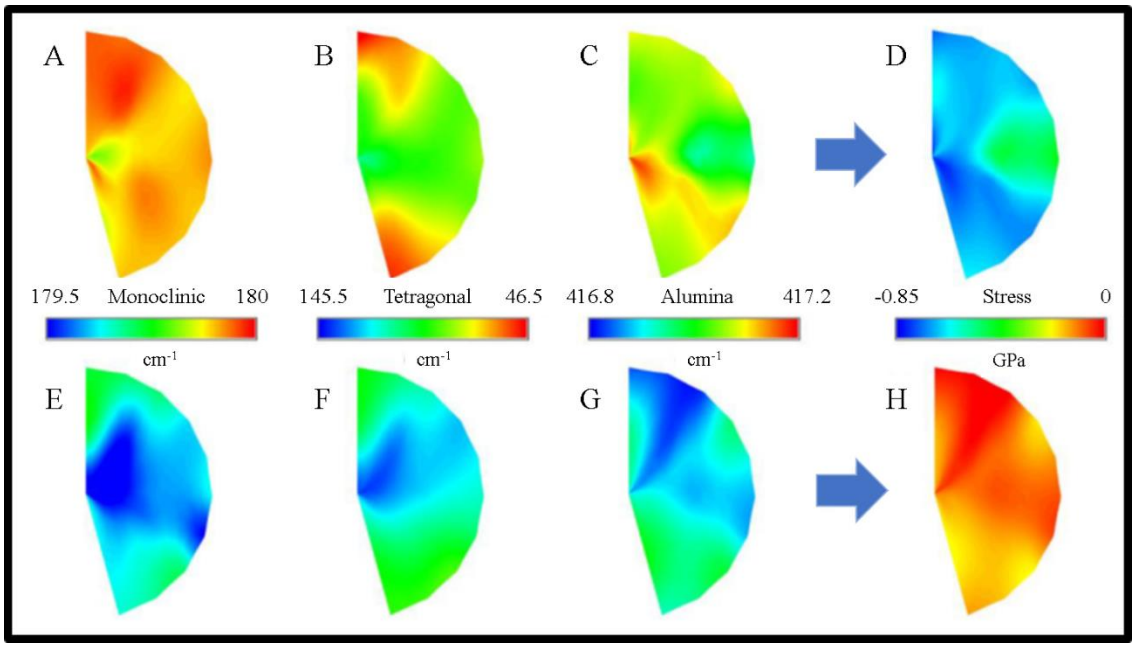

Fig. 46: A), B), C) Raman shifts of monoclinic zirconia, tetragonal zirconia, and alumina for the hydrothermally degraded sample; E), F), G) Raman shifts of monoclinic zirconia, tetragonal zirconia and alumina for the pristine sample; D) and H) final residual stress of the hydrothermally degraded sample and the pristine sample.

Regarding the Raman shifts of the peaks of the aged sample, final residual compressive stress values of up to 850MPa were detected, observing that the bands of the peaks of the three different phases oscillate towards longer wavelengths than the pristine sample taken as a reference. Near the point where the crack originates, is recorded the highest point of residual compressive stress (figure 46D). In the pristine sample, the residual stresses are mostly close to zero, and the Raman shifts for the different phases fall at lower wavelengths. If observing the distribution of the Raman shifts, there is no particular trend; in the case of residual stresses, there is a very similar distribution, even if for pristine, the values are close to zero. However, minimal residual stress values were observed for both samples in the center of the fracture mirror. An interesting hypothesis concerns the correlation between the distribution of residual stresses on the fracture

mirror and the distribution of the monoclinic zirconia fractions on the primary fracture surfaces of the samples (figure 47).

Looking at both global distributions, two main areas emerge one inclined by about 30 degrees respect to the application load axis (white arrows in figure 47) and one parallel to the same axis along the taper (black arrows in figure 47).

The arrows respectively show areas with a high fraction of monoclinic zirconia and areas where the residual stress value is great. This phenomenon is particularly marked in the aged sample. Furthermore, it is observed that the minimum values of the monoclinic fraction and residual compressive stress are recorded at the center of each distribution.

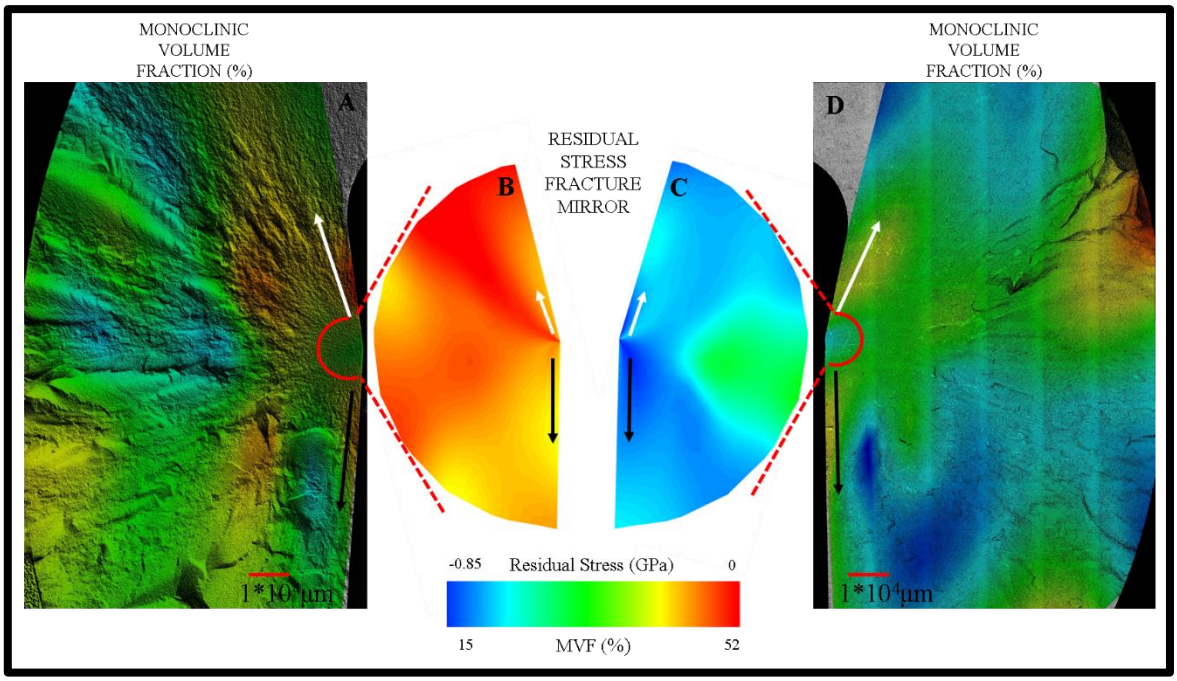

Fig.47: A-B Monoclinic volume fractions (MVF %) and fracture mirror residual stress measured on fracture surface for an autoclaved sample, C-D monoclinic volume fractions (MVF %) and fracture mirror residual stress measured on fracture surface for a pristine sample.

In the study conducted by Huang et all. [101] the presence of residual compressive stress on a fracture surface initially reduces the volume expansion of the polymorphic transformation, since at the point of contact, there is no energy dissipation, and only afterward there is the dissipation of the stored energy.

Similarly, it is hypothesized that the presence of the residual stresses observed on the fracture mirror may have directed the phase transformation from tetragonal zirconia to monoclinic along the primary fracture surface of the samples. Simultaneously with the dissipation of energy along with the possible directions, there is an increase in the phase transformation of zirconia, as previously observed in points A and B of figures 43 and 44. It can be assumed that in the fracture mirror, compressive stress slows down the phase transformation of zirconia, and this could explain the radial distribution seen in images 43 and 44. Subsequently, along the direction shown in figure 47 by the black arrows, there is a higher phase transformation caused by mechanical contact, while along the direction shown by the white arrows, there is a more significant phase transformation caused by mechanical bending stresses. It is worth noting that on any surface analysed, an overall residual stress value of zero should be expected. The presence of a non-zero value indicates the presence of a non-zero effort. This phenomenon can be explained mainly in two ways: in the fracture mirror, there are compressive stresses, and these are, in turn, balanced by tensile stresses in regions outside the analysed area, or the probe of the Raman instrument used it is not sensitive enough. In the second case, please note that the sensitivity of the instrument with which the measurements were made is approximately 3-5µm and depends on the sample material and its roughness.

To understand if the overall balance of stress could occur going down in-depth, the surface of the fracture mirror of the pristine sample was analysed with the Raman set in confocal mode. The in-depth analyses take a long time to obtain an adequately analysable signal, for this reason, the surface of the fracture mirror was divided into three macro-areas (zone A, zone B, zone C), each area was analysed through a square map from -100 µm to +100 µm along the X and Y axes, with 7 points per line; the steps at 5 µm, 10 µm, 20 µm, 50 µm, and 100 µm were chosen (figure 48B).

Figure 48A shows the trend of the residual stress values calculated by going down in-depth. The graph shows that there is no total stress balance. Still on the contrary, initially, there is a random trend between the different areas with values that are oscillating between -0.1 and -0.3GPa, at greater depths, on the other hand, the highest amounts of compressive stress are recorded. The profile observed in the graph would suggest the presence of a non-zero load effort on the material. To justify this trend, it is

necessary to remember the two hypotheses made previously concerning either the low sensitivity of the Raman instrument or the fact that the tensile residual stresses, which should lead to an overall balance of the residual stresses, have not been measured as they are probably far from the analysed area.

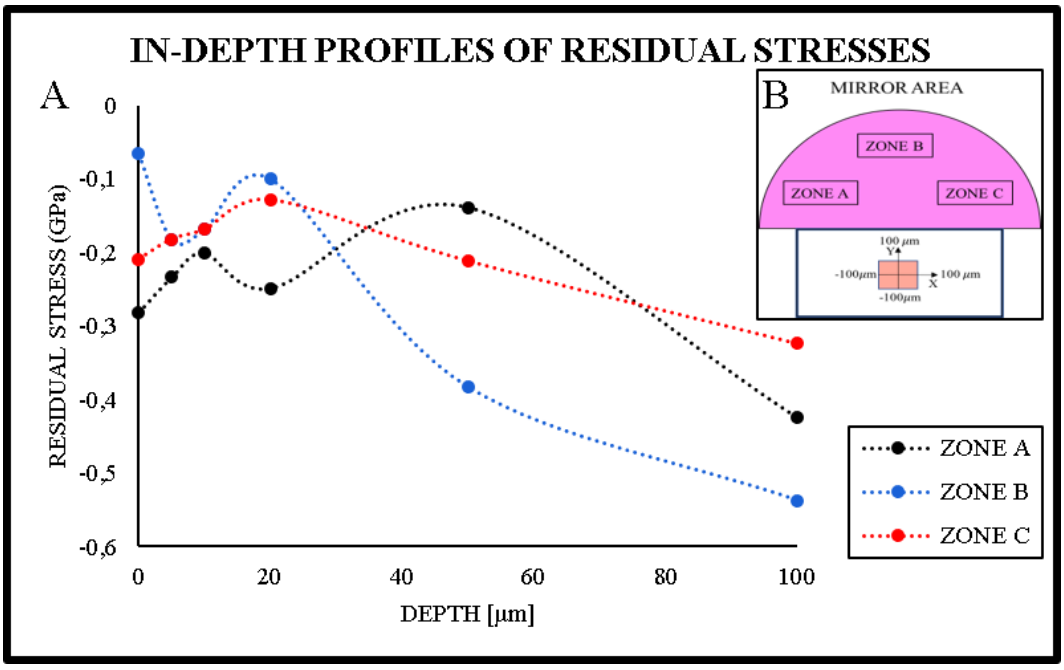

Fig.48: A) In-depth profiles of residual stresses in three different fracture mirror regions as measured by Raman spectroscopy; B) representation of the three areas considered.

Subsequently, the depth trend of the polymorphic transformation from tetragonal zirconia to monoclinic zirconia was studied, using the three regions similarly shown in Figure 48B. Figure 49 shows the depth profile of the fraction of monoclinic zirconia as a function of hydrothermal aging. Going down from 0 to 100µm, the volume of monoclinic zirconia decreases as depth increases in all three areas considered; initially, the monoclinic fraction decreases more rapidly to a depth of 20µm and then drops continuously to a depth of 100µm. A second consideration to make concerns the fact that the surface values of monoclinic zirconia are about 50% greater than the values recorded at a depth of 100µm; this means that the stress related to the breakage of the material contributed to the surface polymorphic transformation, also considering that the sample was not hydrothermally degraded.

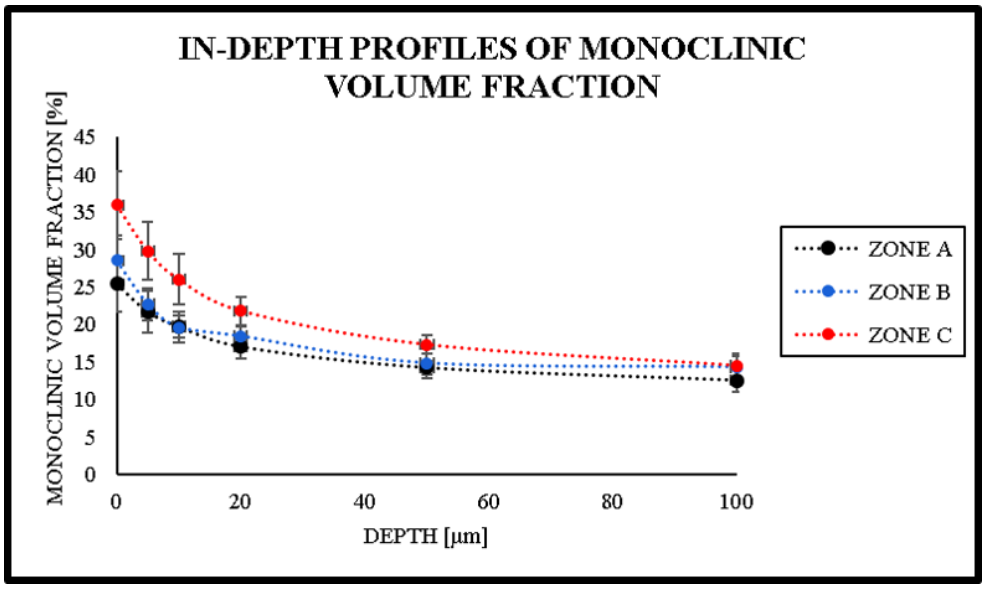

Fig.49: In-depth profiles of monoclinic volume fractions in three different fracture mirror regions, as measured by Raman spectroscopy using the Katagiri equation.

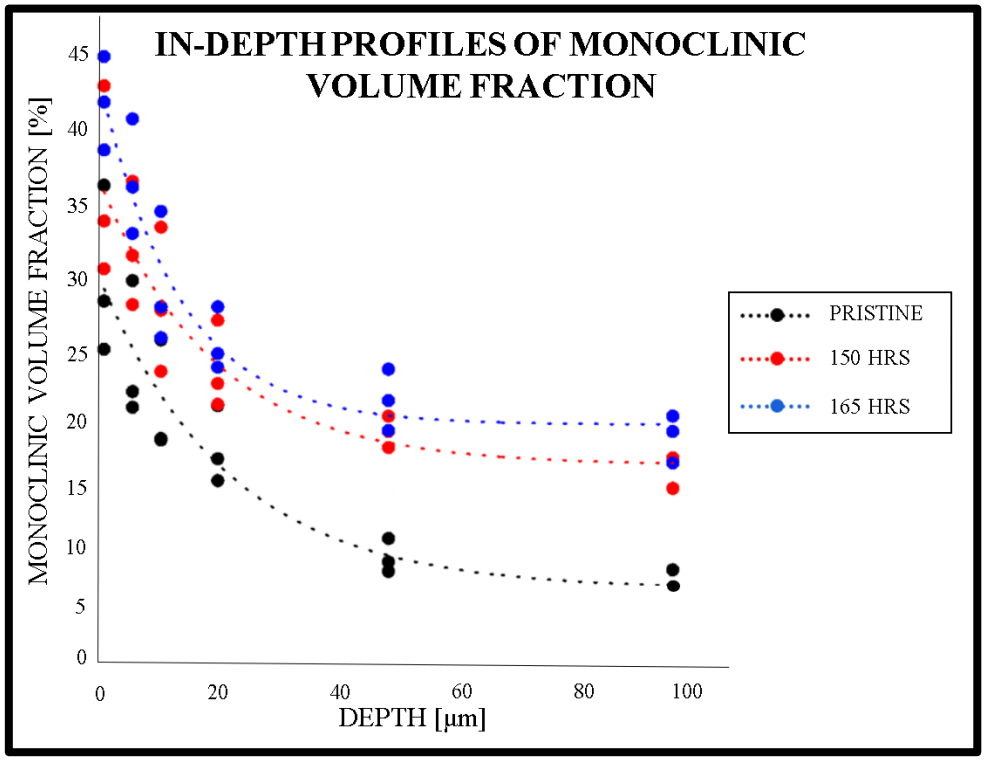

Fig.50: In-depth profiles of monoclinic volume fractions in three different fracture mirror regions as a function of hydrothermal aging, as measured by Raman spectroscopy using the Katagiri equation.

The in-depth profiles of the degree of polymorphic transformation from tetragonal zirconia to monoclinic for the aged femoral heads for 150 hours and 165 hours have also been studied. As shown in Figure 50 and as previously observed, going down in-depth, there is a decrease in the volume of the fraction of monoclinic zirconia also for the degraded femoral heads while maintaining generally higher values compared to pristine samples. The values of the monoclinic fraction are higher for the aged femoral heads. Still, as in the pristine samples, moving away from the surface, a decrease of about 50% of the monoclinic volume fraction is observed. The monoclinic volume fraction decreases rapidly up to 20 μm and then more constant up to 100 μm.

7. CONCLUSIONS

In this work, the effects of hydrothermal ageing on BIOLOX® delta femoral heads subjected to burst strength test were studied, first with a fractographic approach, allowing the reconstruction of fracture dynamics, and then by Raman spectroscopy. Eighteen femoral heads were studied; they were hydrothermally degraded in an autoclave according to different ageing steps, and after, they were subjected to the burst strength test. All femoral heads reported breaking values higher than 42 kN, the minimum amount imposed by the US FDA. According to studies reported in the literature [86] [89] the average values of the breaking loads are higher than those obtained in this work (~58kN for pristine samples, ~55 kN for samples aged in the autoclave for 150 hours); however, it is necessary to consider that the ISO 7206-10 test was conducted with CoCr trunnions and not with Ti_6Al_4V and that the femoral heads analysed by us all had a diameter of 28mm.

Through the fractographic approach, it was possible to reconstruct the fracture dynamics that the ceramic material undergoes; also, the typical elements of a fracture surface were defined from a morphological point of view, identifying regions characterized by intergranular and transgranular fractures. Using the Raman spectroscopy and the related mathematical equations, it was possible to calculate the distribution of the fraction of monoclinic zirconia and the distribution of residual stresses along the primary fracture surfaces. The monoclinic fraction grows linearly as a result of hydrothermal aging as also observed in previous academic studies [59], it has been observed that along the surfaces directly involved in the fracture, the degree of surface transformation from tetragonal zirconia to monoclinic zirconia is greater than 50 % respect to internal regions (at a depth of 100μm from the surface) and not directly subjected to breakage stress. As observed in figure 40, the decrease in the radius of the fracture mirror as a function of hydrothermal aging is a symptom that the residual stress is stored in the microstructure of the polymorphic material, the composite ceramic material reduces the ability to mechanically absorb the stress with consequent reduction of the mechanical

performance. Based on these considerations, it has been proved that, where the fracture originates, the fraction of monoclinic zirconia is less than in the areas of contact with the taper or where the binding stress is maximum. This behavior is supported by the fact that the propagation of the cracks has directly influenced the polymorphic transformation, so that along the transgranular fracture surfaces, typical of the fracture mirror, there is a reduced transformation from tetragonal to monoclinic.

Fracture mirror surfaces were analysed to find out whether degradation at low temperatures could influence the distribution of residual stresses. Thanks to a rigorous approach based on Raman measurements, it has been observed that in the aged samples, there are higher values of residual compressive stress. As shown by the comparison, in figure 46D-H, between the pristine and aged samples, it is evident that a low-temperature degradation played a key role. As reported in previous academic studies, contact stress can be dissipated through crystallographic transformation [59], however for autoclaved samples, given the high content of monoclinic zirconia, the microstructure has probably not been able to absorb the same amount of energy compared to pristine samples.

Concerning residual stresses, a balance between compressive and tensile stresses was not observed, even after in-depth analysis. Still, the distribution of residual compressive stress mainly in two directions has been found, one inclined respect to the load application axis and one parallel to the axis along the contact region between trunnion and taper.

This study would need to be accompanied by an analysis with the finite elements, to have an accurate simulation of how the contact stresses are distributed between the trunnion and the femoral head. The simulated analysis would allow understanding better if there is a correlation between the distribution of residual stresses on the fracture mirror and the distribution of the monoclinic fraction along the primary fracture surface.

8. BIBLIOGRAPHY

1. Liu X. W., Zi Y., Wang Y., Total hip arthroplasty: a review of advances, Advantages and limitations. International journal of clinical and experimental medicine. Vol 8(1), pp. 27-36, 2015.

2. Dietrich, M.D., H; Leyen, S., Ceramic Implants for Joint Arthroplasty, Experiences and Visions, CeramTec AG Germany, pp.1-4, 2004

3. Rieger W., Claude R S.O., Wyss U., Humber H., Ceramics in Orthopedics - 30 years of Evolution and Experience, in World Tribology Forum in Arthroplasty, Bern Editor, 2001.

4. Kurtz, S.M., UHMWPE Biomaterials Handbook - Ultra-High Molecular Weight Polyethylene in Total Joint Replacement and Medical Devices (2nd Edition) Elsevier, 2009.

5. BIOLOX® delta Nanocomposite for Arthroplasty the Fourth Generation of Ceramics, CeramTec AG: Germany, pp. 1-15, 2006.

6. Weisse, B., Improvement of the reliability of ceramic hip joint implants. Journal of Biomechanics. Vol. 36(11), pp. 1633-1639, 2003

7. Huet, R., A. Sakona, and Kurtz S.M., Strength and reliability of alumina ceramic femoral heads: Review of design, testing, and retrieval analysis. Journal of the Mechanical Behavior of Biomedical Materials. Vol 4(3), pp. 476-483, 2011.

8. Pospula W., Total hip replacement: past present and future. Kuwait Medical Journal. Vol. 36(4), pp. 250-255, 2004.

9. Smith-Petersen M.N., Treatment of malum coxae senilis, old slipped femoral epiphysis, intrapelvic protrusion of the acetabulum, and coxa plana by means of acetabuloplasty. J Bone Joint Surg. Vol.18, pp.869-884, 1936.

10. Smith-Petersen M.N., Evolution of mould arthroplasty of the hip joint. J Bone Joint Surg. Vol. 30B, pp. 59-74, 1948.

11. Signorello L.B., Ye W., Fryzek J.P., Lipworth L., Fraumeni JF Jr., Blot W.J., McLaughlin J.K., Nyren O., Nationwide study of cancer risk among hip replacement patients in Sweden. J Natl Cancer Inst. Vol. 93(18), pp.1405-1410, 2001.

12. Steinberg M.E., Reconstructive Surgery of the adult Hip: an overvieww. In the hip and its disorders. Philadelphia, WB Saunders Company. Vol. 32, pp. 705-727, 1991.

13. Charnley J.C., Arthroplasty of the hip: a new operation. Lancet. Vol. 1, pp. 1129-1132, 1961.

14. Tanaka S., Surface replacement of the hip joint., Clin. Orthop.Vol.134, pp. 75-79, 1978.

15. Paltrinieri M., Trentani C., Variante di artro-protesi d'anca. Chir. Org. Mov. Vol. 60, pp. 85-95, 1971.

16. Howie D.W., Cornish B.L., Vernon-Roberts B., Resurfacing Hip Arthroplasty. Classification of Loosening and the Role of Prosthesis Wear Particles. Clin. Orthop. Vol. 255, pp.144-159, 1990.

17. Wroblewski B.M., Fleming P.A., Siney P.D., Charnley low frictional torque arthroplasty of the hip, 20 to 30year results, Journal of Bone and Joint Surgery. Vol. 81, pp. 427-430, 1999.

18. Müller M. E., Lessons of 30 years of total hip arthroplasty. Clin. Orthop. Vol. 274, pp.12-21, 1992.

19. Mittelmeier H., Heisel J., Sixteen-years' experience with ceramic hip prostheses. Clin Orthop Relat Res. Vol. 282, pp. 64–72, 1992.

20. Shikata T., Oonishi, H., Hashimato Y., Wear resistance of irradiated UHMW polyethylenes to alumina ceramics in total hip prostheses. Transactions of the 3rd Annual Meeting of the Society for Biomaterials. Vol. 3, pp.118- 127, 1977.

21. Pezzotti G., Yamada K., Sakakura S., Pitto R.P., Raman spectroscopic analysis of advanced ceramic composite for hip prosthesis, Journal American Ceramic Society. Vol. 91, pp.1199–1206, 2008.

22. Weber B.G., Experience with the Metasul total hip bearing system. Clin Orthop. Vol. 329S, pp. 69-77, 1996.

23. Wagner M., Wagner H., Preliminary results of uncemented metal on metal stemmed and resurfacing hip replacement arthroplasty. Clin. Orthop. Vol. 329S, pp. 78-88, 1996.

24. McMinn D., Treacy R., Lin K., Pynsent P., Metal on Metal Surface Replacement of the Hip. Experience of the McMinn Prosthesis. Clin. Orthop. Vol. 329S, pp.89-98, 1996.

25. Clarke I.C., Manaka M., Green D.D., Williams P., Pezzotti G., Kim Y.H., Ries M., Sugano N., Sedel L., Delauney C., Nissan, B.B., Donaldson T., Gustafson G.A., Current status of zirconia used in total hip implants. The Journal of bone and joint surgery. American. Vol. 85(4), pp. 73-84, 2003.

26. Sheth N.P., Lementowski P., Hunter G., Garino J.P., Clinical applications of oxidized zirconium. Journal of surgical orthopedic advances. Vol. 17, pp.17-26. 2008.

27. Kurtz S.M., UHMWPE Biomaterials Handbook - Ultra-High Molecular Weight

Polyethylene in Total Joint Replacement and Medical Devices (2nd Edition), Elsevier, 2009.

28. Chevalier J., Grandjean S., Kuntz M., Pezzotti G., On the kinetics and impact of tetragonal to monoclinic transformation in an alumina/zirconia composite for arthroplasty applications, Biomaterials. Vol. 30 (29), pp. 5279–5282, 2009.

29. McEntire B.J., Lakshminarayanan R., Ray D.R., Clarke I.C., Puppulin L., Pezzotti G., Silicon nitride bearing for total joint arthroplasty. Lubricants, Vol. 4, pp. 23-35, 2006.

30. Siopack J.S., Jergesen H.E., Total Hip Arthroplasty, Western Journal of Medicine. Vol.162, pp. 243-249, 1995.

31. Pluot E., Davis E.T., Revell M., Davies A.M., James S.L.J., Hip Arthroplasty. Part 1: prosthesis terminology and classification, Clinical Radiology. Vol. 64, pp. 954-960, 2009.

32. Frank H., Netter M.D., Atlante di Anatomia Fisiopatologia e Clinica, Apparato Muscolo-Scheletrico. Vol. 8, Parte I, 1999.

33. Byrne D.P., Mulhall K.J., Baker J.F., Anatomy of Biomechanics of the Hip, The Open Sports Medicine Journal. Vol. 4, pp. 51-57, 2010.

34. Giannini S., Faldini C., Manuale di Ortopedia e Traumatologia, Edizioni Minerva Medica. 2008.

35. Morlock M., Bishop N., Huber G., Biomechanics of Hip Arthroplasty. Tribology in Total Hip Arthroplasty Vol. 12, pp.11-24, 2011.

36. Siopack J.S., Jergesen H.E., Total Hip Arthroplasty. Western Journal of Medicine. Vol. 162, pp. 243-249, 1995.

37. Del Pozo J.L., Patel R., Infection associated with prosthetic joints. New England Journal of Medicine. Vol. 361, pp.787-794, 2009.

38. Robbins S.L, Cotran R.S., Le basi fisiologiche delle malattie. Piccin Editore, 1982.

39. Kabo J.M, Gebhard J.S, Loren G., Amstutz H.C., In vivo wear of polyethylene acetabular components. Journal of Bone and Joint Surgery. Vol. 75, pp.254-258, 1993.

40. Willert H.G., Semlitsch M., Tissue reactions to plastic and metallic wear products of joint endoprostheses. Clinical Orthopedics and Related Research. Vol. 333, pp. 4-14, 1996.

41. Bordini B., Stea S., Clerico M. D., Strazzari S., Sasdelli A., Toni A., Factors affecting aseptic loosening of 4750 total hip arthroplasties: Multivariate survival analysis. BMC Musculoskeletal Disorders. Vol. 8 (1),2007.

42. Black J., Biological Performance of Materials: Fundamentals of Biocompatibility, New York: Marcel Dekker, 1992.

43. Holzwarth U., Cotogno G., Total Hip Arthroplasty: state of arts, challenges and prospects. European Commission, Joint Research Centre, Institute for Health and Consumer Protection. 2012.

44. Cigada A., Chiesa R., Pinasco M., and Hisatsune K., Metallic Materials. Integrated Biomaterials Science (R. Barbucci, ed.), Springer US. Vol.1, pp. 255–296, 2002.

45. Navarro M., Michiardi A., Castano O., Planell, J. A., Biomaterials in orthopedics. Journal of The Royal Society Interface. Vol. 5(27), pp.1137-1158, 2008.

46. Ozturk O., Turkan U., Eroglu A. E., Metal ion release from nitrogen ion implanted CoCrMo orthopedic implant material, Surface & Coatings Technology. Vol. 200(20-21), pp. 5687-5697, 2016.

47. Süry P., and Semlitsch M., Corrosion behavior of cast and forged cobalt-based alloys for double-alloy joint endoprostheses, J Biomed Mater Res A. Vol. 12, pp. 723–741, 1978.

48. Eisenbarth, E., Velten, D., Muller, M., Thull, R., Breme, J., Biocompatibility of stabilizing elements of titanium alloys, Biomaterials. Vol. 25(26), pp. 5705-5713, 2004.

49. Heness G., and Ben-Nissan B., Innovative bioceramics, Mater Forum. Vol. 27, pp. 104–114, 2004.

50. Ramakrishna S., Mayer J., Wintermantel E., Leong K. W., Biomedical applications of polymer composite materials: A review. Composites Science and Technology. Vol. 61(9), pp.1189-1224, 2001.

51. Pietrzak W. S., Sarver D. R., and Verstynen M. L., Bioabsorbable Polymer Science for the Practicing Surgeon, Journal of Craniofacial Surgery. Vol.8(2), pp. 87-91, 1991.

52. Stein H., Ultrahigh molecular weight polyethylene (UHMWPE), ASM International, Engineering Plastics, Engineered Materials Handbook, Vol. 2, pp. 167–171, 1988.

53. Kurtz S., UHMWPE Biomaterials Handbook: Ultra High Molecular Weight Polyethylene in Total Joint Replacement and Medical Devices. Academic, 2009.

54. Deng M., Shalaby S. W., Properties of self-reinforced ultra-high molecular weight polyethylene composites, Biomaterials. Vol.17, pp. 977-982, 1997.

55. Muratoglu O. K., Wannomae K., Christensen S., Rubash H. E., Harris W. H., Ex vivo wear of conventional and crosslinked polyethylene acetabular liners, Clinical Orthopedics and Related Research. Vol 438, pp.158–164, 2005.

56. Oral E., Muratoglu O., Vitamin E diffused, highly crosslinked UHMWPE: a review, Int Orthop., Vol. 35, pp. 215–223, 2011.

57. Lewis G., Properties of crosslinked ultra-high-molecular-weight polyethylene, Biomaterials. Vol. 22, pp. 371–401, 2001.

58. Zietz C., Kluess D., Bergschmidt P., Haenle M., Mittelmeier W., Bader R., Tribological aspects of ceramics in total hip and knee arthroplasty, Semin Arthroplasty. Vol. 22, pp. 258–263, 2011.

59. Pezzotti G., Kiyotaka Y., Seiji S., Pitto R.P., Raman spectroscopic analysis of advanced ceramic composite for a hip prosthesis. Journal of the American Ceramic Society. Vol. 91, pp.1199–1206, 2008.

60. Elpers M., Nam D., Boydston-White S., P-Ast M., M Wright P, Padgett E., Zirconia phase transformation, metal transfer, and surface roughness in retrieved ceramic composite femoral heads in total hip arthroplasty. The Journal of arthroplasty. Vol. 29(11), pp.2219–2223, 2014.

61. Chevalier J., Taddei P., Gremillard L., Deville S., Fantozzi G., Bartolomé J., Pecharroman C., Moya J., Diaz L., Torrecillas R., Affatato S., Reliability assessment in advanced nanocomposite materials for orthopaedic applications, J. Mech Behav. Biomed Mater. Vol. 4, pp. 303–314, 2011.

62. Gutknecht D., Chevalier J., Garnier V., Fantozzi G., Key role of processing to avoid low-temperature ageing in alumina-zirconia composites for orthopedic application. Journal of the European Ceramic Society. Vol. 27(2-3), pp.1547-1552, 2007.

63. Shin D. W., Orr K.K., Schubert H., Microstructure-Mechanical Property Relationships in Hot Isostatically Pressed Alumina and Zirconia-Toughened Alumina, Journal of the American Ceramic Society. Vol73(5), pp.1181-1188, 1990.

64. Burger W., Richter H.G., High Strength and Toughness Alumina Matrix Composites by Transformation Toughening and 'In Situ' Platelet Reinforcement (ZPTA) - The New Generation of Bioceramics. Key Engineering Materials, Vol.192-195, pp.545-548, 2001.

65. Schneider J., Begand S., Kriegel R., Kaps C., Glien W., Oberbach T., Low-temperature aging behavior of alumina-toughened zirconia. Journal of the American Ceramic Society. Vol. 91(11), pp. 3613-3618, 2008.

66. Piconi C., and Maccauro G., Zirconia as a ceramic biomaterial. Biomaterials. Vol. 20(1), pp.1-25,1999.

67. Elpers M., Nam D., Boydston-White S., Ast M. P., Mwright T., Padgett D.E., Zirconia phase transformation, metal transfer, and surface roughness in retrieved ceramic composite femoral heads in total hip arthroplasty. The Journal of Arthroplasty. Vol. 29(11), pp. 2219-23, 2014.

68. Chevalier J. and Gremillard L., The Tetragonal-Monoclinic Transformation in Zirconia: Lessons Learned and Future Trends. Vol.192, pp.1901-1920, 2009.

69. Theunissen G. S. M., Bouma J. S., Winnubst J., Burggraaf J., Mechanical properties of ultra-finegrained zirconia ceramics. Journal of materials science, Vol. 27, pp. 4429-4438, 1992.

70. Reed S. J., Lejus A. M., Affect of grinding and polishing on near-surface phase transformations in zirconia. Materials Research Bulletin. Vol.12(10), pp. 949-954, 1977.

71. Wan K. T., Lathabai S., Lawn B. R., Crack velocity function and thresholds in brittle solids, Journal of the European Ceramic Society. Vol. 6, pp. 259-268, 1990.

72. De Aza A. H, Chevalier J., Fantozzi G., Schehl M., Torrecillas M., Crack growth resistance of alumina, zirconia and zirconia toughened alumina ceramics for joint prostheses, Biomaterials. Vol. 23, pp. 937-945, 2002.

73. Claussen N., Fracture toughness of Al_2O_3 with an unstabilized ZrO_2 dispersed phase, Journal of American Ceramic Society. Vol. 59, pp. 49-51, 1976.

74. Tuan W. H., Chen R. Z., Wang T. C., Cheng C. H., Kuo P.S., Mechanical properties of Al_2O_3/ZrO_2 composites, Journal of The European Ceramic Society. Vol. 22, pp. 2827-2833, 2002.

75. Deville S., Chevalier J., Fantozzi G., Bartolomé J. F., Requena J., Moya J. S., Torrecillas R., Dìaz L. A., Low-temperature ageing of zirconia- toughened alumina ceramics and its implication in biomedical implants, Journal of the European Ceramic Society. Vol. 23, pp. 2975-2982, 2003.

76. Richter H., Fractography of Bioceramics, Key Engineering Materials. Vol 223, pp.157-180, 2002.

77. Varner J. R., Quinn G. D., Wightman M., Fractography of glasses and ceramics V, Journal of the American Ceramic Society. Vol.1, pp. 163-187, 2007.

78. Takahashi K., Matsushige K., Sakurada Y., Application of ultrasonic fractography to visco-elastic materials, Japanese Journal of applied physics. Vol. 21(3), pp.123-125, 1982.

79. Long, D. A., The Raman effect: a unified treatment of the theory of Raman scattering by molecules. Wiley, Vol.8, 2002.

80. Smith E., and Dent G., Modern Raman spectroscopy: a practical approach. Hoboken, NJ, Wiley, 2019.

81. Minsky M., Memoirs on Inventing the Confocal Scanning Microscope, Scanning. Vol 10, pp.128-138, 1988.

82. Atkinson A. and Jain S.C., Spatially Resolved Stress Analysis Using Raman Spectroscopy, Journal of Raman Spectroscopy. Vol. 30(10), pp. 885-891, 1999.

83. Keshu W., Wenliang Z., and Pezzotti G., Determination of in-depth probe response function using spectral perturbation methods, Journal of Applied Physics. Vol.98(11), 2005.

84. Kurtz S.M., Kocagoz S., Arnholt C., Huet R., Ueno M., Walter W.L., Advances in zirconia toughened alumina biomaterials for total joint replacement, Journal Mechanical Behavior Biomed Mater. Vol. 31, pp. 107-116, 2013.

85. Chevalier J., Cales B., Drouin J.M., Low-temperature ageing of Y-TZP ceramics, Journal American Ceramic Society. Vol. 82, pp. 2150-2154, 1999.

86. Kuntz M., Billau K., Chang J.D, Live time prediction of Biolux®delta, Ceramics in Orthopaedics: Proceeding of the 12th BIOLUX® symposium. (Germany), pp.281-288, 2007.

87. Goldberg J.R., Gilbert J.L., Jacobs J.J., Bauer T.W., Paprosky W., Leurgans S., A multicentre retrieval study of the taper interfaces of modular hip prostheses. Clinical Orthopaedics and Related Research®. Vol. 401, pp.149-161, 2002.

88. Panagiotidou A., Meswania J., Hua J., Muirhead-Allwood S., Hart A., Blunn G., Enhanced wear and corrosion in modular tapers in total hip replacement is associated with the contact area and surface topography, Journal of Orthopaedic Research. Vol. 31(12), pp. 2032-2039, 2013.

89. Corfield V., Khan I., Scott R., Hydrothermal stability of ceramic femoral heads, Bioceramics and Alternative Bearings in Joint Arthroplasty, Steinkopff. Vol.1, pp. 59-64, 2007.

90. Garino J. P., The reliability of modern alumina bearings in total hip arthroplasty- update to a 2006 report, Seminars in Arthroplasty, WB Saunders. Vol. 24(4), pp. 193-201, 2013.

91. https://www.ceramtec.com/files/mt_biolox_forte_delta_comparison_en.pdf, last accessed online on 6th September 2019.

92. Khumrak S., Yakampor T., Ceramic on ceramic bearings. The Bangkok Medical Journal. Vol.4, pp. 30-38, 2014.

93. Chevalier J., What future for zirconia as a biomaterial? Biomaterials. Vol.27(4), pp. 535-543, 2006.

94. Chevalier J., Grandjean S., Kuntz M., and Pezzotti G., On the kinetics and impact of tetragonal to monoclinic transformation in an alumina/zirconia composite for arthroplasty applications, Biomaterials. Vol. 30(29), pp.5279-5282, 2009.

95. Boffelli M., Doimo A., Marin E., Puppulin L., Zhu W., Sugano N., Clarke I.C., and Pezzotti G., Chemically driven tetragonal-to-monoclinic polymorphic transformation in retrieved ZTA femoral heads from dual mobility hip implants, Journal of the Mechanical Behavior of Biomedical Materials. Vol. 56, pp.195-204, 2016.

96. Katagiri G., Ishida H., Ishitani A., Masaki T., Direct determination by a Raman microprobe of the transformation zone size in Y2O3 containing tetragonal ZrO2 polycrystals, Adv. Ceram. Vol. 24, pp. 537–544, 1986.

97. Affatato S., Modena E., Toni A., Taddei P., Retrieval analysis of three generations of Biolox femoral heads: Spectroscopic and SEM characterization, Journal of the Mechanical Behavior of Biomedical Materials. Vol. 13, pp.118-128, 2012.

98. Tateiwa T., Marin E., Rondinella A., Ciniglio M., Zhu W., Affatato S., Pezzotti G., Bock M.R., McEntire B.J., Bal B.S., Yamamoto K., Burst strength of BIOLOX®delta femoral heads and its dependence on low-temperature environmental degradation, Materials. Vol 13(2), 350, pp. 1-15, 2020.

99. Lundberg H., Ha N., Hall D., Urban R., Levine B., Pourzal R., Contact mechanics and plastic deformation at the local surface topography level after assembly of modular head-neck junctions in modern total hip replacement devices, In Modularity and Tapers in Total Joint Replacement Devices. ASTM International, 2015.

100. Dyrkacz R. M. R., Brandt J. M., Morrison J. B., O'Brien S. T., Ojo O. A., Turgeon T. R., Wyss U. P., Finite element analysis of the head-neck taper interface of modular hip prostheses. Tribology International. Vol. 91, pp. 206-213, 2015.

101. Huang S., Binner J.G.P., Vaidhyanathan B., Todd R.I., Quantitative analysis of the residual stress and dislocation density distributions around indentations in alumina and zirconia toughened alumina (ZTA) ceramics, Journal of the European ceramic society. Vol. 34, pp. 753-763, 2014.